2010

Probing The Nanoscale Interaction Forces And Elastic Properties Of Organic And Inorganic Materials Using Force-distance (f-d) Spectroscopy

Abhilash Vincent
University of Central Florida

PROBING THE NANOSCALE INTERACTION FORCES AND ELASTIC PROPERTIES OF ORGANIC AND INORGANIC MATERIALS USING FORCE-DISTANCE (F-D) SPECTROSCOPY

by

ABHILASH VINCENT
Bachelor of Technology (B.Tech) CUSAT, Kochi, India, 2002
Master of Science (M.Sc. Engg.) IISc., Bangalore, India, 2004

A dissertation submitted in partial fulfillment of the requirements
for the degree of Doctor of Philosophy
in the Department of Mechanical, Materials and Aerospace Engineering
in the College of Engineering and Computer Science
at the University of Central Florida
Orlando, Florida, USA

Spring Term
2010

Major Professor: Dr. Sudipta Seal

ABSTRACT

Due to their therapeutic applications such as radical scavenging, MRI contrast imaging, Photoluminescence imaging, drug delivery, etc., nanoparticles (NPs) have a significant importance in bio-nanotechnology. The reason that prevents the utilizing NPs for drug delivery in medical field is mostly due to their biocompatibility issues (incompatibility can lead to toxicity and cell death). Changes in the surface conditions of NPs often lead to NP cytotoxicity. Investigating the role of NP surface properties (surface charges and surface chemistry) on their interactions with biomolecules (Cells, protein and DNA) could enhance the current understanding of NP cytotoxicity. Hence, it is highly beneficial to the nanotechnology community to bring more attention towards the enhancement of surface properties of NPs to make them more biocompatible and less toxic to biological systems. Surface functionalization of NPs using specific ligand biomolecules have shown to enhance the protein adsorption and cellular uptake through more favorable interaction pathways.

Cerium oxide NPs (CNPs also known as nanoceria) are potential antioxidants in cell culture models and understanding the nature of interaction between cerium oxide NPs and biological proteins and cells are important due to their therapeutic application (especially in site specific drug delivery systems). The surface charges and surface chemistry of CNPs play a major role in protein adsorption and cellular uptake. Hence, by tuning the surface charges and by selecting proper functional molecules on the surface, CNPs exhibiting strong adhesion to biological materials can be prepared. By probing the nanoscale interaction forces acting between CNPs and protein molecules using Atomic

Force Microscopy (AFM) based force-distance (F-D) spectroscopy, the mechanism of CNP-protein adsorption and CNP cellular uptake can be understood more quantitatively. The work presented in this dissertation is based on the application of AFM in studying the interaction forces as well as the mechanical properties of nanobiomaterials. The research protocol employed in the earlier part of the dissertation is specifically aimed to understand the operation of F-D spectroscopy technique. The elastic properties of thin films of silicon dioxide NPs were investigated using F-D spectroscopy in the high force regime of few 100 nN to 1 μN. Here, sol-gel derived porous nanosilica thin films of varying surface morphology, particle size and porosity were prepared through acid and base catalyzed process. AFM nanoindentation experiments were conducted on these films using the F-D spectroscopy mode and the nanoscale elastic properties of these films were evaluated. The major contribution of this dissertation is a study exploring the interaction forces acting between CNPs and transferrin proteins in picoNewton scale regime using the force-distance spectroscopy technique. This study projects the importance of obtaining appropriate surface charges and surface chemistry so that the NP can exhibit enhanced protein adsorption and NP cellular uptake.

This thesis is dedicated to my lovely wife Melvi Mathew and my wonderful son Lucas James Vincent, who was born on the same day of my thesis defense (17th December, 2009). Melvi, you have been with me through every step of my life in good and bad times. Thank you so much for the unconditional love and support that you have always given me. Lucas, when your mom was pregnant with you, you were my inspiration for finishing this thesis on time. Thank you so much for your lovely decision to get birth just few hours after successful completion of my thesis defense.

ACKNOWLEDGMENTS

I would like to take this opportunity to express my sincere gratitude to all my teachers who bestowed the knowledge upon me at various levels of my academic life. I am grateful to my major advisor Dr. Sudipta Seal, for guiding me through this doctoral dissertation work. From the very first day I joined his group, Dr. Seal has provided me the opportunities to improve my core competency, aptitude, oral and written communication skills. I am extremely thankful to all my candidacy committee members, Dr. Jiyu Fang, Dr. Helge Heinrich, Dr. William Self, and Dr. Alfons Schulte for their advice and guidance throughout the course of my dissertation research. I am fortunate to have the opportunity to work with postdoctoral scholar Dr. Suresh Babu. I believe the significant amount of time Dr. Babu and I had spent on scientific discussions is the key behind the progress I have made during my doctoral research. I would like to thank all my collaborators, Dr. William Self (UCF), Dr. Talgat Inerbaev (UCF), Dr. Artëm Masunov (UCF) Eric Heckert (UCF), Janet Dowding (UCF), Dr. Sanjay Singh (UCF), Suzanne Hirst (Virginia Polytechnic Institute), Dr. Christopher Reilly (Virginia College of Osteopathic Medicine), Dr. Suresh Babu (UCF), Erik Brinley (UCF), Ajay Karakoti (UCF), and Sameer Deshpande (UCF) for their help and support in achieving great success in different collaborative research projects. I am thankful to my seniors Dr. Debasis Bera, Dr. Swanand Patil, Dr. Vishwanathan Venkatachalapathy and Dr. Sameer Deshpande, from whom I received the preliminary hands on training on various instruments and learnt the basics of doctoral research.

The funding supports from National Science Foundation (NSF) and National Institute of Health (NIH) for various nanotechnology research in Dr. Seal's lab is greatly acknowledged. I would like to thank various research organizations such as Materials Research Society (MRS), The Minerals, Metals and Materials Society (TMS), American Ceramic Society (ACS), Electrochemical Society, American Vacuum Society (AVS), and AFM BioMed Society for the opportunities they provided me to present my research in their annual technical meetings. I greatly appreciate the financial support I received from the UCF-SGA, and graduate studies for participating in these events.

I would like to thank Waheeda Illasarie, Karen Glidewell, Cindy Harle, Kari Stiles, Judith Ramos and Angelina Feliciano at AMPAC and MMAE, UCF for their administrative support during the course of my Ph.D.

I would like to thank all my friends. Special thanks to my best friend Prakash Palanisamy (University of Virginia) for his constant encouragement and support. I would like to thank my lab members and my best friends, Ajay Karakoti, Virendra Singh, Amit Kumar and David Reid for the moral and physical support they gave me during the course of my Ph.D.

I would like to take this opportunity to thank my M.S thesis mentor Dr. S. Mohan (Indian Institute of Science, Bangalore), my IISc group members and best friends, Dr. S. Balaji (Université de Moncton), Dr. R. Balu (Université de Moncton), Dr. S. Guruvenket (North Dakota State University), and M. A. Sumesh (Indan Space Research Organization, Bangalore) for the support and encouragement I received during the course of my M.S thesis. I also would like to acknowledge the encouragement given by my undergraduate

thesis advisor Dr. D. P. Mahapatra (Institute of Physics, Bhubaneswar, India) for guiding me through my research project work and for motivating me to choose research as my main carrier. I would like to express my sincere gratitude to my undergraduate teacher, Dr. Jacob Philip (Cochin University of Science and Technology, Kochi) and others professors who taught me the very first lessons of engineering and materials science.

I am not sure how to thank or how to express my sincere gratitude to my lovely wife, Mrs. Melvi Mathew for her constant support and encouragement to pursue research as my main carrier. I would like to acknowledge my father Mr. Alackappillil Mathew Vincent, my mother Mrs. Lilly Vincent, my father in law Mrs. Mathew Geevarghese, my mother in law Mrs. Anna Mathew, my brothers, my sisters, my brother in laws, my sister in laws and all the other family members at this time. All my family members have made many sacrifices to see me achieve this life changing milestone. I strongly believe what I have achieved today is because of their prayers and blessings. I believe the efforts I took to fulfill my greatest dream of becoming a Ph.D scientist were very minute and it became possible only because of the incredible and priceless contributions of all the great individuals I mentioned earlier and many others. Finally yet importantly, I would like to thank God almighty for all the blessing he granted me throughout my life.

TABLE OF CONTENTS

LIST OF FIGURES

LIST OF TABLES

LIST OF SCHEMES

LIST OF ABBREVIATIONS

A549	Human lung adenocarcinoma epithelial cells
AC	Acid catalyzed
AFM	Atomic force microscopy
Asp	Aspartate
ATR FT-IR	Attenuated total reflectance Fourier transform infrared
BC	Base catalyzed
BE	Binding energy
BET	Brunauer-Emmett- Teller
BJH	Barrett-Joyner-Halenda
CMP	Chemical mechanical planarization
CNP/CNPs	Cerium oxide nanoparticle(s)
DFT	Density functional theory
DLVO	Derjaguin-Landau-Verwey-Overbeek
DMEM	Dulbecco's modification of eagle's medium
ELF	Electron localization function
EMEM	Eagle's minimum essential medium
FBS	Fetal bovine serum
F-D	Force-distance
Glu	Glutamate
HRTEM	High-resolution transmission electron microscopy
ICP-MS	Inductively coupled plasma mass spectrometry
LDA	Local density approximation
MPS	Mononuclear phagocyte system
Nanoceria	Cerium oxide nanoparticles
NP/NPs	Nanoparticle(s)

PAW	Projected augmented wave
PBS	Phosphate buffer solution
pl	Isoelectric point
PSD	Pore size distributions
PZC	Point of zero charge
RMS	Root-mean-square
ROS	Reactive oxygen species
SAED	Selected area electron diffraction
SFA	Surface force apparatus
SFM	Scanning force microscope
SMFS	Single molecule force spectroscopy
SPM	Scanning probe microscopy
Tf	Transferrin
Tf:CNPs	Transferrin conjugated cerium oxide nanoparticles
Tf:Qdots	Transferrin conjugated quantum dots
TfRs	Transferrin receptors
UV	Ultraviolet
VASP	Vienna *ab initio* simulation package
WI-38	Human embryo lung fibroblast cells
WLC	Worm-like chain
XPS	X-ray photoelectron spectroscopy
XRD	X-ray diffraction
Yb-CNPs	Ytterbium doped cerium oxide nanoparticles
Y-CNPs	Yttrium doped cerium oxide nanoparticles
ZP/ZPs	Zeta potential(s)

CHAPTER 1: INTRODUCTION

1.1 Introduction to Nanotechnology

Nanotechnology deals with the science of the extremely tiny materials. Nanotechnology was first introduced in the famous lecture of Nobel laureate Richard P. Feynman, "There's Plenty of Room at the Bottom", given in 1959 at California Institute of Technology.[1] Since then, many revolutionary developments and ground breaking inventions have occurred in the area of nanotechnology leading to various applications. According to the US Government's National Nanotechnology Initiative (NNI), "Nanotechnology is the understanding and control of matter at dimensions of roughly 1 to 100 nanometers, where unique phenomena enable novel applications."[2]

Literally, nanotechnology means the technology performed at nanoscale that has major implications in real world. It deals with the creation and manipulation of physical, chemical and biological systems at scales ranging from a few nanometers to submicron dimensions. Nanostructured materials can be made in various shapes and sizes, including spheres, rods, wires, tubes, and triangles. Nanomaterials exhibit very high surface area due to their tiny size. Increase in the surface area by few orders of magnitude can results in having large number of atoms to be present on the surface of the material. This leads to interesting variations in the mechanical, physical, chemical, biological and optical properties of the material compared to its bulk counterpart.

Although nanotechnology is currently well known, it applications remain unexplored. The current trend in nanotechnology research promises future breakthroughs in nanoelectronics, nanomedicine, energy, biotechnology and information technology. The

discovery of novel materials, processes, and phenomena at the nanoscale, as well as the advancement of experimental and theoretical techniques may provide new opportunities for the scientist and engineers to explore novel applications involving nanostructured materials.

1.2 Cerium Oxide Nanoparticles

Cerium is a rare earth element of the lanthanide series. While most of the rare earths exist in trivalent state, cerium exhibits both $^{+}4$ and $^{+}3$ oxidation state and can flip-flop between these two oxidation states in a redox reaction.[3-5] It is established that CNPs can act as excellent oxygen buffers, due to their redox capacity.[6] As a result of alterations in the oxidation states of Ce in CNPs, they exhibit oxygen vacancies (defects), in their lattice structure.[3, 4] The valence of Ce and the resultant defect structure of cerium oxide are dynamic and may change spontaneously or in response to physical parameters like temperature, presence of other ions, and oxygen partial pressure.[4, 5, 7]

Due to their unique switching oxidation capabilities, CNPs are found to exhibit antioxidant properties by scavenging radicals in biological systems. Treatment of rat neuron cells with CNPs showed increased lifespan and reduced cell injury with hydrogen peroxide and UV light in vitro.[8] Other potential biological application of CNPs includes radiation protection of healthy cells in radiation therapy[9], prevention of retinal degeneration from intracellular peroxides[10] and neuroprotection of spinal cord neurons.[11]

1.3 Silicon Dioxide Nanoparticles

Silica NPs are widely used in various applications due to their excellent electronic, mechanical, optical and biological properties. Currently, silica NPs are extensively

studied for their potential use as photonic crystals, optical filters, chemical sensors, biosensors, nano-fillers for advanced composite materials, biomarkers for imaging, substrates for quantum dots, and catalysts. Properties such as optical absorption/transmission, specific surface area, porosity, density and mechanical strength are some of the key parameters that determine the utilization of silica NPs in various applications.

1.4 Presented Study

Considering the beneficial effects of the oxide NPs in many industrial applications, a study exploring various properties such as structural, mechanical, porosity, surface roughness, optical, surface potential, aging and biological interactions (protein adsorption and cellular uptake) are conducted in detail in this dissertation. Though various properties of oxide NPs (CNPs and silica NPs) are explored here, the major focus of this dissertation is devoted towards understanding the nanoscale mechanical and biophysical properties of oxide NPs. The force at which most of the nanoscale properties becomes relevant falls between picoNewton to microNewton scale. Hence, AFM based F-D spectroscopy technique is utilized to explore the nanomechanical and biophysical properties of oxide NPs. The first half of this dissertation discuss in detail about AFM F-D spectroscopy and their applications in probing nanoscale mechanical forces. For a deep and thorough, understand of this technique, a nanoscale indentation experiment was performed on thin films of silica NPs of few 100 nm thickness and their nanoscale elastic properties were determined. The changes in the nanomechanical properties of silica nanoparticles related to their particle size and thin film surface morphology are discussed. The second part of

the dissertation focuses on the application of AFM F-D spectroscopy in probing the interaction forces acting between protein molecules and cerium oxide NPs utilizing functionalized AFM tips. This dissertation also includes the detailed synthesis procedures of size-selected oxide NPs, their surface properties, and their aging behavior in dispersion. Showing that the surface charge modification of CNPs can affects protein adsorption and cellular uptake can be considered as one of the major outcomes of this dissertation. The NP-protein interaction study could lead to a better understanding of the interaction forces acting between NPs and biological cells during cellular uptake and in future may lead to the design of expert drug delivery systems.

1.5 Organization of the Dissertation

The main focus of the dissertation is based on the atomic force microscopy (AFM) based force-distance spectroscopic investigation of various nanomechanical properties such as NP-protein interaction forces, stretching elastic behavior of protein molecules and nanostructured thin film elastic modulus for various applications.

Different chapters in this dissertation are reproduction (partial or complete) of various publications resulting from the author's research work during the course of his doctoral studies at Surface Engineering and Nanotechnology Facility in the Advanced Materials Processing and Analysis Center at University of Central Florida, Orlando, FL, USA. In some cases, the publications are edited to suit the format of the dissertation.

First chapter (the current chapter) gives an introduction to oxide nanoparticles and their importance in various applications followed by the details on how various chapters are organized in this dissertation.

In the second chapter, the author is discussing the application of F-D spectroscopy in the high force regime (<1 μm) in investigating the mechanical properties of nanostructured thin films. Silicon dioxide nanoparticle (nanosilica) thin films are prepared using acid and base catalyzed sol-gel technique and their mechanical properties are investigated as a function of nanoparticle size and porosity. The films displayed a range of elastic modulus depending on the nature and concentration of the catalyst used for their synthesis. Along with their mechanical property measurements, the optical characteristics of these films were also tested and the results are presented in the supporting information of this chapter.

In the third chapter, the author is investigating the influence of environmental aging parameter on the surface charges of cerium oxide nanoparticle. Here, surface charge modified hydrated CNPs are synthesized and their dynamic ion exchange interactions with the surrounding medium are investigated in detail. Time dependent Zeta (ζ) potential (ZP) variations of CNPs are demonstrated as a useful characteristic for optimizing their surface properties. The surface charge reversal of CNPs observed with respect to time, concentration, temperature and doping is correlated to the surface modification of CNPs in aqueous solution and the ion exchange reaction between the surface protons (H^+) and the neighboring hydroxyls ions (OH^-). Using density functional theory (DFT) simulations, it is demonstrated that the adsorption of H^+ ions on the CNP surface is kinetically more favorable while the adsorption of OH^- ions on CNPs is thermodynamically more favorable. The importance of selecting CNPs with appropriate surface charges and the implications of dynamic surface charge variations are

exemplified with applications in microelectronics and biomedical. Here, F-D spectroscopy technique is employed to understand the interaction between freshly prepared and aged CNPs with silica surface for chemical mechanical planarization application. Similarly, the interactions between freshly prepared and aged CNPs with transferrin protein are compared for biomedical applications.

The fourth chapter is focusing on single molecule force spectroscopic (SMFS, F-D spectroscopy using single molecule probes) investigation of transferrin protein (Tf) interaction with cerium oxide nanoparticle (CNP) for targeted cellular uptake. Here, transferrin conjugated AFM probes are used for conducting F-D spectroscopic measurements in the low force regime (<1 nN) on CNPs thin films. By tuning the surface charges of the CNPs from positive to negative zeta potential, it was found that the Tf-CNP bonding adhesion can be tuned to a greater extend. Similarly, binding energy values obtained from DFT calculations predicted an increase in bond strength between the transferrin and CNPs upon surface protonation and charge modification. Transferrin-conjugated CNPs were tested for their binding stability and preferential cellular uptake efficiency by incubating them with human lung cancer cells (A549) and normal embryo lung cells (WI-38). Detailed experimental results supported by theoretical calculations on Tf-CNP bonding and the mechanism of preferential cellular uptake of these particles are presented in this chapter.

Before going into the individual chapter, a general overview on the importance of using force-distance spectroscopy techniques in understanding the interaction force and mechanical properties of different material system are provided in the following section.

1.6 Force Sensing-Current Understanding-An In Depth Literature Review

Using atomic force microscopy (AFM) based force-distance spectroscopy it has become possible to measure the forces acting between different interfaces at high precision. The manipulation of individual molecules by scanning force microscope tips allows us to study the mechanical properties of individual biomolecules and cellular components.

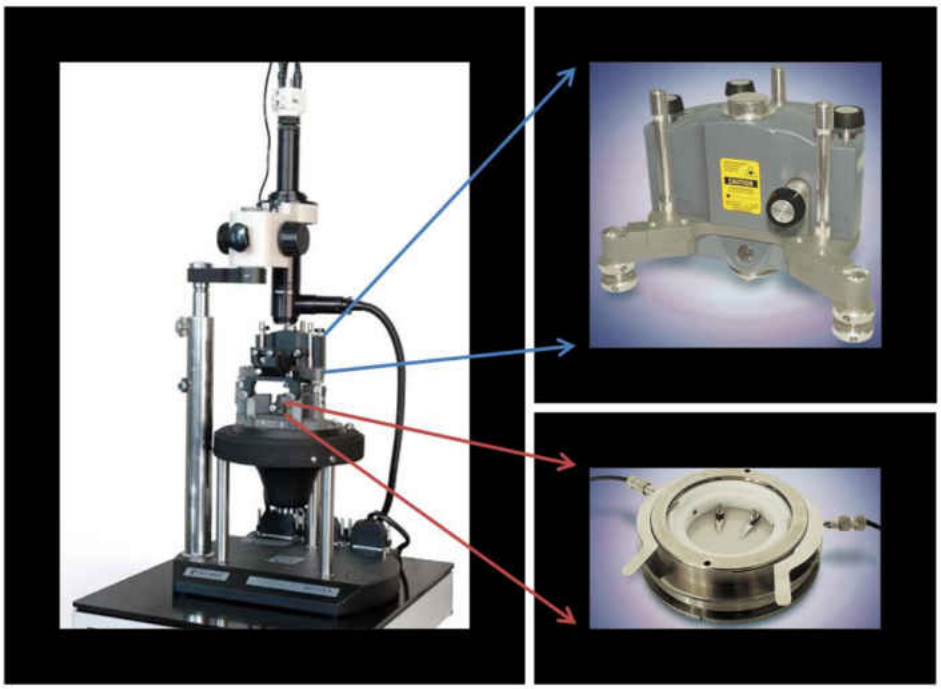

Figure 1.1: Force spectroscopy measurements were conducted using NT-MDT Solver Pro Atomic Force Microscope (left) with a SMENA controller (top right). For measurements in liquid, a closed (hermetic) liquid cell having flow through capability (bottom right) was used.

1.6.1 Atomic Force Microscope as a Tool for Sensing Molecular Forces

Since its invention (1986) by Binning, Quate and Gerber[12] atomic force microscope has evolved from being a predominantly imaging technique to a method that allows the investigation of molecular forces at interfaces in micro to macroscales.[13, 14] The cantilever of the microscope acts as a sensor probing the local interaction between the tip and the sample

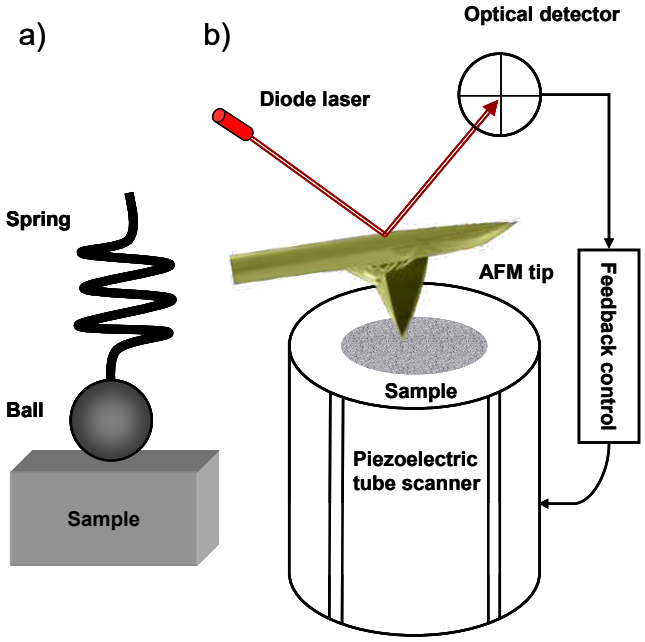

Figure 1.2: (a) The 'small ball on weak spring' model of an AFM cantilever. This model represents the cantilever as an interaction force sensor (b) Schematic diagram of an AFM. Here, the sample is placed on a piezoelectric tube actuator stage that can move in the x, y and z directions. The interactions between the probe tip and the sample are measured by monitoring the deflection of the laser from the cantilever surface. The cantilever deflection in response to tip-sample interactions is detected by a four-quadrant optical photodiode detector. A feedback controller controls the position of the cantilever with respect to the sample by adjusting the piezoelectric tube actuator and collects the data.

The 'small ball on a week spring' model (Figure 1.2) is a useful way of representing the AFM cantilever. In this model, a week mechanical spring (AFM cantilever) is used to

measure the forces between a ball (AFM probe) and a sample whose position can vary relative to the probe. The probe and sample are translated relative to each other using a piezoelectric device, and the movement of the spring is measured by tracing the laser beam reflected off the cantilever surface on a position sensitive detector.

1.6.2 Force-Distance (F-D) Spectroscopy-Introduction

The interaction forces can be determined using the force-distance curve obtained by detecting the cantilever deflection when the tip of the force microscope is moved towards and away from the surface (Figure 1.3).

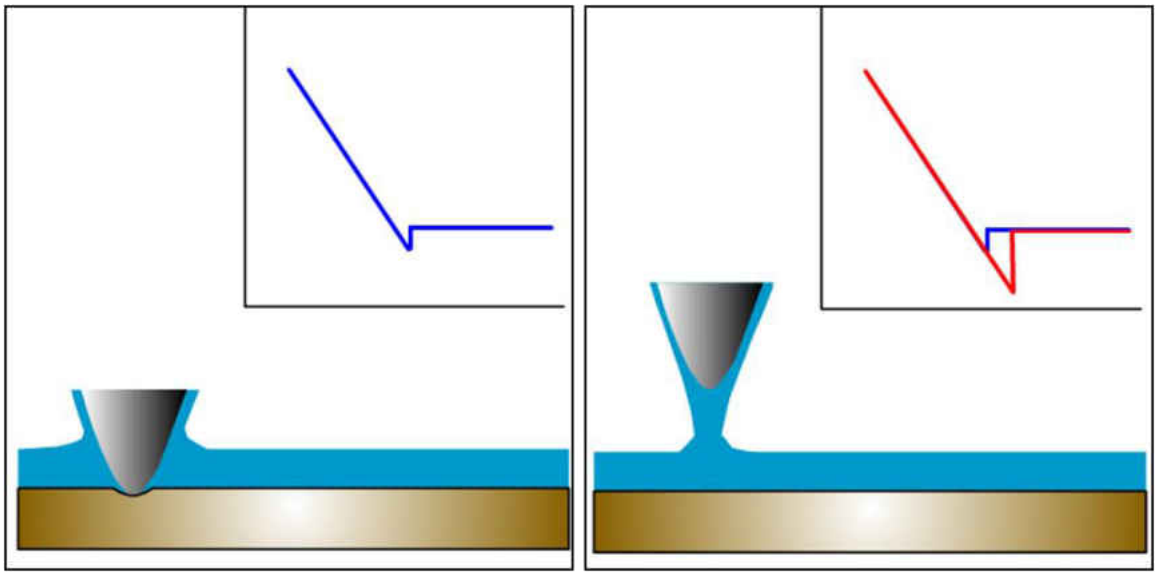

Figure 1.3: Schematic of force-distance spectroscopy technique. The blue curve in the left image represents the cantilever deflection-distance curve obtained while the AFM tip approaches the sample. The red curve corresponding to the image shown in the right image represents the cantilever deflection-distance curve

The applied force F can be deduced from the cantilever deflection z_F using Hook's law,

$$F = kz_F \tag{1.1}$$

A force resolution in the range of picoNewton to microNewton can be achieved in these experiments. In the low force regime, The interactions observed can range from Van der Walls forces in the nanoNewton scale to entropic forces of several hundreds picoNewton. In most of the cases, the interactions occurring are strongly depend on the experimental conditions, such as the tip and sample material, chemical modification of the surfaces, and the surrounding medium. When measurements are performed in air, Van der Waals forces, which are always present at the interface, are in general superimposed by the presence of stronger capillary forces, which are caused by the condensation of water vapor in the area where the tip contacts the sample. The effect of these capillary forces can be avoided if the measurements are performed in fluids.

Force-distance spectroscopy experiments in aqueous solutions are of major importance to scientists who are working in the area of biophysics since only this environment allows the study of native biological processes and elastic behavior of single molecules, such as nucleic acids, proteins and biological cells in situ. Electrostatic forces, that are predominant in aqueous solutions[15-18] can be mainly attractive or repulsive (Figure 1.4) depending on the surface potential of the sample and ionic strength, and pH of the medium. In addition to electrostatic interactions, the use of molecules with appropriate functional groups can lead to short-range dipole-dipole interactions, hydrogen bonding[19-22] or in the case of ligand-receptor pairs, highly specific and complex binding types as well as covalent bonding character is observed.[13, 14, 23-26]

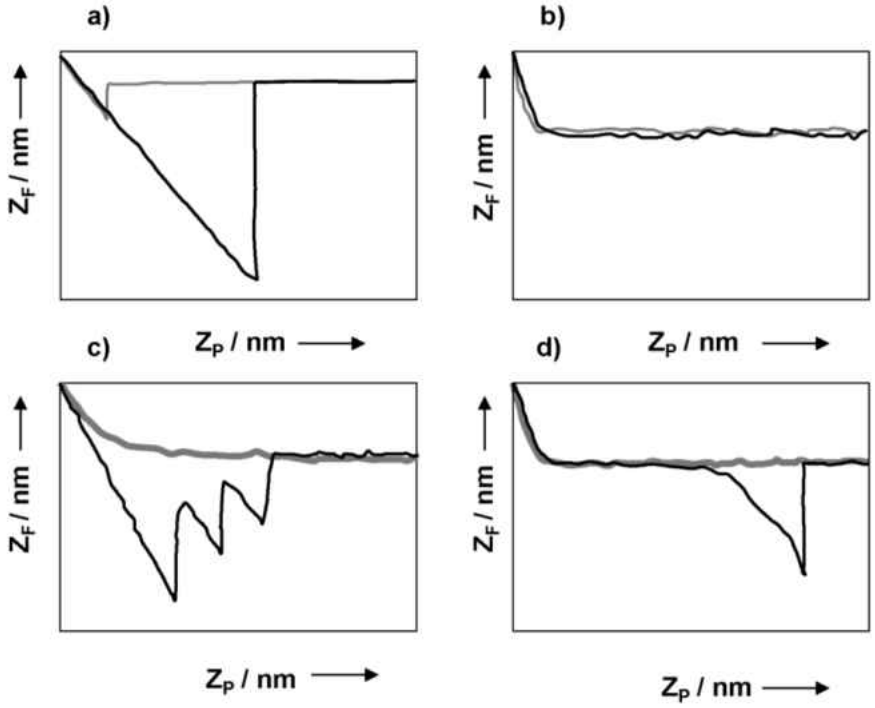

Figure 1.4: Deflection of different interactions by recording force-distance curves. a) and b) are attractive and repulsive electrostatic interaction forces acting between the tip and the sample in fluids c) Specific ligand-receptor interactions between a protein functionalized tip and another protein surface d) Unfolding of a long-chain single protein molecule. The light gray curve shows the approaching of the tip to the surface and the dark black curve shows the retracting of the tip from the surface.

1.6.3 Force-Distance Spectroscopy-Current Understanding

Careful analysis of force-distance spectroscopy during approach and retract can provide a quantitative measurement on the different kinds of interaction forces acting between the tip and the sample at different environments.[27]

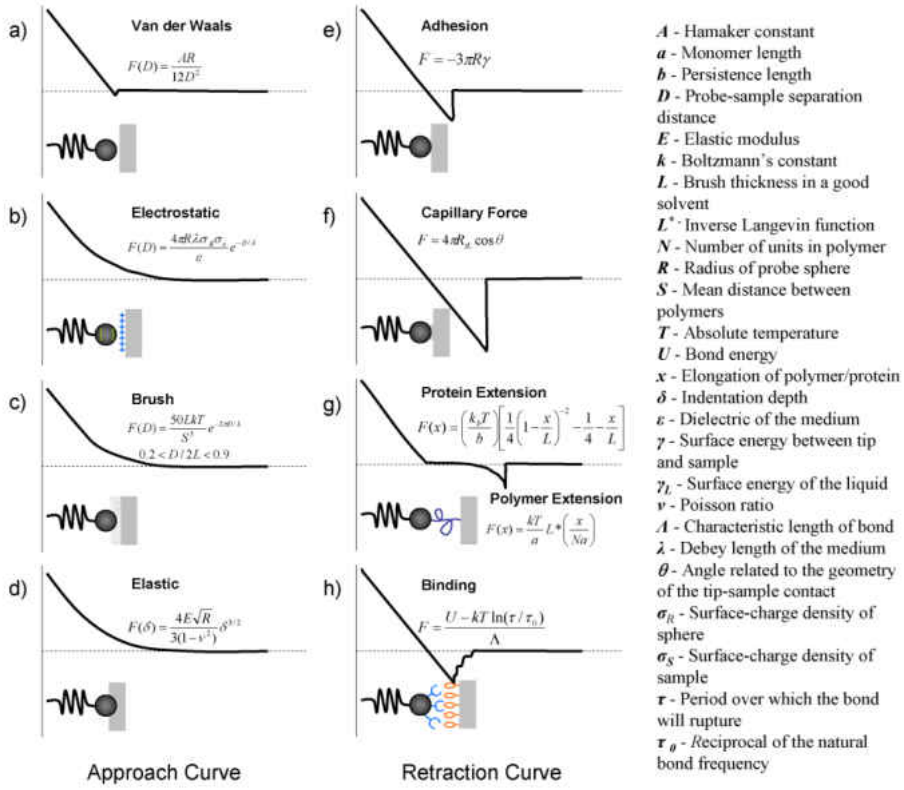

Figure 1.5: AFM force curves. (a-d) Represents approach curves. (e-h) Represents retraction curves. (a) Attractive, van der Waals force in the absence of other forces. (b) Repulsive electrostatic double-layer force in solution. (c) Polymer brushing forces from the polymers grafted onto a solid surface in solution. (d) Nanoindentation curve on an elastic sample. (e) Adhesion between the tip and the sample. (f) Capillary force results from the formation of a water bridge between the tip and sample. (g) Polymer/protein-extension force curves show a characteristic negative deflection and a jump back to zero deflection as the polymer/protein breaks or detaches from one of the surfaces. (h) The unbinding of specific receptor-ligand pairs producing a stepwise return to zero deflection from the point of adhesion.

1.6.3.1 Approach Curve

When two hard surfaces are approached in the absence of any long-range interactions, they will often experience Van der Waals forces. For a large sphere approaching a flat surface, the attractive Van der Waals force varies with the tip sample separation distance

as $1/D^2$. Here, D represents the probe-sample separation distance. If the tip dimensions are close to the size of single atoms, the $1/D^2$ dependence will become a $1/D^4$ dependence.[15] This force appears in the approaching force curve as a small downward deflection just prior to tip sample contact (Figure 1.5a). The downward deflection is often very steep and is most of the times associated with a jump-to-contact event. The jump-to-contact results when the force gradient between the tip and the sample exceeds the stiffness of the cantilever.[16] The magnitude of force depends on the tip, sample and the medium.

Electrostatic and polymer brush forces are two different long-range forces that give rise to similar force curve morphology. Quantitative electrostatic measurements can be obtained with AFM as a biased AFM probe is brought near to a charged sample surface (Figure 1.5b). Research works reported earlier using Surface Force Apparatus (SFA) have shown that the Gouy-Chapman theory (the electrostatic part of DLVO theory) can be used to understand the relation between the measured force and the surface potential.[15, 28, 29] Ducker and colleagues have shown that this theory also holds good for AFM measurements.[30] Subsequently, AFM had been used by many groups to measure the surface charge density and Debye length as a function of pH, electrolyte type and concentration.[16, 31-33]

Polymer grafted surfaces can experience repulsive forces (polymer brush forces) as particles move through their space.[34] This repulsive force is arising from the reduction in the polymer's entropy and can be examined by an AFM.[35, 36] For a densely grafted

polymer sample in a solvent, the brush forces acting on a spherical probe can be described by the Alexander deGennes' theory (Figure 1.5c).

Elastic properties of samples can be investigated with AFM force-distance curves by measuring the depth of indentation corresponding to different applied forces. Second chapter of this dissertation is dedicated to the elastic property measurements of acid and base catalyzed nanosilica coatings[37] obtained by conducting force-distance spectroscopic measurements. AFM force curves have been widely used to examine the viscoelastic properties of a wide range of biological structures, including cartilage[38], lysozyme molecules[39], gelatin gels[40], glial cells[41], epithelial cells[42, 43] and mast cells.[44] Temporal changes in cellular mechanics have also been monitored using AFM.[45, 46] One of the most widely used models for analyzing the mechanical properties of materials based on AFM-force-curves is the Hertz model. This model predicts the forces acting on a spherical probe as a function of the mechanical properties of the materials (both sample and the probe), the radius of the probe and the indentation depth of the probe inside the material[47] (Figure 1.5d).

1.6.3.2 Retract Curve

Most of the time, the retracting force curve will not exactly follows the approach force curve. There is often hysteresis present in the force curves. The most common type of hysteresis is due to the adhesion of the tip to the substrate, which appears as a huge deflection in the force curve. The source of the adhesion can vary depending on the nature of the sample. For a sphere (AFM probe) interacting with a flat surface (sample),

the adhesion force is related to the radius of the sphere and the surface energies (Figure 1.5e) of both the sphere and the flat surface.[15] Under normal circumstances, a capillary bridge (resulting from atmosphere moisture) is formed between the tip and the sample. This capillary bridge itself can act as the main source of adhesion between the tip and the sample (Figure 1.5f). Often large force is required to pull the tip away from the capillary bridge as the magnitude of surface tension exerted by the capillary bridge can be huge.[48] In fluids, the adhesive force depends on the energies at the interface between the tip and the sample surfaces, and the medium.[15] Hence, changing the medium itself can change the force of adhesion.[49] A different type of 'adhesion' occurs when a polymer or a protein is pulled between the AFM tip and the substrate. In this case, one can observe a very distinctive 'adhesive' force as the tip is pulled away from the substrate. These curves exhibit a large negative deflection as the polymer or the protein is stretched until they break or detach from the tip or the substrate (Figure 1.5g). If multiple polymer or protein molecules are attached to the tip and/or substrate, a saw-tooth pattern may be observed in the force curve as they detach. A small part of the third chapter and most of the forth chapter of this dissertation are dedicated to the SMFS measurements of interaction forces acting between protein and nanoparticles.[50]

The interaction force measurements between specific biological receptor-ligand systems have generated massive interest to the biophysical community.[51] Here, a ligand-functionalized AFM tip will be brought into contact with the receptor-coated surface (or vice versa); the receptor and ligand molecules will eventually bind, and the tip will be later retracted. The binding force is calculated from the magnitude of the adhesion spikes

(Figure 1.5h). Statistical analysis can be employed here to estimate the bond strengths using multiple force curves.[52, 53] Force-curve studies have been conducted by many groups on several antibody-antigen systems[54-56], avidin-biotin and their analogues[13, 57] and complementary DNA strands.[58]

1.6.4 Problems, Challenges, Solutions

While probing the elastic properties of nonmaterials, one can break the AFM cantilevers or damage the AFM tip. Hence, it is recommended to use high force constant AFM tips for nanoindentation experiments. In addition, it is important to make sure that the depth of indentation is not exceeding ~1/10th the thickness of the film or size of the nanoparticle. For instance, if the nanoparticles are of ~100 nm in diameter, then using an AFM tip of size 10 nm or fewer is more appropriate to extract the mechanical properties. While indenting nanoparticle samples, one might face issues such as material pileup, particle movement, tip blunting, etc. Hence, it is important to conduct multiple force spectroscopy measurements and acquire large number of data points to reduce possible errors involved in these types of measurements.

While probing the interaction forces acting between the nanoparticles and protein molecules, one can face many challenges in acquiring the real physical data. It is very important to select AFM tips with a very low spring constant (10-50 pN/nm) to detect picoNewton level forces. Conjugating AFM probe with protein molecules can be considered as one of the major challenges involved in these types of experiments. Realizing AFM probes terminated with single protein molecules is a challenging task. During the conjugation process, multiple numbers of protein molecules can get attached

to the AFM probes. In addition, it is possible to have multiple protein molecules interacting with the nanoparticle at the same instant. This might lead to forces of magnitude close to few nanoNewton. The best way to find out if the obtained F-D curves are true representation of single molecule interaction is by fitting the curve with worm like chain (WLC) model. Also, it is important to conduct multiple force-spectroscopy measurements to attain a reasonably good distribution of force values. When it comes to sample preparation, it is important to have a monolayer of nanoparticles of narrow size distribution. Preparing a monolayer of nanoparticles on a silicon or mica substrate can be a challenging task by itself. However, by using suitable adhesive agents such as poly-D-lysine or ploy-L-lysine, nanoparticles can be made to adhere very well to these substrates.

1.7 References

1. Feynman, R., *Eng. Sci.* **1960**, 23, 22-36.

2. http://www.nanotechproject.org/topics/nano101/introduction_to_nanotechnology/

3. Suzuki, T.; Kosacki, I.; Anderson, H. U.; Colomban, P., *J. Am. Chem. Soc.* **2001**, 84, 2007-2014.

4. Herman, G. S., *Surf. Sci.* **1999**, 437, 207-214.

5. Conesa, J. C., *Surf. Sci.* **1995**, 339, 337-352.

6. Land, P. L.; *J. Phys. Chem. Solids* **1973**, 34, 1839-1845.

7. Mamontov, E.; Egami, T.; Brezny, R.; Koranne, M.; Tyagi, S., *J. Phys. Chem. B* **2000**, 104, 11110-11116.

8. Rzigalinski, B. A.; Bailey, D.; Chow, L.; Kuiry, S. C.; Patil, S.; Merchant, S.; Seal, S.; Rzigalinski, B., *Faseb. J.* **2003**, 17, A 606.

9. Tarnuzzer, R. W.; Colon, J.; Patil, S.; Seal, S., *Nano Lett.* **2005**, 5, 2573.

10. Chen, J.; Patil, S.; Seal, S.; McGinnis, J. F., *Nat. Nano* **2006**, 1, 142.

11. Das, M.; Patil, S., Bhargava, N., Kang, J.-F.; Riedel, L. M.; Seal, S.; Hickman, J. J., *Biomat.* **2007**, 28, 1918.

12. Binning, G.; Quate, C. F.; Gerber, C., *Phys. Rev. Lett.* **1986**, 56, 930, (1986)

13. Florin, E.-L.; Moy, V. T.; Gaub, H. E., *Science* **1994**, 264, 415.

14. Lee, G. U.; Kidwell, D. A.; Colton, R. J., *Langmuir* **1994**, 10, 354.

15. Israelachvili, J. N., *Intermolecular and Surface Forces*, 2nd ed., Academic Press, London, 1991.

16. Butt, H.-J., *Biophys. J.* **1991**, 60, 777.

17. Ducker, W. A.; Senden, T. J.; Pashley, R. M., *Nature* **1991**, 353, 239.

18. Marti, A.; Hähner, G.; Spencer, N. D., *Langmuir* **1995**, 11, 4632.

19. Hoh, J. H.; Cleveland, J. P.; Prater, C. B.; Revel, J.-P.; Hansma, P. K., *J. Am. Chem. Soc.* **1992**, 114, 4917.

20. Lee, G. U.; Chrisey, L. A.; Colton, R. J., *Science* **1994**, 266, 771.

21. Boland, T.; Ratner, B. D., *Proc. Natl. Acad. Sci. USA* **1995**, 92, 5297.

22. Wenzler, L. A.; Moyes, G. L.; Olson, L. G.; Harris, J. M.; Beebe, T. P. Jr., *Anal. Chem.* **1997**, 69, 2855.

23. Hinterdorfer, P.; Baumgartner, W.; Gruber, H. J.; Schilcher, K.; Schindler, H., *Proc. Natl. Acad. Sci. USA* **1996**, 93, 3477.

24. Wenzler, L. A.; Moyes, G. L.; Raikar, G. N.; Hansen, R. L.; Harris, J. M.; Beebe, T. P. Jr., *Langmuir*, **1997**, 13, 3761.

25. Mitsui, K.; Hara, M.; Ikai, A., *FEBS Lett.* **1996**, 385, 29.

26. Fritz, J.; Anselmetti, D.; Jarchow, J.; Fernandez-Busquets, X., *J. Struct. Biol.* **1997**, 119, 165.

27. Heinz, W. F.; Hoh, J. H., *Trends in Biotechnol.* **1999**, 17, 143.

28. Israelachvili J.; Adams, G. J., *Chem. Soc. Faraday Trans*. **1977**, 74, 975.

29. Pashley, R. M., *J. Colloid. Interface. Sci.* **1981***,* 83, 531.

30. Ducker, W. A.; Senden, T. J.; Pashley, R.M., *Nature* **1991***,* 353, 239.

31. Hillier, A. C.; Kim S.; Bard, A. J., *J. Phys. Chem.* **1996**, 100, 18808.

32. Raiteri, R.; Gratarola, M.; Butt, H.-J., *J. Phys. Chem.* **1996**, 100, 16700.

33. Larson, I.; Drummond, C. J.; Chan, D. Y. C.; Grieser, F., *Langmuir* **1997**, 13, 2109.

34. Napper, D. H., *Polymeric Stabilization of Colloidal Dispersions*, Academic Press, 1983.

35. Kelley, T. W.; Schorr, P. A.; Johnson, K. D.; Tirrell, M.; Frisbie, C. D., *Macromol.* **1998**, 31, 4297.

36. Overney, R. M.; Leta, D. P.; Pictroski, C. F.; Rafailovich, M. H.; Liu, Y.; Quinn, J.; Sokolov, J.; Eisenberg, A.; Overney, G., *Phys. Rev. Lett.* **1996**, 76, 1272.

37. Vincent, A.; Babu S.; Seal, S., *App. Phys. Lett.* **2007**, 91, 161901-1-161901-3.

38. Jurvelin, J. S.; Muller, D. J.; Wong, M.; Studer, D.; Engel, A.; Hunziker, E. B., *J. Struct. Biol.* **1996**, 117, 45.

39. Radmacher, M.; Fritz, M.; Cleveland, J. P.; Walters, D. A.; Hansma, P. K., *Langmuir* **1994**, 10, 3809.

40. Radmacher, M.; Fritz, M.; Hansma, P. K., *Biophys. J.* **1995**, 69, 264.

41. Haydon, P. G.; Lartius, R.; Parpura, V.; Marchese-Ragona, S. P., *J. Microsc*. **1996**, 182, 114.

42. Putman, C. A.; van der Werf, K. O.; de Grooth, B. G.; van Hulst N. F.; Greve, J., *Biophys. J*. **1994**, 67, 1749.

43. Hoh J. H.; Schoenenberger, C.-A., *J. Cell Sci.* **1994**, 107, 1105.

44. Parpura, V.; Fernandez, J. M., *Biophys. J.* **1996**, 71, 2356.

45. Shroff, S.G.; Saner, D. R.; Lal, R., *Am. J. Physiol.* **1995**, 269, C286.

46. Dvorak, J. A.; Nagao, E., *Exp. Cell Res.* **1998**, 242, 69.

47. Johnson, K. L., *Contact Mechanics*, Cambridge University Press, Cambridge, 1985.

48. Weisenhorn, A. L.; Hansma, P. K.; Albrecht, T. R.; Quate, C. F., *Appl. Phys. Lett.* **1989**, 54, 2651.

49. Lyubchenko, Y. L.; Oden, P. I.; Lampner, D.; Lindsay, S. M., *Nucleic Acids Res*. **1993**, 21, 1117.

50. Vincent, A.; Babu, S.; Heckert, E.; Dowding, J.; Self, W. T.; Hirst, S. M.; Reilly, C. M.; Inerbaev, T. M.; Masunov, A.; Rahman, T. S.; and Seal, S., *ACS Nano* **2009**, 3, 1203-1211

51. Allen, S.; Davies, M. C.; Roberts, C. J.; Tendler S. J. B.; Williams, P. M., *Trends Biotechnol.* **1997**, 15, 101.

52. Hoh, J. H.; Cleveland, J. P.; Prater, C. B.; Revel, J. P.; Hansma, P. K., *J. Am. Chem. Soc.* **1992**, 114, 4917.

53. Williams, J. M.; Han, T.; Beebe T. P. Jr., *Langmuir* **1996**, 12, 1291.

54. Hinterdorfer, P.; Baumgartner, W.; Gruber, H. J.; Schilcher, K.; Schindler, H., *Proc. Natl. Acad. Sci. USA* **1996**, 93, 3477.

55. Allen, S.; Chen, X.; Davies, J.; Davies, M. C.; Dawkes, A. C.; Edwards, J. C.; Roberts, C. J.; Sefton, J.; Tendler, S. J. B.; Williams, P. M., *Biochem.* **1997**, 36, 7457.

56. Dammer, U.; Hegner, M.; Anselmetti, D.; Wagner, P.; Dreier, M.; Huber, W.; Guntherodt, H.-J.; *Biophys. J.* **1996**, 70, 2437.

57. Allen, S.; Davies, J.; Davies, M. C.; Dawkes, A. C.; Edwards, J. C.; Parker, M. C.; Roberts, C. J.; Sefton, J.; Tendler, S. J. B.; Williams, P. M., *FEBS Lett*. **1996**, 390, 161.

58. Lee, G. U.; Chrisey, L. A.; Colton, R. J., *Science* **1994**, 266, 771.

CHAPTER 2: SOLID-SOLID INTERACTIONS AND ELASTIC MODULII OF NANOPARTICLE THIN FILMS

2.1 Introduction

Influence of porosity in mechanical properties such as elastic modulus and Poisson's ratio has been a subject of interest of many researchers as the elastic modulus decreases with increase in porosity[1] and decrease in density.[2] We have prepared porous silica antireflective coatings with 99% and above transmittance on boron silicate glass substrate (see Supporting Information for more details).[3] We found that the refractive index of these coatings could be tuned by varying the particle size and porosity. However an increase in particle size and porosity can affect the bonding between the particles and modify the mechanical strength.[4] Hence it is necessary to understand the influence of porosity and particle size on the mechanical properties of these films.

Mechanical response of the surfaces to forces at nanoscale and nanometer penetration depth levels has been possible with scanning force microscope (SFM)[5-14], where the applied load can be controlled from nanoNewton to picoNewton by changing the tip curvature radius and cantilever stiffness.[7] Herein, we report the surface elastic modulus obtained as a function of microstructure and porosity by force-distance spectroscopy on porous silica coatings prepared by acid and base catalyzed sol-gel process.

2.2 Results and Discussions

2.2.1 Synthesis of Silica Nanoparticle Thin Films

The details of silica sol-gel synthesis, the coating preparation, microstructural and optical characterization are discussed in detail in Supporting Information. Using the acid

catalysis, less porous and highly dense coatings can be achieved while use of base catalyst results in highly porous and less dense silica coatings.[3] In our experiments, depending on the nature of the catalyst (acid or base) the samples were coded as A or B. It is to be noted that only one molar ratio of acid catalyzed silica sample was chosen (TEOS to HNO_3 molar ratio of 1:0.025) while two different molar ratios of base catalyzed silica samples (TEOS to NH_4OH molar ratio of 1:1 and 1:3) were used for the experiment, as the variation in molar ratio of acid catalyst did not result in marked variation on surface morphology and mechanical properties among other acid catalyzed samples. The coatings were deposited on boron silicate glass by dip coating.

2.2.2 Force-Distance Spectroscopy on Silica Nanoparticle Thin Films

Figure 2.1 shows the F-D curves acquired on a relatively smooth area (selected based on AFM image) of the individual coating samples as well as on the glass substrate at a load of 2.0 μN using NT-MDT scanning force microscopy. Acquisition of the force curve at several points was conducted for better uniformity and repeatability. All measurements were made with a silicon cantilever having a tip size of 20 nm diameter. These curves are then compared with the curve on the blank glass substrate. Since the silicon tip couldn't penetrate the hard glass substrate (AFM images shows no sign of indentation on glass substrate), the z axis movement of the piezo stage (linear solid curve, G in Figure 2.1) represents only cantilever deflection and no indentation while collecting force curves on blank substrate. Considering the F-d curves of the coatings, there is a clear trend of decrease in slope as well as deviation in the linear nature of the curve due to tip indentation. The difference in the piezo height between the substrate and the silica

coatings provides the depth of indentation. The cantilever deflection D (in nA) can be converted into the applied load F (in nN) using the relation,

$$F = kD / S, \tag{2.1}$$

where k is the spring constant (in nN/nm) determined using the method of Sader *et. al.*[15] and S is the sensitivity (in nA/nm) obtained from the slope of the F-d curve on the glass substrate. Base catalyzed silica coatings showed lower resistance to indentation as indicated by the decrease in slope of the F-d curves and hence exhibits lower mechanical strength (higher depth of indentation) in comparison to the acid catalyzed silica coating.

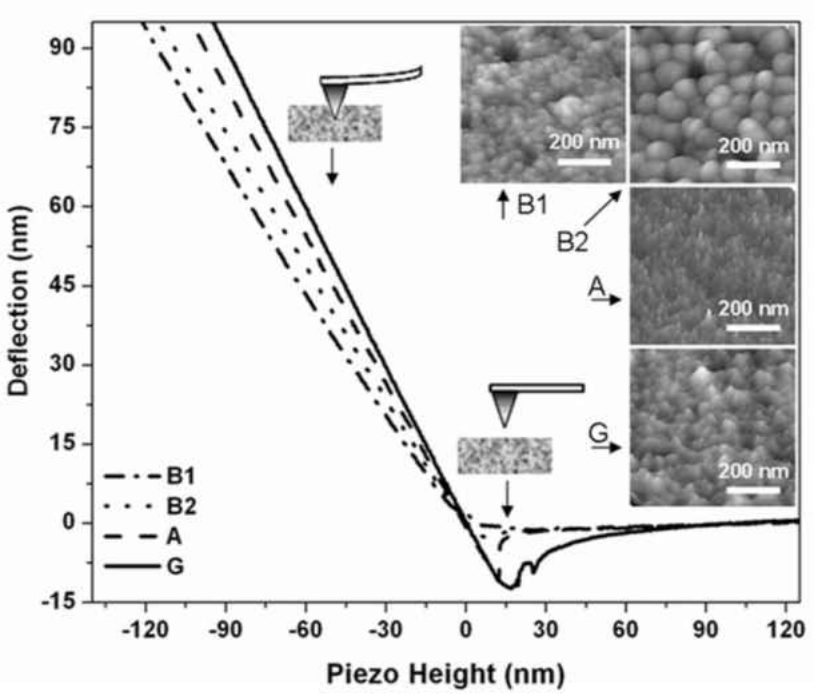

Figure 2.1: Force-distance curves obtained from base catalyzed silica coatings (B1 and B2), acid catalyzed silica coating (A) and a bare glass substrate (G). Inset shows the corresponding AFM images of the samples. Particle size increases with increase in the basic nature of the catalyst. The mean particle size was found to be 5nm, 30nm, 100 nm for A, B1 and B2, respectively.

2.2.3 Elastic Modulus of Silica Nanoparticle Thin Films

It is now possible to calculate the tip indentation Δz into the soft sample as the difference in the respective piezo height, z positions relative to the blank glass reference. The elastic deformation has been defined through Hertz equation[9-14,] for a parabolic indenter (Parabolic indenter is the most reasonable approximation for an SFM tip), as

$$F = (4/3)E_r R^{1/2}\delta^{3/2}, \tag{2.2}$$

where E_r is the reduced elastic modulus (also called as effective elasticity), R is the radius of the indenter and δ is the indentation depth. The elastic modulus of the sample, E_s can be obtained from the sample tip interaction and is given by,

$$1/E_r = \left(1-\nu_t^2\right)/E_t + \left(1-\nu_s^2\right)/E_s, \tag{2.3}$$

where υ is the Poisson's ratio, E_t and E_s is the elastic modulus of the tip and sample respectively. The elastic modulus and the poison ratio of silicon tip were taken from the literature (E_t = 130GPa, ν_t = 0.27).[16] Poisson's ratio of 0.22 was assumed for silica film and it was reported to be not affected by the variation in film density.[17] Hertzian model can be applied only when $E_t > E_s$.[11] The model is valid only for elastic deformation and assumes no significant adhesion between the tip and the sample.[18] It is important to avoid any contribution from inelastic deformation and tip-sample adhesion during the analysis of the load displacement curve. The adhesion between contacting bodies becomes more significant at nanoscale.[19] We have observed adhesion between the tip and silica coatings during unloading. Also in the case of base catalyzed silica films, cracking and pileup of material was observed during indentation due to plastic deformation. Hence, only the

initial elastic deformation region of the loading curve was analyzed for elastic modulus determination.

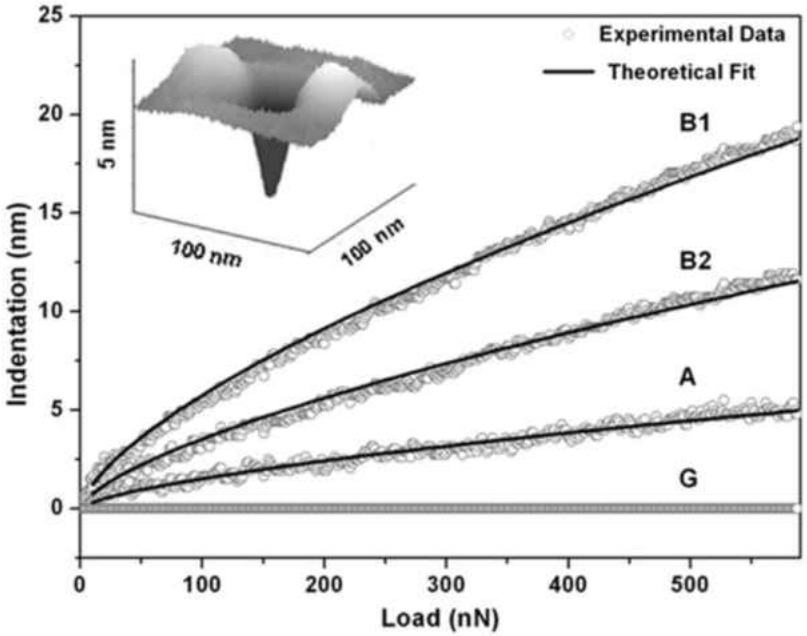

Figure 2.2: Load-Indentation profile obtained from base catalyzed and acid catalyzed silica coatings. The power-law fitting coefficient for each of the curves is listed in Table 2.1; Insert shows the three-dimensional surface profile of an indent obtained on an acid catalyzed coating.

Nanoindentation curves obtained on base and acid catalyzed silica coatings are shown in Figure 2.2. The effective elastic modulus of the coatings can be obtained from the indentation curve through power-law regression analysis using the following equation,

$$\delta = aF^b, \tag{2.4}$$

where δ is the indentation depth, and a, b are the fitting parameters. The value of power, b is fixed as 2/3 by applying the Hertz model and the value of coefficient, a can be obtained by power law regression fitting (values of coefficient, a are listed in Table 2.1). From the parabolic tip model the reduced elastic modulus, E_r can be calculated as

$$E_r = 3/(4a^{3/2}R^{1/2}), \quad (2.5)$$

where R is the tip radius.

Table 2.1: Structural and elastic properties of acid and base catalyzed silica coatings

Thin Film	Film thickness (nm)[a]	Particle diameter (nm)[a]	Roughness (nm)[a]	Pore radius (nm)[a]	Porosity (%)[a]	Density (g/cc)[a]	Power law coefficient *a*	Elastic modulus (GPa)
A	635±2	5.9±1.1	0.3	1.7	5.0	2.18	0.00007	13.40
B2	105±2	99.5±20.7	3.0	14	36.1	1.47	0.00017	5.02
B1	110±2	33.5±8.8	4.5	4.7	49.1	1.17	0.00027	2.38

[a] Reference[3]

The elastic modulus calculated for acid and base catalyzed coatings are listed in Table 2.1. Among all the coatings, acid catalyzed silica coatings showed the highest elastic modulus (13.4 GPa) and is close to the earlier reported values for sol-gel silica coating.[20,21] This higher value of elastic modulus compared to base catalyzed silica is due to the low porous nature (5%) and higher density (2.18 g/cc) of the coatings. Unlike polycrystalline materials whose mechanical properties largely depends on the nature of grain boundaries, mechanical properties of glassy materials such as silica depend more on composition and structure of the bonding network.[22] Elastic modulus value calculated for base catalyzed silica coating B1 is 1.63GPa, and is close to the reported values for porous silica.[22] The lower value of elastic modulus is due to the presence of large number of pores in the film as the B1 silica film is approximately 49% porous in nature and the density is very low (1.17 g/cc). Due to their high porous nature, porous silica coatings often exhibit very low density[23] and their elastic modulus can be even 10^2-10^4 smaller than that of silica glass.[24]

2.2.4 Significance of Surface Roughness on Elastic Modulus

Coatings obtained from porous silica sol-gel contain roughness in the form of asperities. Presence of these asperities will increase the surface area over which the tip and the sample make the effective contact. This leads to a reduced contact pressure for a given load and results in a lower value of elastic modulus.[10] In order to determine the significance of surface roughness on elastic modulus determination, a nondimensional parameter α has to be considered.

$$\alpha = \sigma_s R / a_0^2 = \sigma_s \left(16RE_r^2 / 9F^2\right)^{1/3}, \tag{2.6}$$

where σ_s is the rms roughness obtained experimentally and a_0 is the contact radius for smooth surfaces under the load F. The Hertz theory for smooth surfaces is valid only if the parameter α is less than 0.05.[25] The value of α calculated for acid catalyzed silica coating with a low surface roughness of 0.3 nm is less than 0.05 which is within the error limit. Hence, no roughness correction is required for acid catalyzed silica coating. However the value of α calculated for base catalyzed silica coating with B1 with a surface roughness of 4.5 nm is 0.23 (>0.05) and the value of value of α calculated for base catalyzed silica coating B2 with a local cluster surface roughness of 3 nm is 0.26 (>0.05). A second nondimensional parameter μ, defined by Greenwood and Tripp[26] is given by,

$$\mu = (8/3)\eta_s \sigma_s \left(2R / \kappa_s\right)^{1/2}, \tag{2.7}$$

where μ_s is the asperity density and κ_s is the mean curvature of the summits of asperities. Greenwood and Tripp obtained two values of μ, which bracketed a wide range of

practical rough surfaces. Using these two parameters, α and μ, the correction required for elastic modulus is determined. The ratio of effective contact radius (experimental), a^* to the Hertz radius (theoretical), a_0 are influenced by the surface roughness as shown in Figure 2.3. Since E is proportional to $1/a^3$, the elastic modulus value after roughness correction for base catalyzed silica coating B1 is approximately 2.38 GPa. In the case of base catalyzed silica coating B2, the coating was mainly formed by individual silica agglomerates (clusters) of size closer to 100 nm (AFM image of B2 in Figure 2.1) and contained larger size pores. However, B2 silica coatings were less porous (approximately 36%) than that of B1 silica coatings. Due to the larger size of silica agglomerates compared to SFM tip diameter, the indentation experiments conducted on these agglomerates particles only represents the mechanical properties of the skeletal silica agglomerates and not that of the porous silica coating. The elastic modulus of individual silica agglomerates obtained after roughness correction is approximately 5.02 GPa. The amplitude contrast AFM images of B2 silica coatings (Figure 2.3 inset) showed that these silica clusters are agglomerates of smaller size (diameter approximately 20 nm) particles with a local cluster surface roughness of 3.0 nm. The bonding strength between these individual particles determines the mechanical properties of these bigger agglomerates. The reason for lower value of elastic modulus of these silica agglomerates is mainly due to the weaker bonding between the individual amorphous particles.

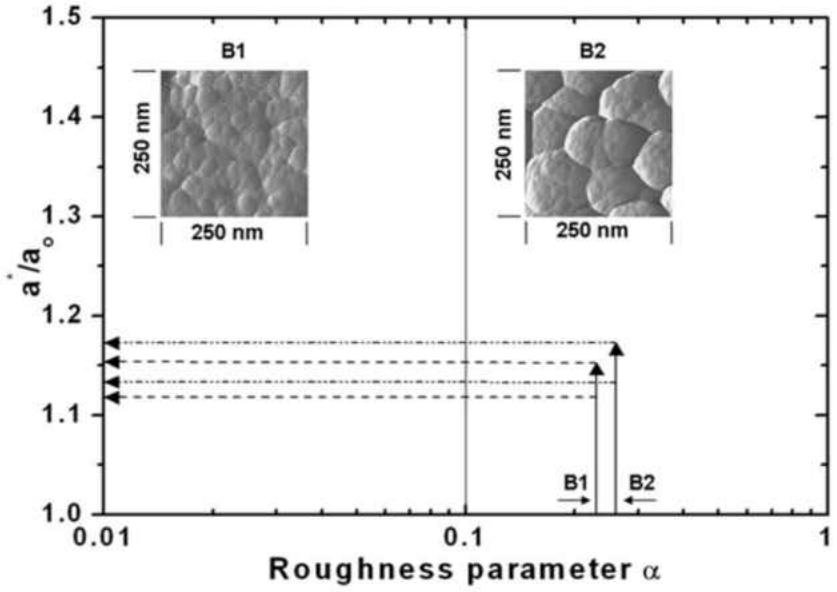

Figure 2.3: Influence of surface roughness on the effective contact radius a^* compared with the Hertz radius a_0 for two values of μ that encompass a wide range of practical rough surfaces.[26] For coating B1, α = 0.23 and 4<μ<17, a^*/a_0 is between 1.12 and 1.15 and for coating B2, α = 0.26 and 4<μ<17, a^*/a_0 is between 1.13 and 1.17; Insert shows the amplitude contrast AFM image of base catalyzed silica coatings.

2.3 Conclusion

Porous silica optical coatings obtained by acid and base catalyzed synthesis showed variation in elastic modulus depending on the microstructure and nature of the coatings. From SFM indentation curves, using the Hertz model we have obtained the elastic modulus of thin film silica optical coatings. Acid catalyzed silica coatings were denser in nature and exhibited higher elastic modulus than base catalyzed silica samples. Between the two base catalyzed silica coatings, the particle size, microstructure and porosity greatly influenced the individual elastic modulus values.

2.4 References

1 Avar, B. B.; Hudyma, N.; Karakouzian, M., *Int. J. Rock Mech. Min. Sci.* **2003**, 40, 919.

2 Fan, H.; Hartshorn, C.; Buchheit, T.; Tallant, D.; Assink, R.; Simpson, R.; Kissel, D. J.; Lacks, D. J.; Torquato, S.; Brinker, C. J., *Nat. Mater.* **2007,** 6, 418.

3 Vincent, A.; Babu, S.; Brinley, E.; Karakoti, A.; Deshpande, S.; Seal, S., *J. Phys. Chem. C* **2007**, 111, 8291.

4 Chen, Y.; Balani, K.; Agarwal, A., *Appl. Phys. Lett.* **2007**, 91, 031903.

5 Pharr G. M.; Oliver, W. C., *MRS Bull.* 1992, 17, 28.

6 Nancy A. B.; Richard, J. C., *J. Vac. Sci. Technol.* A 1989, 7, 2906.

7 Miyake, K.; Satomi, N.; Sasaki, S., *Appl. Phys. Lett.* **2006,** 89, 031925.

8 Salmeron, M. B., *MRS Bull.* **1993**, 18, 20.

9 Heim, A. J.; Matthews, W. G.; Koob, T. J., *Appl. Phys. Lett.* **2006**, 89, 181902.

10 Tan E. P. S.; Lim, C. T., *Appl. Phys. Lett.* **2005**, 87, 123106.

11 Munuera, C.; Matzelle, T. R.; Kruse, N.; Lopez, M. F.; Gutierrez, A.; Jimenez, J. A.; Ocal, C., *Acta Biomat.* **2007**, 3, 113.

12 Salerno M.; Bykov, I., *Microscopy and Analysis* **2006**, 20, S5.

13 Garcia-Manyes, S.; Güell, A. G.; Gorostiza, P.; Sanz, F., *J. Chem. Phys.* **2005**, 123, 114711.

14 Touhami, A.; Nysten, B.; Dufrene, Y. F., *Langmuir* **2003**, 19, 4539.

15 Sader, J. E.; Chon, J. W. M.; Mulvaney, P., *Rev. Sci. Instru.* **1999**, 70, 3967.

16 Brantley, W. A., *J. Appl. Phys.* **1973**, 44**,** 534.

17 Gross, J.; Reichenauer, G.; Fricke, J., *J. Phys. D: Appl. Phys.* **1988**, 21, 1447.

18 Perkins, M.; Ebbens, S. J.; Hayes, S.; Roberts, C. J.; Madden, C. E.; Luk, S. Y.; Patel, N., *Int. J. of Pharm.* **2007**, 332, 168.

19 Gissi, R.; Decuzzi, P., *J. Appl. Phys.* **2005**, 98, 014310.

20 Chan, C. M.; Cao, G. Z.; Fong, H.; Sarikaya, M.; Robinson, T.; Nelson, L., *J. Mater. Res.* **2000**, 15, 148.

21 Yu, S.; Wong, T. K. S.; Hu, X.; Yong, M. S., *J. Sol-Gel Sci. Technol.* **2005**, 35, 69.

22 Takada, S.; Hata, N.; Seino, Y.; Yamada, K.; Oku, Y.; and Kikkawa, T., *Jpn. J. Appl. Phys.* **2004**, 43, 2453.

23 Moner-Girona, M.; Roig, A.; Molins, E.; Martinez, E.; Esteve, J., *Appl. Phys. Lett.* **1999**, 75, 653.

24 Gronauer M.; Fricke, J., *Acustica* **1986**, 59, 177.

25 Johnson, K. L., *Contact Mechanics*, Cambridge University Press, Cambridge, 1992, pp. 397-423.

26 Greenwood J. A.; Tripp, J. H. *J. Appl. Mech.* **1967**, 34, 153.

2.5 Supporting Information: Sol-gel Derived Silica Nanoparticle Thin Films

2.5.1 Introduction

Antireflective (AR) coatings play an important role in variety of optical technologies by reducing the reflective losses at the interfaces. AR coatings have been widely used in many energy related applications such as solar thermal and photovoltaic systems. In the case of devices, such as flat panel display AR coatings are used to reduce the transmission losses.[1] There are several approaches to introduce anti-reflectance and among them, the coating with an adjustable refractive index on the substrate is a prominent one. An ideal homogeneous antireflective coating can achieve effectively 0% reflection at a specific wavelength when its refractive index (n_c) is equal to $(n_1 n_2)^{1/2}$, where n_1 and n_2 are the refractive indices of the air and the substrate, respectively.[2] A typical glass has an index of refraction between 1.45 and 1.65 in visible spectral region, which implies that the index of refraction of the antireflective interference film must be between 1.20 and 1.25.[3] Such a low-index requirement makes it practically impossible to design a dense single-layer AR film on glass. Further, the low refractive index is difficult to attain with any known low index coating material (the lowest index optical material is MgF_2 with n = 1.38 at 600 nm).[4] Since the refractive index of a material is related to its density, the index can be lowered by introducing porosity, provided that the pore sizes are much smaller than the electromagnetic wavelengths of interest. The refractive index is related to the porosity according to the Lorentz-Lorenz relationship[5],

$$\frac{\left(n_f^2 - 1\right)}{\left(n_f^2 + 2\right)} = \left(1 - V_f\right)\frac{\left(n_s^2 - 1\right)}{\left(n_s^2 + 2\right)} \tag{2.8}$$

where n_f and n_s are the refractive indices of the porous film and the solid skeleton, respectively, and V_f is the volume fraction of the pores. Thus, by tuning the porosity, hence refractive index of the coating, it is possible to tune the antireflective properties of any substrate material.

The materials widely used as AR coatings are dielectric materials such as silica, titania and alumina with refractive indices of 1.45, 2.3 and 1.65 respectively in the mid-visible range spectral region. Silica coating has low refractive index, good durability and environmental resistance.[6] As a result of tunable refractive index properties, porous silica is considered to be one of the best anti-reflective coatings[7, 8] which attracted wider interest in optical, microelectronic, and thermal applications.[9-13] To introduce porosity in thin films, broadly three approaches can be followed: (i) by introducing organic filler particles as templates that can be removed later to create the porosity, (ii) by coating made up of larger particles, (iii) by the use of bimodal size distribution.[14] Sol-gel technique is widely used for producing porous coatings. Sol-gel technique gives a greater control on pore size as pore size can be modified by tuning the process parameters.[6, 15, 16] While the use of as filler particles for introducing porosity lead to poor mechanical properties[17, 18] porous silica coatings developed through colloidal sol-gel route were reported to be stress-free and highly damage resistant.[18, 19] Acid or base or a combination of acid and base has been used as catalyst to form the porous silica coatings.[16-18] However, still a comprehensive understanding relating the role of catalyst, catalyst concentration with surface and optical properties are limited.

In the present study, we have used acid and base catalysis for the fabrication of anti-reflective porous silica coatings with a transmission of about 99% on boron silicate glass. The effect of catalyst nature and concentration on porosity, surface roughness, micro-structural and optical transmittance has been reported.

2.5.2 Experimental Section

2.5.2.1 Materials

Silica porous coatings were prepared by sol-gel method using tetraethyl orthosilicate (TEOS, Sigma Aldrich, 98%) as precursor and ethanol as the solvent (Sigma Aldrich, 99.5%). The molar ratio of TEOS to ethanol was maintained at 1:30 for all the experiments and either a base (ammonia) or an acid (nitric acid) was used as a catalyst. Depending on the nature of catalyst (acid or base), the samples were coded as AC or BC. All solutions were aged at different times to ensure completion of condensation reaction depending on the concentration of the catalyst to form a sol optimum for coating. Table 2.2 summarizes the sample codes and the corresponding variation in molar ratio, viscosity and aging time for both acid and base catalyzed samples. Viscosity measurements were carried out using HAAKE Viscotester 7 rotational viscometer, at 25°C and at a shear rate of 244.8 s^{-1}. The coatings were made on glass slides by dip coating technique (Dip Coater, 1000 IUD, KSV Instruments Ltd., Finland) at a withdrawal rate of 8.5 cm/min. Boron silicate glass (BK-7) having a refractive index close to 1.53 at 550nm, was used as substrate. The glass slides used as substrate for

coating were ultrasonicated in acetone for 10 minutes. The coatings were dried at room temperature in air under normal atmospheric conditions for 12 hours.

Table 2.2: Details of synthesis parameters for the preparation of porous silica

Coating	TEOS to catalyst molar ratio	Viscosity (mPa.s)	Aging time (hrs)
BC11	1:1	1.92	72
BC12	1:2	1.87	30
BC13	1:3	1.84	18
AC	1:0.025	2.56	18

2.5.2.2 Surface and Optical Characterization of Silica Nanoparticle Thin Films

The surface topography and the microstructure of the coatings were studied with a Multimode AFM (MMAFM-2, Nanoscope IIIa Digital Instruments) in tapping mode using a 7 nm radius silicon tip (PPP-NCH, Nanosensors). The surface root-mean-square (RMS) roughness values were obtained from the analysis of AFM images. Solver PRO Scanning Probe Microscope (NT-MDT Co.) was used to perform the coating scratch resistance measurements. The coating thickness and refractive index was calculated from the optical transmission spectra by simulation using Film Star software (FTG Software Associates). Ellipsometry measurements (VASE Spectroscopic Ellipsometer) were used to validate the calculated thickness and refractive index from the simulation. Transmittance of silica coatings were measured with a UV-visible spectrophotometer (Varian, CARY 1E) over a spectral range of 200-900 nm. Attenuated Total Reflectance - Fourier Transformed Infra Red (ATR FT-IR) spectroscopy was used for evaluating structural modifications. ATR FT-IR spectra were recorded in a Perkin Elmer (Spectrum one) FT-IR spectrometer in the range of 4000-600 cm^{-1}. Surface area measurements were

carried out to obtain the texture properties (surface area and pore volume) using a NOVA 4200e Surface area & Pore size analyzer. The silica samples were degassed at 378K for 12 hours and the adsorption-desorption isotherms were obtained at 77K. The surface area was calculated using Brunauer-Emmett-Teller (BET) method and the average pore radius (r) and pore size distributions (PSD) were calculated by the Barrett-Joyner-Halenda (BJH) method.

2.5.3 Results and Discussion

2.5.3.1 Surface Morphology of Silica Nanoparticle Thin Films

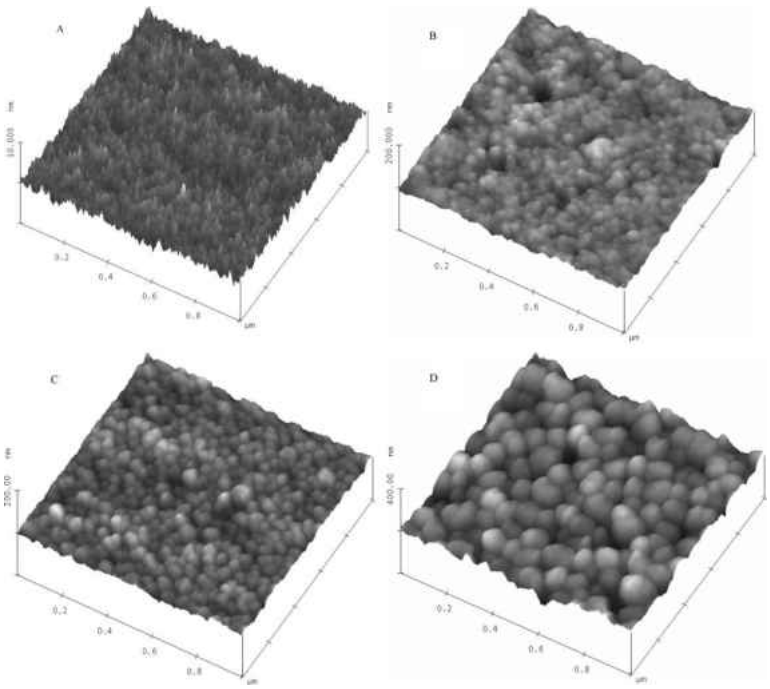

Figure 2.4: AFM images of acid- and base-catalyzed silica coatings on BK-7 glass substrate: (A) AC, (B) BC11, (C) BC12, and (D) BC13. Particle size increases with increase in the basic nature of the catalyst. All the images are taken at 1 μm x1 μm area at a scan rate of 1 Hz.

AFM patterns of the surface morphologies of silica films for AC, BC11, BC12 and BC13 are shown in Figure 2.4. AFM images exhibited a direct relation between the surface morphology with the nature and concentration of catalyst. The acid catalyzed coating (AC) exhibited smooth and dense surface while base catalyzed coatings (BC) showed rough and coarse particle morphology. Among the three bases catalyzed samples, BC11 showed finer particle while BC13 showed coarser particles. With the increase in base concentration, there was a corresponding increase in particle size. It is to be noted that even lower molar ratio of acid catalyst (AC in Table 2.2) resulted in smooth surface morphology and further increase in acid catalyst concentration did not result in marked variation of surface morphology. Apart from the one acid catalyzed silica sample mentioned as coating AC in Table 2.2, two different concentrations, one with lower and one with higher acid content, were prepared with molar ratios of 1:0.0125 and 1:0.0375. Optical transmission and particle size of these coatings remained the same and were found to be independent of the amount acid catalyst used. However, a trend of transition from an ultra smooth to a slightly clustered network structure was observed with increase in acid content. Since changes in acid content has marginal influence on the morphology and transmission only coating AC is reported here. Particle size distribution calculated from the AFM images (Figure 2.4) are shown in Figure 2.5. The mean particle size was found to be 5 nm, 30 nm, 55 nm, 100 nm for AC, BC11, BC12 and BC13, respectively. The surface studies showed a direct relation of particle morphology on the acidic/basic nature of catalyst in the precursor solution.

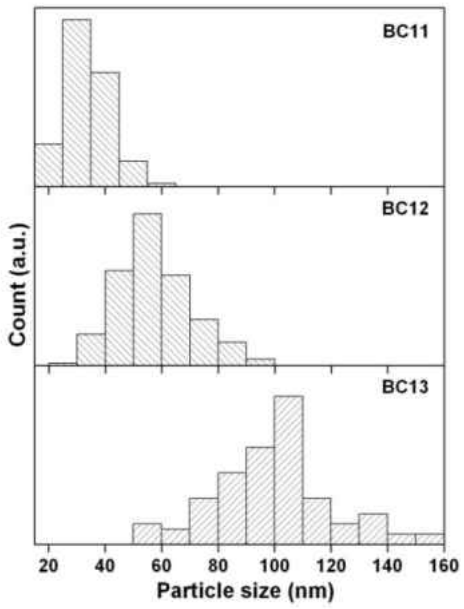

Figure 2.5: Particle size distribution of Base Catalyzed silica samples, BC11, BC12 & BC13 obtained from AFM image shown in Figure 2.4. Particle size increases with increase in base catalyst concentration.

2.5.3.2 Surface Chemical Analysis of Silica Nanoparticle Thin Films

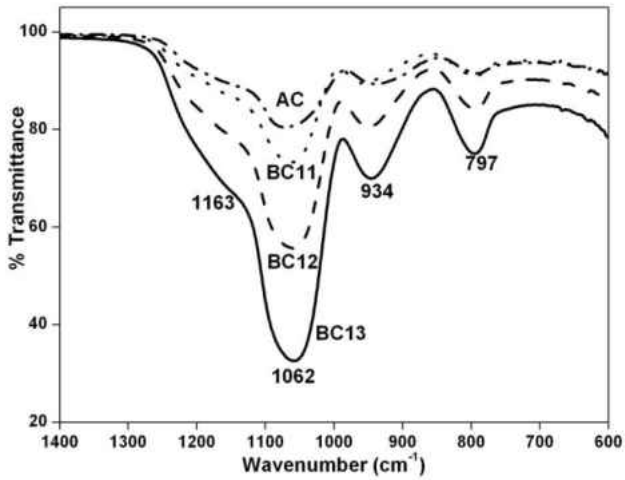

Figure 2.6: ATR FT-IR spectra of acid and base catalyzed silica samples in the regime of 1400 to 600 cm^{-1}.

In order to understand the chemical modifications occurring over the surface of the silica thin films, infrared spectral analysis was carried out. ATR FT-IR spectra of porous silica formed from base and acid catalyzed silica sol-gel in the regime of 600 to 1400 cm^{-1} is shown in Figure 2.5. The Si-O-Si vibrational modes, ascribed to symmetric stretching (TO_2) and asymmetric stretching (TO_3) were observed at about 800 cm^{-1} and 1060 cm^{-1} respectively. A strong shoulder observed at about 1150 cm^{-1} is related to the longitudinal optical component (LO_3) of the high frequency vibration of SiO_2. All the samples exhibited a band near to 940 cm^{-1}, which is assigned to stretching vibrations of Si-OH bonds. The absence of peak at 1400 cm^{-1} indicates that no residual ethoxy groups were present. Figure 2.7 shows the ATR FT-IR spectra of porous silica samples in the regime of 4000 to 1500 cm^{-1}. An O-H stretching region observed near 3400 cm^{-1} (Figure 2.7) where both H_2O (3300 cm^{-1}) and SiOH (3650 cm^{-1}) components are apparent.[20] An O-H bending vibration of water molecule is observed at 1630 cm^{-1} (Figure 2.7).[21] Intensity of Si-O-Si and Si-OH peaks increase with increase in concentration of base catalyst. AC and BC11 showed a low intense Si-O-Si and Si-OH peaks in comparison to BC12 and BC13.

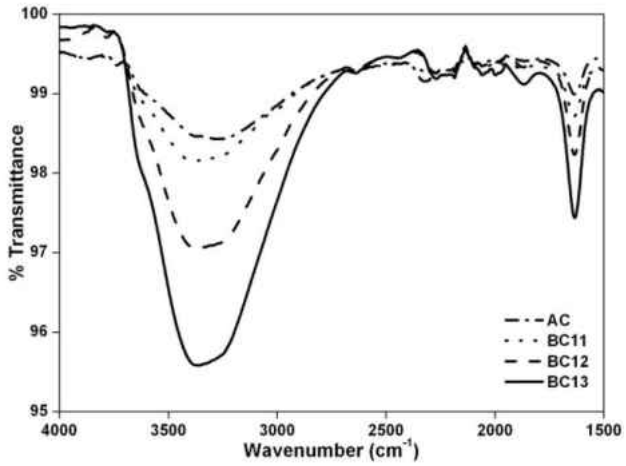

Figure 2.7: ATR FT-IR spectra of acid and base catalyzed samples in the regime of 4000 to 1500 cm^{-1}.

In order to delineate the intensities of Si-O-Si and Si-OH with the influence of catalyst, a Gaussian curve fit carried out for all the coatings. Figure 2.8 shows a Gaussian curve fit for the base catalyzed sample BC13. After resolving individual peaks, and the area under the peak was calculated towards their integrated intensity. Ratio of integrated intensity of Si-O-Si to Si-OH peaks at positions 1060 cm^{-1} and 940 cm^{-1} respectively were calculated. Calculated Si-O-Si to Si-OH ratio was found to be 1.85, 2, 2.4 and 2.6 for AC, BS11, BS12 and BS13 samples, respectively. Acid catalyzed silica coating (AC) showed the lowest ratio while the ratio shifted from 2 to 2.6 with the concentration of base catalyst. The relative increase in the peak integrated intensity ratio shows an increase in formation of Si-O-Si and a corresponding decrease in Si-OH intensity. In other words, an increase in base catalyst concentration increases the rate of condensation reaction of silanol group (Si-OH) to form siloxane groups (Si-O-Si).

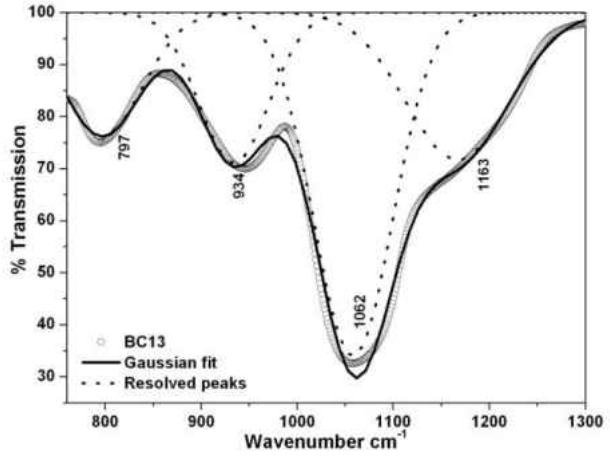

Figure 2.8: Gaussian peak fitting of the ATR FT-IR spectra for coating BC13; Individual peaks are resolved for relative intensity calculation.

Synthesis of silica by sol-gel process involves the formation of a colloidal suspension of siloxane groups (Si-O-Si) by condensation reaction of water with silanol (Si-OH). The mechanistic aspects of hydrolysis, alcohol and water condensation reactions are widely available in literature.[22, 23] The polymerization stages can be described as (i) polymerization of monomers to form primary particles, (ii) growth or agglomeration of primary particles into larger particles and (iii) linking of particles into chains to form a three dimensional network that extend throughout the liquid medium leading into a gel formation.[22, 23] Presence of acid or base catalyst has profound effect on the mechanism of the reaction and the final morphology.

Under acidic conditions, the alkoxide group is protonated in the first step. Si in the alkoxide becomes more electrophilic and starts reacting with the surrounding water molecule. The water molecule attacks from the rear and acquires a partial positive charge. At the same time, the positive charge of the protonated alkoxide is correspondingly

reduced resulting in the formation of a penta-coordinate transition state with significant SN_2 (Substitution Nucleophilic bimolecular) type character. At the end of the reaction alcohol leaves as a byproduct followed by inversion of silicon tetrahedron (Scheme 2.1).[22] This hydrolysis reaction is followed by polymerization reaction to form siloxane bonds by either an alcohol producing or water producing condensation reaction. The sequence of condensation requires both depolymerization (ring opening) and addition of monomers.[22] The rate of ring opening polymerizations and monomer addition reaction is dependent upon the solution pH. In this acidic pH range (pH<7), the solubility of silica is very low and the particle growth stops when the particle reach about 5 nm where the solubility and the size dependence solubility is greatly reduced. Thus, the resulting linear chain network will be composed mostly of small primary particles. This is in agreement with our AFM results (Figure 2.4A). In the base catalyzed condition, the water dissociates to produce nucleophilic hydroxyl anions in a rapid first step. Here also an SN_2 reaction mechanism is composed of the hydroxyl anion attacking the silicon atom and displacing the OR^- with inversion of the silicon tetrahedron (Scheme 2.2).[22]

Scheme 2.1: Acid catalyzed reaction mechanism of sol-gel silica

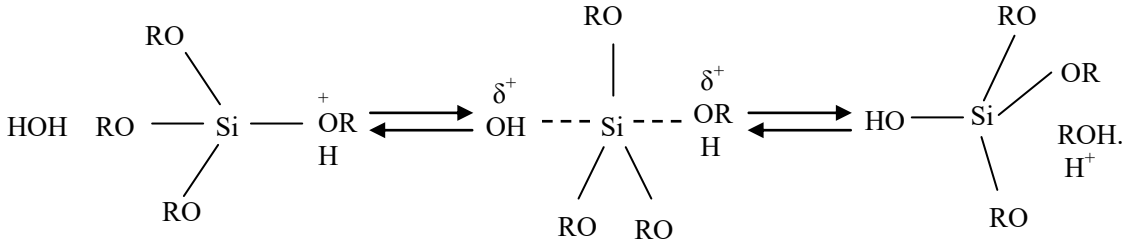

Scheme 2.2: Base catalyzed reaction mechanism of sol-gel silica

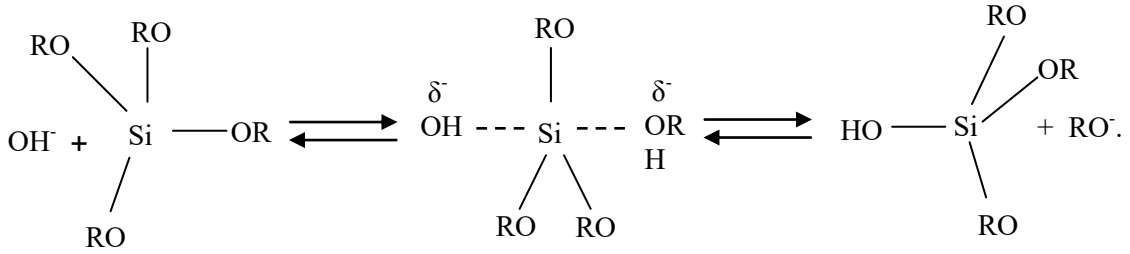

The growth occurs primarily through the addition of monomers to the more highly condensed particles rather than by particle aggregation. Due to greater solubility of silica and greater size dependence of silica above pH = 7, these larger particles grow by Ostwald ripening[23] mechanism whereby the particles grow in size and decrease in number as highly soluble small particles dissolve and precipitate again into larger less soluble particles. The growth stops when the difference in the solubility between the smallest and the largest particle becomes negligible. This type of growth results in highly branched silica cluster formation, as the particles are negatively charged and repel each other to form particulate sol. This is in agreement with our AFM images of base catalyzed coatings (Figure 2.1b-d). Thus acid catalysis resulted in dense film due to the formation of polymeric chains while base catalysis leading to porous film through particulate network formation. This is in agreement with the surface morphologies obtained from AFM studies.

2.5.3.3 Textural Properties of Silica Nanoparticle Thin Films

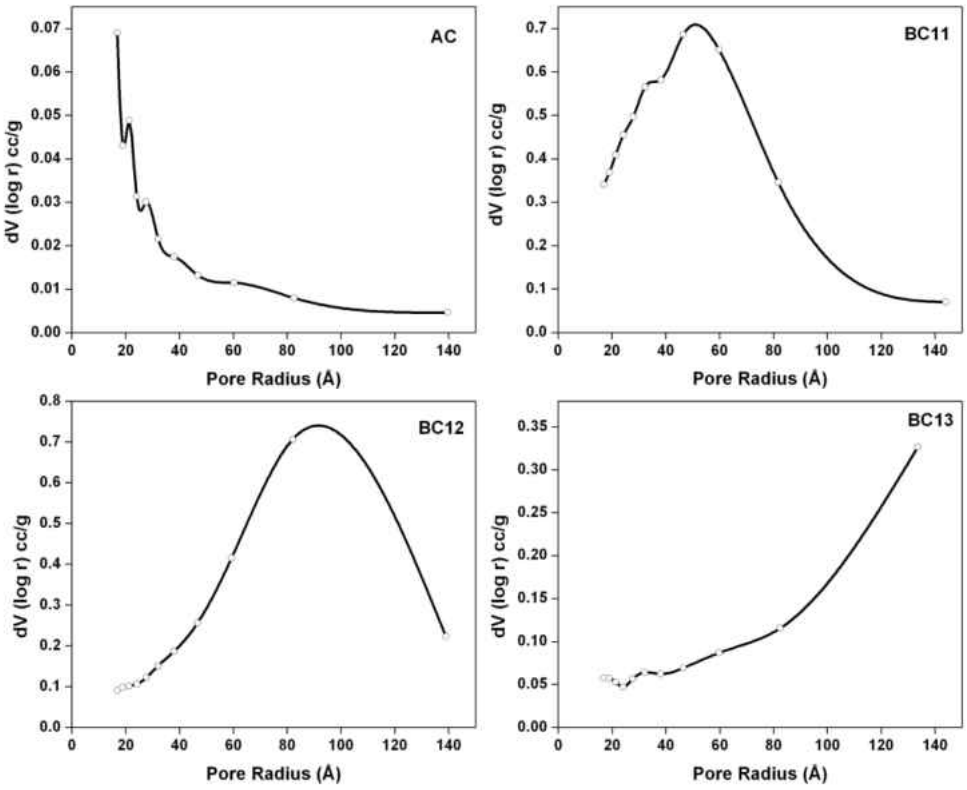

Figure 2.9: Pore size distribution (PSD) profiles of the acid- and base-catalyzed silica samples.

The textural properties (surface area, pore volume, pore size distribution) measurements were carried out on acid and base catalyzed silica samples. The pore size distribution (PSD) of acid and base catalyzed silica powders are shown in Figure 2.9. The sample AC (acid catalyzed) shows a smooth surface while base catalyzed samples showed a wider distribution. Further, the mean pore size shifted to larger values for base catalyzed samples. The observation of catalyst assisted tuning of PSD is in good agreement with the recent report.[24]

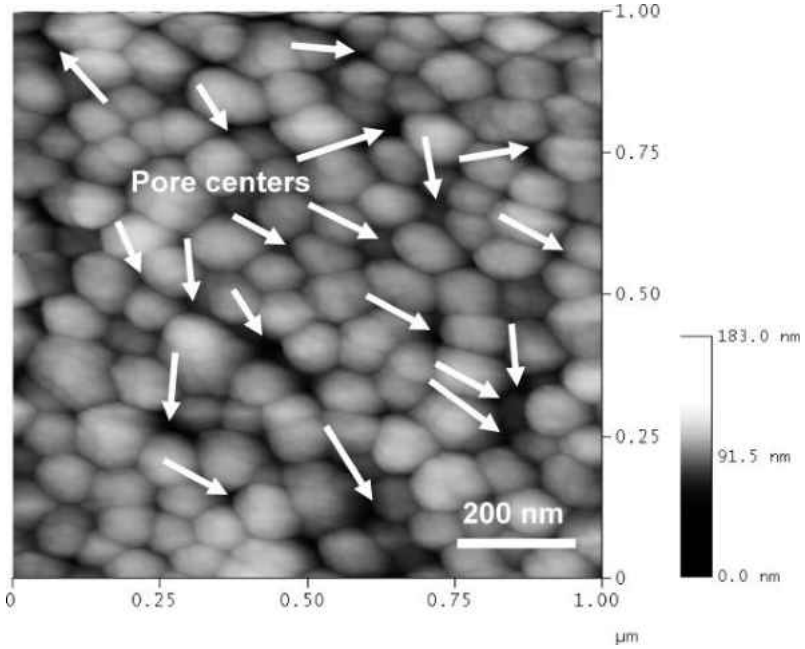

Figure 2.10: AFM image of base catalyzed silica (BC13) coating with pores in between silica particles. Arrows indicate the pore centers.

The textural properties of acid and base catalyzed silica samples are summarized in Table 2.3. BC11 powder showed higher surface area (~595 m^2/g) and highest porosity (49%) among all powders. This is due to the small particle size nature (~34 nm) of BC11. But BC13 powder composed of larger silica particles (~100 nm) showed the lowest surface area (~264 m^2/g) and porosity (36%) among the base catalyzed samples and the pore size of BC13 was more compared to that of BC11 and BC12. Figure 2.10 shows the AFM image of BC13 silica with pore centers trapped between silica particles (indicated through arrows). BC12 powder (~57 nm size particles) has a surface area in between BC11 and BC13 (~357 m^2/g) with a porosity of 42%. AC powders showed the lowest surface area (~199 m^2/g) and lowest porosity (5%) among all the powders. Acid catalyzed silica coatings results in atomically smooth coatings (RMS roughness ~0.34 nm). These coatings form a strongly bonded network structure, which gives them high

mechanical strength. Their low surface area in powder form can be correlated to their lower surface roughness in the case of thin film form. The density of porous silica is calculated from the pore volume fraction and bulk density of silica powder.

The density of porous silica obtained from base catalyzed silica increased as the concentration of base catalyst was increased. This is due to the formation of larger silica particles. As the particle starts growing, they form more and more dense particles, which are devoid of any pores. This is the reason for increase in density of porous silica with base catalyst concentration. Acid catalyzed silica showed the highest density (2.18 g/cc) among all the samples. This is due to the formation of highly dense network structure which had much lower porosity (5%) and is close to the bulk density (2.3 g/cc) of silica.

AFM scratch resistance measurements were conducted on these coatings to determine the resistance to low load scratching. W_2C coated AFM tip of 30 nm curvature radius (NSG 20/W2C, NT-MDT) was used to scratch the coatings. Base catalyzed silica coatings showed no resistance to scratch and exhibited a scratch depth closer to their film thickness (~100 nm) at a load of 10 μN, while acid silica coatings were highly resistant to scratch and exhibited a scratch depth of ~2 nm even at a load of 40 μN. Acid catalyzed coatings composed of smaller (less than 2nm) particles with many more particle-particle bonding resulting in higher coating strength. Base catalyzed silica coatings composed of larger particles with weaker and lower number of particle-particle bonding exhibited decreased coatings strength.[25]

Table 2.3: Textural properties of acid and base catalyzed silica powder

Coating	Surface area (m^2/g)	Pore volume (cc/g)	Pore radius (nm)	Porosity (%)	Density (g/cc) of porous silica
AC	198.87	0.02	1.7	5.0	2.18
BC11	594.46	0.42	4.7	49.1	1.17
BC12	356.61	0.32	8.2	42.2	1.33
BC13	263.97	0.25	14	36.1	1.47

2.5.3.4 Surface Roughness of Silica Nanoparticle Thin Films

The surface topographies of both the substrate and the film determines the quality of the coating in terms of their optical transmission.[26] The surface morphology of the coatings can lead to surface scattering and reduce the transmitted intensity. Optical transmission through a rough surface is considerably affected by scattering of light having wavelengths close to the magnitude of the surface features. The optical scattering loss at a rough interface between two media is described by the scalar scattering theory.[27-29] The corresponding scattering loss in transmitted intensity is given by

$$T^s = T_0 \left\{ 1 - \exp\left[-\left(\frac{2\pi (n_1 - n_2) R_q}{\lambda} \right)^2 \right] \right\} \tag{2.9}$$

and the surface scattering coefficient is given by

$$\alpha_{surf}(\lambda) = \left[\frac{2\pi (n_1 - n_2) R_q}{\lambda} \right]^2 \tag{2.10}$$

where T_0, λ, R_q n_1 and n_2 are the total transmittance, optical wavelength, RMS surface roughness, refractive index of film and air, respectively.[26] In order to quantify the surface topography, roughness measurements on the coatings were made using AFM. Table 2.4

shows the roughness and the particle size of these coatings. The root mean square (RMS) surface roughness of the base catalyzed silica increases with increase in base concentration due to an increase in the particle size (Table 2.3). As the particle size increases the surface packing density decreases, void space increases between the particles, and surface become rougher. Among the base catalyzed silica films, BC13 had the highest roughness of the order of 16 nm. In the case of acid catalyzed silica, the surface roughness is less (0.3 nm). This is because, when the particle size becomes smaller, the packing density increases and the surface become smooth (Table 2.3, Figure 2.4A). With the increase in particle size and film surface roughness, optical scattering loss also increases. It is clear from Table 2.4 that the scattering loss of AS is much less while BC13 showed the highest scattering loss among all samples. The scattering loss due to surface roughness in the transmitted intensity is less than 1% for all the samples, which is much less to affect any transmission loss. Since RMS surface roughness of all these films are less than 20 nm, these roughness is small enough not to cause any intense surface light scattering as long as the wavelength is longer than 200 nm.[30]

Table 2.4: Surface roughness & particle size of optical coatings from AFM image analysis

Coating	RMS roughness (nm)	Particle diameter (nm)	$\alpha_{surf}(\lambda)$ at 550nm	$\%\frac{T_s}{T_0}$
AC	0.3	5.9 ± 1.1	$3.0X10^{-6}$	$3.0X10^{-4}$
BC11	4.5	33.5 ± 8.8	5.2X10-4	$5.2X10^{-2}$
BC12	10.6	57.1 ± 12.9	$2.9X10^{-3}$	$2.9X10^{-1}$
BC13	16.2	99.5 ± 20.7	$6.7X10^{-3}$	$6.7X10^{-1}$

2.5.3.5 Optical Properties of Silica Nanoparticle Thin Films

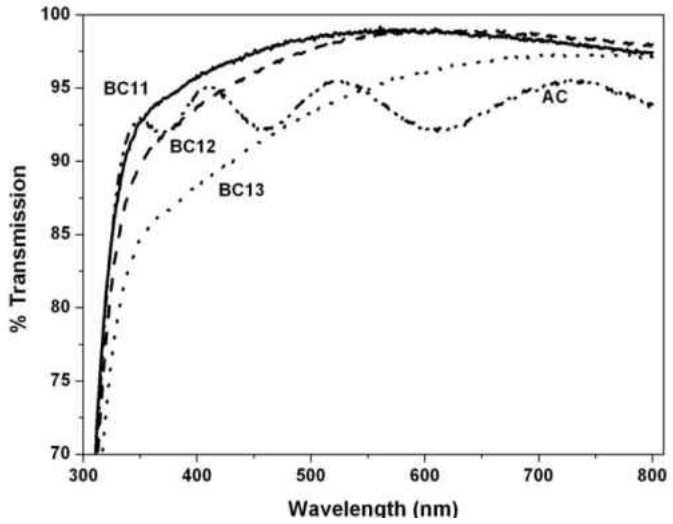

Figure 2.11: Transmission Spectra of acid and base catalyzed sol-gel silica coatings on glass substrate. BC11 showed the highest transmission among all the samples (99.03% at 548 nm).

UV-Visible optical transmission spectra of the acid and base catalyzed sol-gel silica coatings are shown in Figure 2.11. Base catalyzed silica coatings showed high optical transmission in the visible wavelength range, while acid catalyzed silica coatings exhibited lower optical transmission. The base catalyzed sol-gel silica with a TEOS to NH_4OH ratio of 1:1 (BC11) resulted in a transmission of 99.03% at 548 nm compared to that of the acid catalyzed silica (a transmission of 95.50%). This enhanced transmission is due to the lower refractive index of the base catalyzed silica, compared to the former, which is necessary to produce higher transmission on boron silicate glass. This observation can be correlated with the structural morphology the coatings (Figure 2.4). As discussed earlier the base catalyzed hydrolysis resulted in larger silica particles and the silica coatings prepared from the sol-gel solution have larger pores and higher surface

roughness. The porous centers can trap air and can result in an inhomogeneous refractive index coating. Since the refractive index of air is considered as unity, incorporation of air in highly porous coatings can result in a lower refractive index compared to that of less porous coatings. Although it is expected that BC13 sample should show higher transmission compared to other samples it exhibited a lower value. In BC13, the coating is composed of 100 nm diameter silica clusters and the sizes of the void space between these clusters are comparable to the size of the clusters. With the increase in void space, there will be a corresponding increase in light scattering at wavelengths closer to their size. This results in lower transmission of BC13 compared to that of BC11.[3]

2.5.3.6 Refractive Index and Thickness of Silica Nanoparticle Thin Films

The refractive index of these coatings can be calculated by constructing continuous envelops T_M and T_m around the maxima and the minima of the interference fringes.[31] If the substrate refractive index is s, the value of film refractive index, n is given by[32]

$$n^2 = N + \left(N^2 - s^2\right)^{1/2} \tag{2.11}$$

where

$$N = 2s\frac{T_M - T_m}{T_M T_m} + \frac{s^2 + 1}{2} \tag{2.12}$$

If n_1 and n_2 are the refractive indices at two adjacent maxima (or minima) at λ_1 and λ_2, the thickness d is given by,

$$d = \frac{\lambda_1 \lambda_2}{2\left(\lambda_1 n_2 - \lambda_2 n_1\right)} \tag{2.13}$$

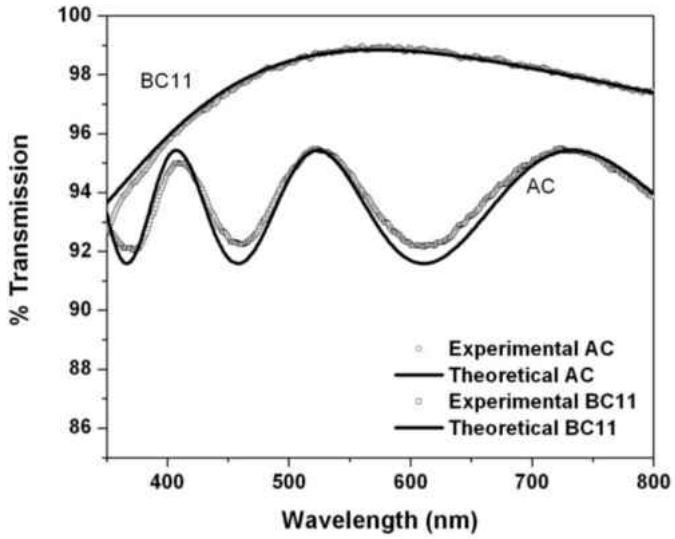

Figure 2.12: Comparison of theoretical and experimental transmission spectra of base and acid catalyzed silica coatings on glass substrate.

Film Star software was used to model the refractive index and the thickness of these coatings and was matching well with the experimental results obtained from ellipsometric measurements. Figure 2.12 shows a comparison of the experimental data versus theoretical transmission spectra of the base and acid catalyzed sol-gel silica coatings. The theoretical profile agrees well with the experimental results.

The acid catalyzed sol-gel silica coatings are usually denser in nature compared to that of the base catalyzed silica coatings. The multiple interference peaks of the acid catalyzed silica coating showed that these coatings were thicker in nature, while the base catalyzed silica coatings were thin as indicated by their transmission spectra. Film thickness increases with viscosity and dip coating speed (pull or drain rate).[33] Both acid and base silica coatings were prepared with the same withdrawal rate of 8.5 cm/min. The variation in thickness between acid and base catalyzed silica can be directly correlated to the viscosity of the sol-gel solution (Table 2.2). Viscosity of acid catalyzed silica was 2.66

mPa.s while that of base catalyzed silica varied between a close range of 1.92 to 1.84 mPa.s. In the case of acid catalyzed silica, strongly bonded network structure makes the sol more viscous than the loosely bonded particulate structure obtained in the case of base catalyzed silica.[25] Among the base catalyzed silica, BC11 showed higher viscosity while BC13 showed lower viscosity. This can be correlated to the presence of higher interaction forces present between larger concentration of small silica particles as compared to that of BC12 and BC13 where the interaction forces are low due to smaller concentration of large size silica particles.[34] However the variation in viscosity among the base catalyzed silica sol-gel solutions was marginal and insufficient to produce noticeable thickness variation among base catalyzed silica coated samples. Table 2.5 presents the calculated thickness, refractive index, and other optical properties of the films. The calculations also showed that the refractive index of the sol-gel silica coatings were less than that of the substrate, which is a different form of silica and is highly dense in nature. The lower refractive index of sol-gel silica is due to the effect of the incorporation of porosity. Acid catalyzed silica coatings showed a higher refractive index (1.443 at 550nm) compared to that of base catalyzed silica coatings (1.335 at 550nm) over the substrates of boron silicate microscopic glass slides (1.53 at 550nm). The maximum transmission values were due to the tuned refractive indices and the horizontal location of the maximum peak was due to altered film thickness, which would not affect transmission. Thus by varying the concentration of base catalyst, which results in modifications of porosity it is possible to optimize the refractive index and percentage of transmission.

Table 2.5: Optical properties of silica coatings made by acid and base catalyzed sol-gel chemistry

Coating	Thickness	Refractive index	Maximum %transmission	Wavelength of maximum transmission
AC	635 ± 2 nm	1.443 ± 0.001	95.5	521 nm
BC11	110 ± 2 nm	1.335 ± 0.001	99.0	548 nm
BC12	107 ± 2 nm	1.340 ± 0.001	99.0	609 nm
BC13	105 ± 2 nm	1.395 ± 0.001	97.3	714 nm
Substrate (Boron silicate glass)	2 mm	1.530 ± 0.001	92.0	550 nm

2.5.4 Conclusion

Porous silica thin films were prepared by sol-gel method by dip coating technique in the presence of acid and base catalysts. The coatings showed variation in morphology depending on nature of the catalyst used. While acid catalysis resulted in smoother surface, base catalyzed coatings exhibited a coarse, porous surface. Infrared spectral analysis showed an increase in Si-O-Si peak intensity in the case of base catalysis, due to an increase in condensation reaction of silanol group (Si-OH) results in coarse particles. Because of coarse particle morphology, base catalyzed samples exhibited larger surface area and pore volume, while acid catalyzed samples showed lower surface area and pore volume due to smooth surface. Bases catalyzed silica coatings showed superior optical transmission, higher surface roughness and lower refractive indices, while acid catalyzed silica showed less porous and non-particulate network structure with a lower optical transmission. Base catalyzed samples provided a greater flexibility in controlling the particle size, pore size, refractive index and hence optical coatings suitable for antireflective applications. However, the mechanical strength of the acid catalyzed coatings was found to be superior to that of base catalyzed coatings due to the stronger

particle-particle binding. The present work shows that by controlling the porosity and particle size, it is possible to attain almost 99% transmission in the visible range. In general, this approach can be useful for preparing sol-gel based porous antireflective optical coatings.

2.5.5 References

(1) Cao, M.; Song, X.; Zhai, J.; Wang, J.; Wang, Y., *J. Phys. Chem. B* **2006**, *110*, 13072.

(2) Yoldas, B. E., *Appl. Optics* **1980**, *19*, 1425.

(3) Yoldas, B. E.; Partlow, D. P., *Appl. Optics* **1984**, *Vol. 23*, 1418.

(4) Thomas, I. M., *Appl. Optics* **1988**, *27*, 3356.

(5) Suzhu, Y.; Terence, K. S. W.; Kantisara, P.; Xiao, H., *J. Vac. Sci. Technol. B* **2002**, *20*, 2036.

(6) Biswas, P. K.; Devi, P. S.; Chakraborty, P. K.; Chatterjee, A.; Ganguli, D.; Kamath, M. P.; Joshi, A. S., *J. Mater. Sci. Lett.* **2003**, *22*, 181.

(7) Cook, L. M.; Lowdermilk, W. H.; Milam, D.; Swain, J. E., *Appl. Opt.* **1982**, *21*, 1482.

(8) Floch, H. G.; Priotton, J.-J., *Ceram. Bullet.* **1990**, *69*, 1141.

(9) Hiller, J. A.; Mendelsohn, J. D.; Rubner, M. F., *Nat. Mater.* **2002**, *1*, 59.

(10) Liu, Y.; Ren, W.; Zhang, L.; Yao, X., *Thin Solid Films* **1999**, *353*, 124.

(11) Thomas, I. M., *Appl. Optics* **1992**, *31*, 6145.

(12) Wu, G.; Wang, J.; Shen, J.; Zhang, Q.; Zhou, B.; Deng, Z.; Fan, B.; Zhou, D.; Zhang, F., *High Temp. - High Press.* **2000**, *32*, 687.

(13) Yang, H.-S.; Choi, S.-Y.; Hyun, S.-H.; Park, H.-H.; Hong, J.-K., *J. Non-Cryst. Solids* **1994**, *221*, 151.

(14) Prevo, B. G.; Hwang, Y.; Velev, O. D., *Chem. Mater.* **2005**, *17*, 3642.

(15) Janotta, M.; Katzir, A.; Mizaikoff, B., *Appl. Spectro.* **2003**, *57*, 823.

(16) Guangming Wu; Jue Wang; Jun Shen; Tianhe Yang; Qinyuan Zhang; Bin Zhou; Zhongsheng Deng; Bin Fan; Dongping Zhou; Zhang, F., *Mater. Sci. Eng. B* **2000**, *78*, 135.

(17) Bautista, M. C.; Morales, A., *So. Energy Mater. So. Cells* **2003**, *80*, 217.

(18) Takada, S.; Hataa, N.; Seino, Y.; Fujii, N.; Kikkawa, T., *J. Appl. Phys.* **2005**, *97*, 113504.

(19) Thomas, I. M., *Appl. Optics* **1986**, *25*, 1481.

(20) Du, X. M.; Almeida, R. M., *J. Sol-Gel Sci. Tech.* **1997**, *8*, 377.

(21) Graubner, V. M.; Jordan, R.; Nuyken, O.; Schnyder, B.; Lippert, T.; Kotz, R.; Wokaun, A., *Macromolecules* **2004**, *37*, 5936.

(22) Brinker, C. J.; Scherer, G. W., *Sol-Gel Science: The Physics and Chemistry of Sol-Gel Processing*, Academic Press, Inc., New York, 1990.

(23) Iler, R. K., *The Chemistry of Silica*; Wiley: New York, 1979.

(24) Bhagat, S. D.; Kim, Y.-H.; Ahn, Y.-S.; Yeo, J.-G., *Micropor. Mesopor. Mater.* **2006**, *96*, 237.

(25) Wang, J.; Wu, G.; Shen, J.; Yang, T.; Zhang, Q.; Zhou, B.; Deng, Z.; Fan, B.; Zhou, D.; Zhang, F., *J. Sol-Gel Sci. Tech.* **2000**, *18*, 219.

(26) Ulmeanu, M.; Serghei, A.; Mihailescu, I. N.; Budau, P.; Enachescu, M., *Appl. Surf. Sci.* **2000**, *165*, 109.

(27) Beckmann, P.; Spizzichino, A., *The Scattering of Electromagnetic Wave from Rough Surface*; Pergamon: Oxford, 1963.

(28) Krc, J.; Smole, F.; Topic, M., *Prog. in Photov, Research and Applications* **2003**, *11*, 15.

(29) Poruba, A.; Fejfar, A.; Remes, Z.; Springer, J.; Vanecek, M.; Kocka, J.; Meier, J.; Torres, P.; Shah, A., *J. Appl. Phy.* **2000**, *88*, 148.

(30) Xu, Y.; Fan, W. H.; Li, Z. H.; Wu, D.; Sun, Y. H., *Appl. Optics* **2003**, *42*, 108.

(31) Manifacier, J. C.; Gasiot, J.; Fillard, J. P., *J. Phys. E* **1976**, *9*, 1002.

(32) Swanepoel, R., *J. Phys. E* **1983**, *16*, 1214.

(33) Kim, G.-S.; Hyun, S.-H., *J. Non-Crys. Solids* **2003**, *320*, 125.

(34) Cheng, N.-S.; Law, A. W.-K., *Powder Technology* **2003**, *129*, 156.

CHAPTER 3: ORGANIC AND INORGANIC INTERACTIONS OF AGED NANOPARTICLES

3.1 Introduction

Nanoparticles (NPs) of size less than 100 nm exhibit remarkably different properties from their bulk counterparts displaying a potential for their use in various application, ranging from catalysis[1], photonics[2], optoelectronics[3], biological labeling[4], and targeted drug delivery.[5] The homogenization, dispersion, and stabilization of NPs in suspension are of primary importance for their high performance in many applications.[6] Since, the surface energy of NPs is significantly higher than that of larger particles[7], NP sols are extremely sensitive to the changes in their physicochemical environment such as pH, ionic strength, temperature, and concentration, which in turn influences their agglomeration in suspensions.[8] A stable colloidal NP suspension can be obtained by balancing the attractive van der Waals forces acting between the NPs against the repulsive Columbic forces induced by the surface adsorbed species. Such suspensions are often formed by providing steric or electrostatic stability by adding chemical additives to adjust the suspension properties such as viscosity, ionic strength, pH[9] or by surface functionalization of the NPs themselves.[10] However, addition of chemicals may add more complexity to the system and may be undesirable. For example pure NP suspensions are required for targeted drug delivery and cellular uptake, [5, 11] where the interactions between NPs and biomacromolecules, cells, or living tissues determine the toxicity.[8] Surface charge modification of NPs through acidic or basic buffer treatment and subsequent dispersion in water is an attractive route to form stable suspension suitable for variety of applications.[11]

Cerium is a rare earth element of the lanthanide series. The oxide form of cerium (CeO_2) has been widely used for glass polishing[12]. Currently cerium oxide nanoparticles (CNPs, also known as nanoceria) have been used in catalytic conversion[13], solid oxide fuel cell[14], and oxygen gas sensor.[15] Recent advancements in bionanomaterials research have proven the superoxide dismutase (SOD) mimetic radical scavenging activity of CNPs in protecting cells against oxidative stress.[16-18] The unique property of CNPs, which makes them suitable for potential applications, originates from the increased concentration of Ce^{3+} ions with the reduction in the size of the CNPs and their relative ease to undergo reversible redox reaction between Ce^{3+} and Ce^{4+} states (due to the presence of oxygen vacancy).[19] Due to their biocompatibility, small size and cell membrane permeation capabilities, CNPs conjugated with ligand proteins has been identified as potential drug carriers, that can target and release drugs to cancerous cells. Our earlier studies have shown that the efficiency of surface modified CNPs to successfully target cancer cells and undergo internalization mainly depends on the stability of the CNP-ligand binding which is often influenced by their surface chemistry.[5] The nature and long-term stability of the modified surface charges on CNPs and their behavior under different physiological conditions is relatively unknown and a detailed study is necessary to explore the physicochemical changes taking place on the CNP surface under these conditions. Similarly, for applications such as in chemical mechanical polishing (CMP), the interaction between CNP and silica surface in the slurry can be greatly influenced by the changes in the surface charges of CNPs.[20] Hence, a molecular level understanding of surface reactions occurring with time, temperature, concentration of CNPs and associated

changes in surface charges, is essential to develop applications where long term surface stability of NPs is highly desirable. Herein we report the surface charge variations of CNPs measured in terms of their Zeta (ζ) potentials (ZPs) as a function of aging time, dispersion temperature, concentration, CNP annealing temperature, doping and their influence in targeted drug delivery and chemical mechanical polishing.

3.2 Materials and Methods

3.2.1 Synthesis of CNPs

Cerium nitrate hexahydrate ($Ce(NO_3)_3.6H_2O$, 99%, Aldrich) was used as a precursor for synthesizing CNPs.[21] To 0.1 M aqueous cerium nitrate solution (500 ml), 1.0 N ammonium hydroxide (NH_4OH, Alfa Aesar) solution was added to maintain the pH at 9 and stirred for four hours. Deionized water (18.0 mΩ) purified in a Barnstead NANOpure Diamond system was used for all the experiments. The resultant solution was stirred and allowed to settle overnight. The precipitates were washed with water multiple times to remove any weakly adhered ions on the surface and dried at 100 °C to obtain the CNPs. It is reported earlier[22] that, the precipitation of $Ce(NO_3)_3.6H_2O$ precursor solution requires oxidation of Ce^{3+} to Ce^{4+} ions in solution. The addition of excess NH_4OH to the Ce^{3+} precursor solution leads to the oxidation of Ce^{3+} to Ce^{4+} ions. Due to their low basicity and higher ionic charge, Ce^{4+} ions undergo strong hydration to form hydroxide complex.

$$\left[Ce(H_2O)_n\right]^{4+} + yH_2O \rightarrow \left[Ce(OH)_y(H_2O)_{n-y}\right]^{(4-y)+} + yH_3O^+ \quad (3.1)$$

This complex will undergo polymerization. In aqueous solution, due to its polar nature, H_2O tend to take the excess protons (H^+) away from the hydroxide complex.

$$\left[Ce(OH)_y(H_2O)_{n-y}\right]^{(4-y)+} + 4H_2O \rightarrow CeO_2.n(H_2O) + (4-y)H_3O^+ \quad (3.2)$$

The precipitation of the hydrated $CeO_2.n(H_2O)$ species leads to the formation of CNPs according to the dissolution precipitation mechanism. The precipitated particles were centrifuged and washed with deionized water multiple times to remove any impurities attached to the surface. Resultant NP powder was dried at 100 °C and was analyzed by both X-ray diffraction (Rigaku Model) and high-resolution transmission electron microscopy (Philips Tecnai operated at 300KeV).

3.2.2 Tuning the Surface Charges of CNPs

NPs tuned with positive or negative surface charge groups usually form strong electrostatic bonds with ligand molecules having oppositely charged groups. To study the stability of modified surface charges of CNPs, both positively and negatively charged CNPs were prepared by treating with different acidic and alkaline pH buffers in the range of pH 3-13. All these buffers were prepared by adding known amount of concentrated HCl or KOH (as necessary to adjust the pH) to 0.05 M KCl solution. This preparation ensured similar types of ions (H^+, OH^-, K^+, and Cl^-) in all buffers. The surface charges of CNPs were varied by treating 5 mg of the CNPs with 5 mL of pH buffer at a 1 mg/mL final concentration. The suspension was ultrasonicated for an hour and stirred using a magnetic stirrer for another 24 hours followed by centrifuging and re-dispersing in deionized water at a concentration of 1 mM. The centrifuging and re-dispersion cycles

were repeated until the pH of the CNP solution becomes neutral. The ZP value of the CNP solution was measured using Zetasizer (Nano-ZS) from Malvern Instruments. The instrument uses a combination of Laser Doppler Velocimetry (LDV) and Phase Analysis Light Scattering (PALS) in a technique called M3-PALS to measure the NP electrophoretic mobility. The details of this method can be found elsewhere.[23] The electrophoretic mobility *(u_ζ)* is then converted to ZP according to the Henry equation[24]:

$$u_\zeta = \frac{2\zeta\varepsilon}{3\eta} f(\kappa a) \tag{3.3}$$

where ζ is the ZP of the particles, ε and η are respectively the dielectric constant and viscosity of the medium and *f(ka)* is the Henry's function. κa is a measure of the ratio of the particle radius to electrical double layer thickness. The value of *f(ka)* was chosen as 1.5 (Smoluchowski approximation) as the zeta potential measurements were conducted in aqueous medium. The original ZP values obtained were rounded to three significant figures and are represented as approximations.

3.2.3 Time, Temperature and Concentration Dependent Aging of CNPs

Time, temperature and concentration dependent ZP variations of CNPs were monitored at different intervals and the effect of aging conditions on the ZPs of CNPs were investigated in detail. To study the influence of aging time on the ZPs of CNPs, solutions of both positively and negatively charged CNPs (obtained by acidic and alkaline buffer treatment) kept under normal atmospheric conditions (room temperature) were monitored for several months and their respective ZP variations were plotted against aging time. Role of aging temperature on ZPs of CNPs was determined by heating the positively

charged CNP in solution at different temperatures and recording their changes at each temperature. Similarly to study the concentration dependent ZP variations, positively charged CNPs in solutions were diluted at different concentrations in the micromolar regime (concentrations of interest for cellular uptake studies) and their respective ZPs were reordered against their concentrations. In temperature dependent study, the ZPs of CNPs were compared with that of doped, annealed and micron ceria (purchased from Johnson Matthey) particles. Yttrium (Y) and ytterbium (Yb) were chosen to prepare doped CNPs as their ionic radii were respectively larger and smaller than that of pure cerium.

3.2.4 AFM Force Spectroscopy Measurements

Atomic force microscopy (AFM)-based Single Molecule Force Spectroscopy (SMFS)[5, 25-28] has proven to be one of the most versatile technique that can induce molecule level interactions on surfaces using functionalized probes and at the same time monitor these interaction forces in picoNewton resolution. SMFS were carried out to study the interaction between transferrin (Tf) protein and CNPs, using Solver pro Scanning Probe Microscopy (SPM) with a SMENA controller from NT-MDT, Moscow, Russia. We used Tf conjugated AFM probes (procedure for Tf-AFM probe conjugation is reported in our earlier publication[5]) with an average spring constant of 0.05 N/m and a tip curvature radius of ~10 nm for force measurements. Samples were prepared by drop coating CNPs on an atomically smooth silicon surface. The forces of interaction between Tf and CNPs were measured using SMFS on these samples by landing the probe tip on to the NP surface. Tf interacted strongly with the NP surface upon contact. The nature of the

bonding was influenced by the surface charge and surface chemistry of the NPs. Following the landing, the tip was retracted from the surface. This lead to the stretching of Tf and subsequent bond breakage between Tf and NPs. Quantitative information regarding the elastic stretching behavior of protein and their interactions with the NP surface can be obtained from the force curve analysis. The laser deflection-piezo displacement data obtained from the SMFS experiments were then converted to force against displacement of the tip from the sample surface using the following equation.

$$D(t) = z(t) - \delta(z)/s \tag{3.4}$$

where $D(t)$ is the distance between the AFM probe and the surface in nm, $z(t)$ is the piezostage displacement, $\delta(z)$ is the cantilever deflection in nanoampere (nA) and s is the sensitivity of the cantilever determined by calculating the slope of the part of the force-distance curve reflecting the bending of the cantilever obtained on silicon sample. The force $F(z)$ is calculated by using the Hooke's law for a linear elastic spring (cantilever) as

$$F(z) = k_c \delta(z)/s \tag{3.5}$$

where k_c is the spring constant of the cantilever.

Similarly, to study the interaction between silica surface and CNPs in CMP slurry, AFM-based force-distance spectroscopy measurements were carried out using AFM probes attached with 600 nm diameter silica bead. The average spring constant of the cantilever was 4.5 N/m. The forces of interaction between silica bead and CNPs drop coated on silicon were measured by lowering the probe tip close to the CNP surface and retracting it until the silica bead-CNP adhesion breaks. In both the cases, multiple force

measurements were carried out at different locations on CNPs coated silicon samples and the corresponding force values were plotted in the form of histograms.

3.2.5 Computational Details

The Density Functional Theory (DFT) calculations presented here were carried out with the plane-wave based Vienna *ab initio* simulation package (VASP).[29, 30] The electronic ground state is determined by using local density (LDA) approximation. We used LDA+*U* version with local part described by Ceperley-Adler functional. On site Coulomb and exchange interaction are treated by a single effective parameter U_{eff}=*U-J*. Plane waves are included up to an energetic cutoff of 415 eV, the electronic wave functions were described using the projected augmented wave (PAW) method and U_{eff}=5 eV.[31] These calculation parameters were recently employed for the investigation of ceria. It was shown that LDA+U_{eff} approximation demonstrates better agreement for geometry with experiment than GGA+*U* approach.[32] Energies of LDA+U_{eff} optimized structures were recalculated with Perdew-Burke-Ernzerhof (PBE) exchange-correlation functional using U_{eff}=5.5eV.[33] Supercells were chosen with at least 10 Å between replicas to remove spurious periodic interactions while Coulomb interaction between periodic charged images is compensated according to the procedure reported earlier.[34]

3.3 Results and Discussion

3.3.1 Time Dependent Surface Charge Modifications of Hydrated Nanoceria

The structural and morphological properties of CNPs were determined by X-ray diffraction (XRD) and high-resolution transmission electron microscopy (HRTEM).

From the HRTEM image, the mean particle size of CNPs was calculated to be ~8.2 ± 1 nm. Both XRD (Figure 3.1a) and selected area electron diffraction (SAED) (Figure 3.1b inset) patterns of CNPs display the cerium oxide fluorite structure.

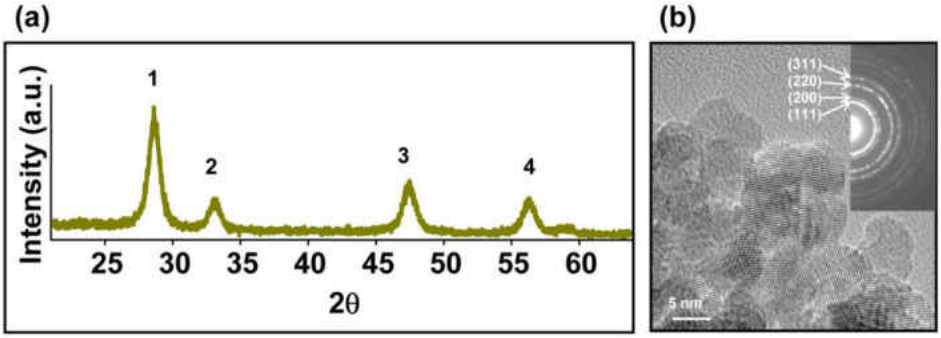

Figure 3.1: (a) XRD spectrum and (b) HRTEM image of fluorite structured CNPs. The peaks corresponds to positions 1, 2, 3 and 4 in the XRD spectrum represents the planes, (111), (200), (220) and (311), respectively (JCPDS 81-0792). The inset in the HRTEM image shows the SAED pattern of CNPs. The CNP particle size is ~8.2 ± 1 nm.

The surface charge of colloidal NPs is often addressed by measuring their ZP, an electrostatic potential that exist at the shear planes of the particles, related to both surface charge and the local environment of the particles. The pH at which the CNPs exhibit a ZP of magnitude close to zero (point of zero charge, PZC) is reported to be ~9.5.[11] The surface charge formulation on CNPs can be visualized as follows. When anhydrous cerium oxide is dispersed in water in the form of a colloidal suspension, it binds with H_2O molecules to form hydrated CeO_2. When the pH of the solution is less than the PZC of CNPs, hydrated CeO_2 absorbs a proton (H^+ ion) and forms a positive charged particle.[35]

$$CeO_2.n(H_2O) + nH_3O^+ \rightarrow CeO_2.n(H_3O)^+ + nH_2O, pH < PZC \quad (3.6)$$

Similarly when the pH of the solution is greater than the PZC of CNPs, hydrated CeO_2 looses an H^+ ion from the bound H_2O molecule and forms a negatively charged colloid particle.[35]

$$CeO_2.n(H_2O) + n(\mathrm{OH})^- \rightarrow CeO_2.n(OH)^- + nH_2O, pH > PZC \quad (3.7)$$

The interaction and the stability of the bond between hydrated CNPs and the H^+ or OH^- ions governs the sign and magnitude of the ZPs of CNPs.

To determine the effect of aging time on the surface charges, ZPs of CNP solutions were monitored at regular intervals of time. Figure 3.2a shows the ZP of fresh CNPs (at a concentration of 1 mM) aged at room temperature for 0, 40, and 220 days respectively. Immediately after dispersing freshly prepared CNPs in water (0 day), a high positive ZP of +43.0 mV was observed. This can be attributed to the formation of positively charged species (H_3O^+ ions) on CNP surface due to the increased dissociation of the H_2O molecules at CNP oxygen vacancies[36, 37], according to the eq. (1). Also, CNPs exhibited a time dependent shift in ZP from positive to negative charges (+43.0, -3.90, and -31.5 mV at 0, 40 and 220 days respectively). To further explore the surface charge dynamics, time dependent studies were carried out on both positive and negative charged CNPs formed via acidic or basic pH buffer treatment (CNPs were re-suspended in deionized water after the buffer treatment). Figure 3.2b shows the ZPs of CNPs (1 mM) after treatment with a range of pH buffers (pH 3-14). CNPs treated with acidic pH buffers retained positive ZPs, while CNPs treated with alkaline pH buffers (pH 8-13) exhibited a gradual shift in ZP from positive to negative with increasing pH. The PZC of CNPs was observed at pH 10 (Figure 3.2b). After about 40 days, the ZP of all the positively charged CNPs changed

to negative values, while the magnitude of negatively charged CNPs increased to higher negative values. The ZP measured in 220 days for all the pH treated CNPs exhibited high negative ZPs values in the range of -26.0 to -36.0 mV. The time dependent shift in ZP from positive to negative values observed could be due to the replacement of the positively charged surface species from the NP surface (H^+) with the negatively charged counter ions (OH^- ions). Figure 3.2c shows the schematic of potential distribution around positive and negative charged CNP surface. It is clear that CNP surface affects the distribution of H_3O^+ and OH^- ions in the surrounding interfacial region, resulting in an increased concentration of counter ions (ions of opposite charge) close to the CNP surface. Though, both aging and pH buffer treatment resulted in different surface charges, the size of CNPs remained the same in all these conditions. The HRTEM images of freshly prepared positively charged CNPs and aged negatively charged CNPs are shown in Supporting Information Figure 3.10.

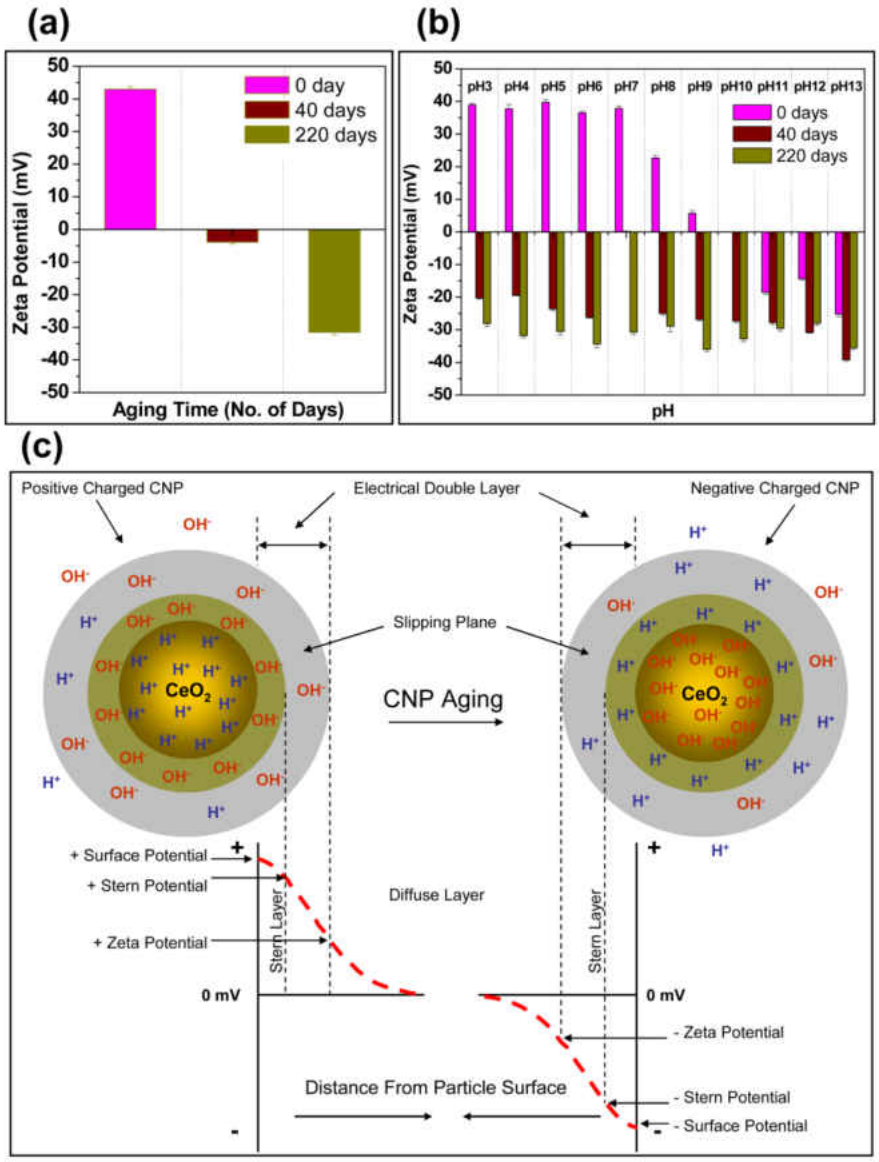

Figure 3.2: ZPs of freshly prepared CNPs (a) and CNPs treated with different pH buffers (b) aged at room temperature. Acid buffer treated CNPs resulted in positive ZP and alkaline buffer treated CNPs resulted in negative ZP. Both untreated and buffer treated CNPs exhibited a time dependent shift of ZP from positive to negative charge. Negatively charged CNPs became more negative with time. (c) Schematic of potential distribution around positive and negative charged CNPs. Development of a net charge at the NP surface affects the distribution of H^+ and OH^- ions in the surrounding interfacial region, resulting in an increased concentration of counter ions (ions of charge opposite to that of the particle) close to the NP surface. During aging, positive charged CNPs display a tendency to replace their surface protons with OH^- counter ions.

3.3.2 Proton and Hydroxyl Ion Interactions with Hydrated Nanoceria

DFT simulation studies were conducted to understand the nature of molecular level interactions of H_3O^+ and OH^- ion with CNPs dispersed in water. For simplicity, we modeled the CNP-H_3O^+/OH^- ion interaction by considering a small CNP as shown in Figure 3.3a, that has a size of ~1 nm and $C_{19}O_{32}$ stoichiometry. This is a minimal octahedral NP derived from a bulk cerium oxide fluorite lattice, exposing the most stable (111) facets in accordance with the HRTEM images of the CNPs shown in Figure 3.1b.

The bulk ionized water structures have been elucidated by previous *ab initio* molecular dynamics simulations,[38] which found that fast proton exchange processes lead to fluctuation between so-called Eigen (H_3O^+)[39] and Zundel ($H_5O_2^+$)[40] forms of hydronium. Modeling of H_3O^+ ion interaction with CNP demonstrates that hydronium ion is unstable in the vicinity of CNP and decays to an H^+ ion and a H_2O molecule. This H^+ ion forms a covalent bond with CNP while the H_2O molecule gets adsorbed on to the CNP surface by forming two hydrogen bonds. We performed CNP-H_3O^+ interaction simulations with the distance between CNP and hydronium oxygen fixed at 3Å. Calculations predict that H_3O^+ ion on the vicinity of CNP is highly unstable and will undergoes barrierless dissociation reaction by proton transfer from the H_2O molecule to the CNP surface. This forms a metastable CNP-H^+ complex. However, after the equilibrium is established, the H^+ species on the CNP surface is replaced with OH^- ion from the solution and forms more stable CNP-OH^- complex.

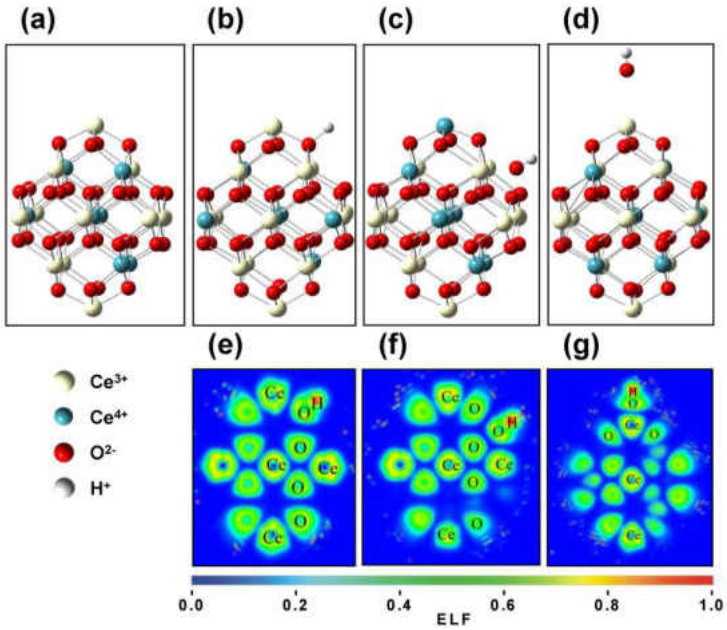

Figure 3.3: Atomic structure model of octahedral $(CeO_{2-x})_{19}$ x=0.32, NP obtained from the bulk cerium oxide by cutting through (111) planes with different molecular species adsorbed: (a) bare CNP, (b) CNP with H^+ ion, (c) CNP with OH^- ion adsorbed on the facet, (d) CNP with OH^- ion adsorbed on the vertex. Ce^{3+}, Ce^{4+}, O^{2-} and H^+ ions are shown as light yellow, blue, red and gray spheres, correspondingly. Projection of electron localization function (ELF) on different planes passing through CNP and adsorbed (e) H^+ ion, (f) OH^- ion (facet) and (g) OH^- ion (vertex). Color code blue (ELF=0) and red (ELF=1.0) represents full absence and full presence of electron pair in actual point of space. Adsorbed H^+ ion forms a covalent bond with CNP while ionic bonding is observed between adsorbed OH^- ion and CNP.

Figure 3.3b-d show the possible ways to conjugate H^+ and OH^- ions on the CNP.[41] For H^+ ion, there is only one possible way to be bonded to the oxygen atom on the NP surface as shown in Figure 3.3b. There are two equilibrium positions for OH^- ions; one on the facet position, in between the three oxygen atoms terminating at the CNP surface (Figure 3.3c) and the other position on the vertex of CNP near the cerium ion (Figure 3.3d). At latter position, OH^- interacts significantly stronger with CNP as the main contribution towards binding interaction comes from the attractive Columbic interaction between cerium ion at vertex position and the neighboring OH^- ion (Figure 3.3d). In the former case, interaction

is partially screened by surface oxygen ions and the value of the binding energy (BE) obtained between the OH^- ion and facet cerium ion is smaller compared to that of vertex cerium ion. H^+ ion is covalently bonded to the CNP's surface oxygen while OH^- ion is ionically bonded as seen from the electron localization function (ELF) [42] plots shown in Figure 3.3e-g.

The BE calculated for CNP-H^+ and CNP-OH^- complexes as a function of the number of ligands (adsorbed species) are shown in Figure 3.4a. Here, the BE between CNP and n number of adsorbed X species is defined as:

$$BE = \left[E(CNP) + nE(X) - E(CNP - nX)\right]/n \tag{3.8}$$

where *E(CNP), E(X)* and *E(CNP-nX)* are the ground state energies for CNP, X species and CNP with adsorbed X species, respectively.

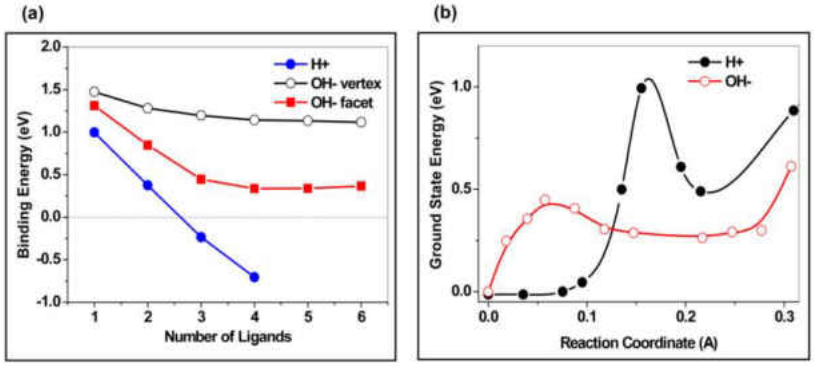

Figure 3.4: (a) Binding energies per adsorbed specie of OH^- and H^+ ions with CNPs as a function of number of ions on the NP's surface. The BE calculations predict that $Ce_{19}O_{32}$ NP is able to adsorb maximum two H^+ ions (positive ZP) while its ability for OH^- adsorption is much higher. Adsorption of OH^- ion on CNP's vertex and facets positions are considered. Larger BE values were observed for the interaction of OH^- ion with Ce^{3+} ion placed on the vertex of CNP. (b) The ground state energy profile for OH^- and H^+ ions as a function of their distance from the equilibrium position on the CNP's facet that defines the zero point of energy. CNP with adsorbed OH^- ion is more energetically favorable since it's BE is about 0.31 eV larger than the corresponding value for H^+ ion adsorption.

As seen from Figure 3.4a, OH^- ions interact with CNP significantly stronger than H^+ ions. This interaction is attractive and its magnitude decreases with the number of additional OH^- ions adsorbed by CNP. Between the two different equilibrium positions for OH^- ions, the vertex position is found to be the more stable than facet position. Adsorption of OH^- ions to these sites leads to a slight decrease in the BE values from 1.47 eV for one adsorbed OH^- ion to 1.12 eV for six adsorbed OH^- ion species. In the case of CNPs with a facet adsorbed OH^- ion, the BE profile display a steady decreases from 1.31-0.37 eV. At the same time, BE values of H^+ ions steadily decreases and becomes negative for n>2, indicating that the interaction between protonated CNP and H^+ ions becomes repulsive and no further attachment of H^+ ions are possible on a doubly protonated CNP of the size studied here.

Experimental results revealed ZP changes from positive to negative values with time while the theoretical results predict that the CNPs exhibits a favorable tendency to bond to OH^- ions in solution. Such experimentally observed changes in the sign of ZP indicate that kinetics of proton-hydroxyl ion exchange on CNP surface play a major role in the ZP sign reversal. To explain such behavior, the potential energy of the elementary processes responsible for the rates of the ion adsorption and desorption were calculated. Potential energy profiles were evaluated for a number of configurations constructed by varying the distance between CNP and adsorbed species (reaction coordinates). Geometrical optimization was performed for each structure by fixing the distance between adsorbed species and CNP (relaxed scan). The obtained results are presented in Figure 3.4b. The CNP-H^+ NPs are formed during the barrierless decay of Eigen cations near the vicinity of

CNPs as described above. The removal of H^+ ion from CNP proceeds through the breaking of the covalent bond between CNP and H^+, which requires the overcoming of the energy barrier. Subsequently, the OH^- ions have to overcome another energy barrier to form coordination bond with CNP surface and to reach the most stable low energy state. This energy barrier originates from the redistribution of *f*-electron density in the CNP during the approach of OH^- ion from the large distance to the equilibrium position on the CNP surface. The redistribution of Ce^{3+} and Ce^{4+} ions in CNPs are shown in Figure 3.3a, d, respectively.

These computational results can be summarized as follows. When CNPs are introduced into the aqueous solution, their surface is protonated through the fast, diffusion controlled process (diffusion of protons from the solution to the CNP surface), resulting in the formation of kinetically favorable CNP-H^+ complexes. This is the possible reason for the initial positive ZP observed for freshly prepared CNPs dispersed in water. During the aging process, the OH^- ions slowly overcome the potential barrier to association and occupy the thermodynamically favorable positions by displacing the H^+ ions from the CNP surface. Thus, performed calculations explain the inversion in ZP observed during the aging of freshly prepared CNPs.

3.3.3 Influence of Solution Temperature on the Surface Charge Modifications

Since our experimental and theoretical observations indicate a kinetically controlled change in the CNP surface charge, we tested the effect of the parameters that can influence the kinetics, such as temperature and concentration. To determine the effect of the temperature on ZP, the CNP solutions (1mM) were heated in situ from 25 to 65 °C

and their ZPs were measured at each temperature after reaching an equilibration time of 5 minutes (Figure 3.5a). Freshly prepared CNPs exhibit ZP values of +43.0, +40.4, +36.2, +36.1, -5.68 mV at 25, 35, 45, 55, and 65 ^{o}C, respectively. Starting from 25 ^{o}C, the CNPs exhibited a decreasing trend in ZP (with marginal variations) until 55 ^{o}C. However, at 65 ^{o}C, CNPs exhibited an inversion in ZP sign from the positive to the negative value (-5.68 mV at 65 ^{o}C).

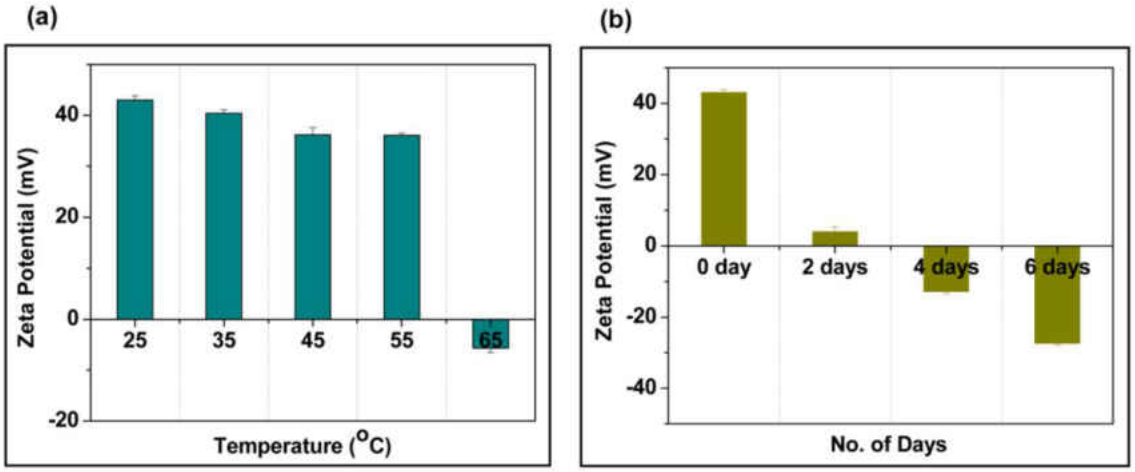

Figure 3.5: (a) ZPs of freshly prepared CNPs measured instantaneously at different temperatures within an equilibration time of 5 minutes. (b) ZPs of fresh CNPs heated at 65 ^{o}C and measured at 25 ^{o}C. ZP of CNPs gradually shifts from positive to negative values with time.

The nature of ZP changes observed while heating the CNP solution at different temperatures were similar to that observed in the case of CNP solutions aged for several days. Though heating at 65 ^{o}C resulted in negatively charged CNPs, cooling the solution back to room temperature displayed positive ZPs of lower magnitudes. Hence, another set of experiment was initiated where the CNPs solution was maintained at 65 ^{o}C for several hours and the ZP was measured after cooling the suspension back to 25 ^{o}C. Figure 3.5b shows the ZP of CNP solution heated at 65 ^{o}C and measured at 25 ^{o}C. In a span of 6 days,

the ZP of the CNPs became stable and exhibited a negative ZP of -27.3 mV at room temperature (25 ^{o}C). Further heating of CNPs solution did not result in considerable ZP variations. These observations suggest that during the heat treatment, accelerated dissociation of protons from CNP surface occurs, which is partially reversible. The following association of CNPs with the hydroxyl ions from the solution proceeds at a slower rate.

The charge density of CNPs is related to their ZP as follows[43],

$$\sigma_d = \left(8\varepsilon_0\varepsilon_r RTC\right)^{1/2} \sinh\left(\frac{zF\zeta}{2RT}\right) \tag{3.9}$$

where R is the ideal gas constant, T is the absolute temperature, F is Faraday's constant, z is the valency of the ions, σ_d is the charge density of the NP, ε_0 is the electrical permittivity of a vacuum, ε_r is the dielectric constant of the electrolyte assumed to be equal to that of water and C is the concentration of the ions in the electrolyte in mol/L. H_2O undergoes self dissociation and form H_3O^+ and OH^- ions. For pure deionized water (pH 7) the concentrations of both the H_3O^+ and OH^- ions are equal to $c=10^{-7}$ *mol/L.* Table 1 displays the charge density calculated for CNPs in suspension heated to different temperatures. The charge density varies with the temperature in a manner similar to that of ZP.

Table 3.1: Calculated charge density (σd) at different temperatures using dielectric constant for water (εr) and ZP

T, °C	ε_r (H_2O)	ε (x 10^{-10} F/m)	ζ, mV	σ_d (x 10^{-6} C/m^2)
25	78.4	6.95	43.0	1.10
35	74.6	6.64	40.4	0.973
45	71.3	6.33	36.2	0.820
55	68.2	6.03	36.1	0.784
65	65.1	5.74	-5.68	-0.111

3.3.4 Concentration Dependent Surface Charge Modifications

Most of the applications, including the biomedical ones, utilize the CNPs in nanomolar to micromolar concentrations.[11] The cell-CNP and protein-CNP interactions depend mainly on their surface charges. Hence, it is important to understand ZP behavior of CNPs at these concentrations. For this purpose, ZP of CNP solutions were tested at 1 mM, 100 μM and 10 μM concentrations. Figure 3.6 shows ZPs of CNPs with respect to CNP concentrations measured at 25 ^{o}C. CNPs exhibited a ZP of +43.0, +6.70, -24.1 mV at 1 mM, 100 μM and 10 μM concentrations, respectively. A gradual shift in the ZP from positive to negative values was observed with decrease in molar concentration of the CNPs. Concentration dependent ZP variation was observed only below 1 mM concentration of CNPs and the ZP remained at +43.0 mV for all concentrations above 1mM. At 100 and 10 μM, the decrease in magnitude of positive ZP and its shift towards negative values indicates that the CNPs have a more pronounced tendency to associate with OH^- ions at lower concentrations. When CNPs are diluted to micromolar concentrations, the rate of H_2O dissociation and formation of H_3O^+ and OH^- ions could decrease. This leads to less interaction between CNPs and kinetically favorable H_3O^+

ions and may effectively reduce the magnitude of positive charge on CNP surface (Figure 3.6). Since many of the drug/gene delivering ligands such as transferrin[5] and folic acid[44] exhibit negative ZP at physiological pH, the concentration dependent ZP changes indicates that it is essential to treat freshly prepared positively charged CNPs with ligand molecules at concentration above 1 mM for achieving better CNP-ligand conjugation and then dilute the resultant solution to the concentration of interest. Treating CNPs with ligand molecules directly at micromolar and nanomolar concentrations may lead to poor ligand adsorption due to the columbic repulsion between the ligands and negatively charged CNPs.

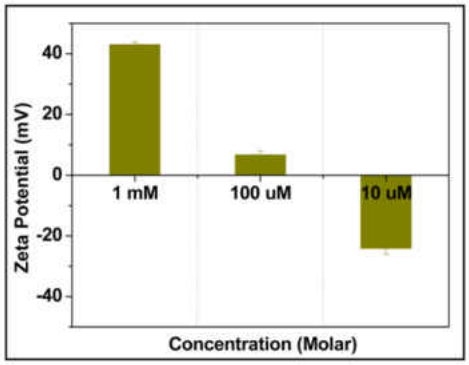

Figure 3.6: ZPs of fresh CNPs measured at 25 ^{o}C at different CNP concentrations. ZP of CNPs shifts from positive to negative with decrease in CNP concentration.

3.3.5 Role of Oxygen Vacancy Defects on the Surface Charge Tunability

The CNPs attracted great interest recently for various catalytic applications due to their ability to easily absorb and release oxygen. This oxygen storage capacity is a result of the oxygen vacancy formation in the CeO_2 lattice.[45] In the earlier sections, we have discussed the role of external material parameters such as aging time, solution temperature and solution concentration on the ZPs of CNPs. To determine the effect of intrinsic material

properties such as oxygen vacancies on ZP values, CNPs were annealed at high temperature (100 ^{o}C, 500 ^{o}C and 900 ^{o}C) in air atmosphere for 2 hour to decrease the oxygen vacancy concentration. Annealing CNPs at high temperature in the air is expected to result in faster oxygen diffusion and subsequent annihilation of oxygen vacancies.[46] Following this annealing, the ZPs of CNPs (1 mM) were measured and the results are presented in Figure 3.7a. The CNPs annealed at 500 ^{o}C exhibit a low positive ZP value of +1.65 mV as compared to those annealed at 100 ^{o}C (+43.0 mV). The CNPs annealed at 900 ^{o}C exhibit a high negative ZP of -20.6 mV. Compared to CNPs, cerium oxide microparticles (micron ceria) of size ~1-2 μm exhibit the highest negative ZP value of -29.0 mV. The gradual shift in ZP from positive to negative values of annealed CNPs and micron ceria can be correlated with the temperature dependent annealing of oxygen vacancy defects in cerium oxide. The lower concentration of oxygen vacancies in annealed CNPs would result in a reduced production of H_3O^+ as the rate of H_2O dissociation decreases. This reduces the rate of proton adsorption by CNPs and increases the rate of adsorption of more favorable OH^- ions, resulting in a gradual increase in the magnitude of negative ZP with the annealing temperature.

The ZP variations observed with CNPs annealed at different temperatures indicate that oxygen vacancies could play a major role in tuning the ZP of CNPs. It is well known that by addition of trivalent dopants, the concentration of oxygen vacancy in CNPs can be tuned to a great extent.[45] Depending on the size of these dopant cations, the oxygen vacancy concentration can be either increased or decreased. To understand the effect of doping on the ZP of CNPs, yttrium (Y) and ytterbium (Yb) were doped into CNPs. When

Ce^{4+} ions are substituted by large rare earth trivalent ions such as Y^{3+}, the oxygen vacancies are created due to the partial reduction of Ce^{4+} to Ce^{3+}. The formation of oxygen vacancies can be represented as

$$2Y^{3+} \xrightarrow{CeO_2} 2Y' + Vo'' + \frac{1}{2}O_2 \tag{3.10}$$

where $Vo^{''}$ is the oxygen vacancy concentration. Earlier we reported that ceria contains ~3.39×10^{20} cm^{-3} oxygen vacancies and doping with larger ion such as Y^{3+} can leads to an increase in the lattice parameter (0.0552% increase with 20% doping) and thus to an increase in the oxygen vacancy concentration (1.77% increase with 20% doping) whereas a decrease in lattice parameter (0.223% decrease with 20% doping) and oxygen vacancy concentration (7.97% decrease with 20% doping) was observed while doping with smaller ions like Yb^{3+}.[47] The doped CNP solution was then heated at different temperatures and their ZP variations with temperature were monitored (Figure 3.7b). Similar to the undoped CNPs, the magnitude of positive ZP of doped CNPs decreases with increase in temperature, and at 65 ^{o}C, the doped CNPs exhibits a negative ZP. At the temperatures below 50 ^{o}C, 20% yttrium doped CNPs (Y-CNPs) exhibits the highest positive ZP while 20% ytterbium doped CNPs (Yb-CNPs) exhibits the lowest ZP as compared to that of pure CNPs (Pure-CNPs). The magnitude of ZP decreased in the same order, Y-CNPs>Pure-CNPs>Yb-CNPs. This observation can be correlated with the oxygen vacancy defect concentration in these CNPs, which decrease in the same order Y-CNPs>Pure-CNPs>Yb-CNPs.[47] The results directly indicate that CNPs with more oxygen vacancies engage in the dissociation of H_2O and undergo higher proton

adsorption. Inconsistent trends in the data at 55 and 65 ^{o}C could be due to the difference in the reaction kinetics of pure and doped CNPs at that temperature range.

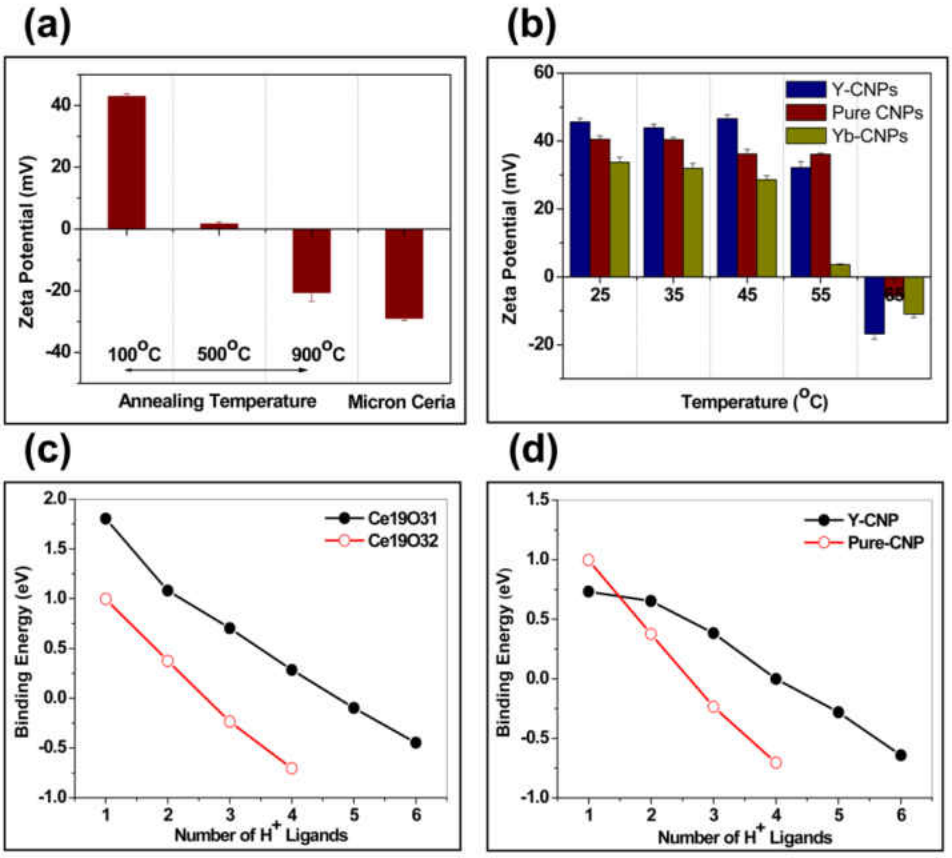

Figure 3.7: (a) ZPs of annealed CNPs and micron ceria and (b) ZPs of doped CNPs measured at different temperatures. ZP of doped CNPs changed from positive to negative with increase in measurement temperature. 100 ^{o}C annealed CNPs displayed positive ZP while high temperature annealed CNPs displayed negative ZP. Micron sized cerium oxide particles showed the highest negative ZP among all the samples. (c) Binding energy plot of H^{+} ion with CNPs as a function of number of H^{+} ions on the CNP surface. Plotted results correspond to perfect octahedral $Ce_{19}O_{32}$ CNP (open circles) and CNP with one surface oxygen vacancy $Ce_{19}O_{31}$ (filled circles). (d) Binding energy plot of H^{+} ion with pure CNP ($Ce_{19}O_{32}$) and yttrium doped CNP ($Ce_{15}Y_{4}O_{30}$) as a function of the number of H^{+} ions on the CNP surface. The BE decreased in the order, Y-CNP>Pure-CNP similar to the amount of oxygen vacancy concentration in these samples.

3.3.6 Oxygen Vacancy Modulated Nanoceria-Proton Interactions

To better understand the role of oxygen vacancies in determining the ZP of CNPs, DFT simulations were carried out by considering different levels of protonation varying from one to six H^+ ions on the surface of CNP. Figure 3.7c shows the BE profile of H^+ ions interacting with CNP as a function of H^+ ion added. The effective BE decreases with increase in the number of H^+ ions attached to the CNP surface, and additional protonation becomes thermodynamically unfavorable after the BE value passes through zero. After the oxygen vacancies are introduced into the CNP, the proton binding energy also decreases; whereas, the zero BE value is reached after addition of four protons (vs. two for CNP without the vacancy). These data indicate that CNPs with higher concentration of the oxygen vacancies will associate with more H^+ ions and will have high positive ZP values. Similar trend is observed for Y-CNP. As one can see from Figure 3.7d, Y-CNP exhibits higher binding affinity towards H^+ ions as indicated by their high BE values, and is capable to attach as many protons as CNP with one vacancy. These computational results explain why the pure CNPs display higher positive ZPs as compared to the annealed CNPs and the doped CNPs display higher positive ZPs as compared to pure CNPs.

3.3.7 Physicochemical Implications in Chemical Mechanical Planarization (CMP) Slurry

Cerium oxide based slurries have been used for glass polishing for several years.[12] Recently the use of ceria slurries has been extended to chemical mechanical polishing (CMP) processes[48] in the microelectronics industry such as those involving the

fabrication of integrated circuit (IC) photomasks[49], glasses for the liquid crystalline displays (LCD)[50] and interlayer dielectrics (ILDs).[51] The interaction of abrasive particle with the polishing surface has been a major focus of study in CMP.[52, 53] Since the polishing process occurs in an aqueous environment (pH 7-10)[52], pH dependent charge modifications can occur on both ceria and silica glass surfaces. The literature reported value of PZC of silica is about 1.5-2.8.[54] Hence, silica exhibits a high negative ZP at pH $\geq$ 7.[52] It is reported that the removal of material from the surface of silica glass during CMP polishing process is attributed to a temporary attachment of CNPs to the silica glass surface through surface chemical bonds.[52]

The surface charges of CNPs can influence the ceria-silica interaction and play a major role in the polishing process. In pH 7-10 range, CNPs can exhibit positive, neutral or negative surface charge depending on the nature of NPs used for polishing. Our experimental observations display that freshly prepared CNPs (PZC ~10) exhibit positive ZP values of +37.8, +22.7, and +5.68 mV, respectively when treated with pH 7-9 buffers and 0.00 mV when treated with pH 10 buffer. However, within 40-220 days of aging in water, the ZP of these CNPs switched to the negative ZP values of -30.7, -28.9, -36.0, and -32.0 mV respectively. These negative charged CNPs could experience a strong repulsion from the negatively charged silica and could adversely affect the atomic scale polishing process. Hence, it is necessary to use freshly prepared CNPs rather than aged CNPs for CMP process.

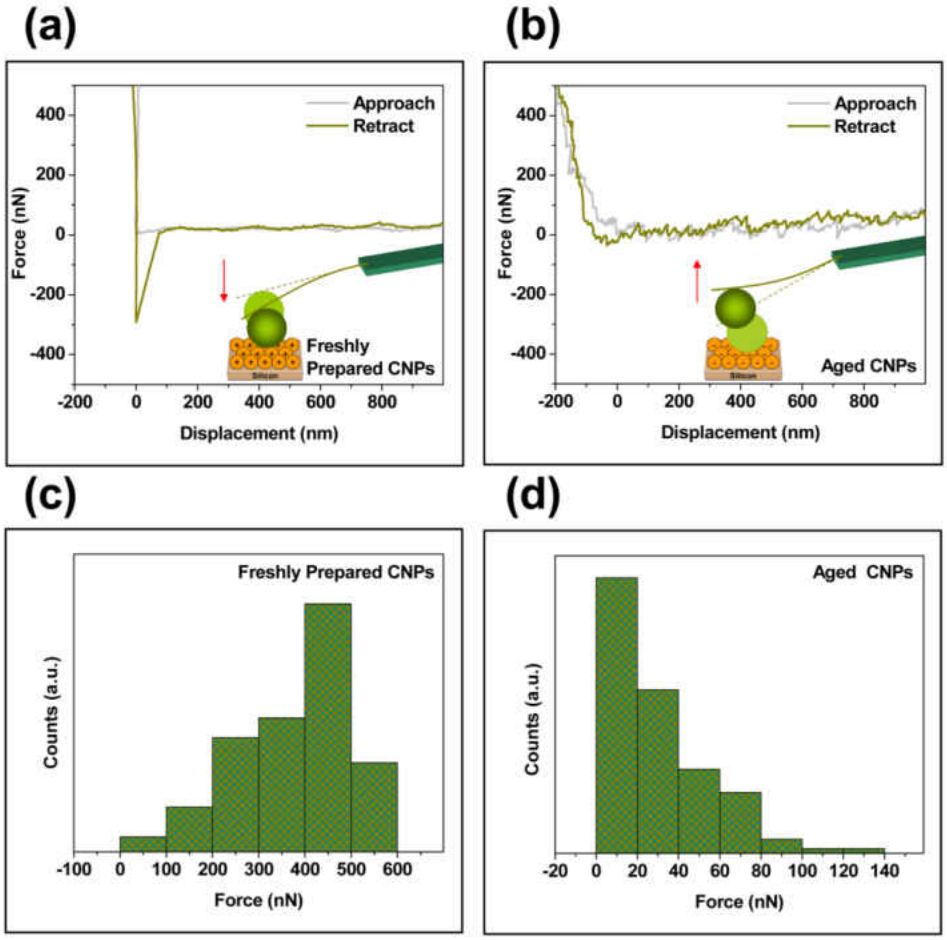

Figure 3.8: Force-distance spectroscopy of 600 nm silica bead interacting with (a) Freshly prepared (+43.0 mV ZP) CNPs, (b) Aged (-23.0 mV ZP) CNPs, The corresponding force histograms are shown in (c) and (d). Force histograms are obtained by conducting multiple SMFS measurements on each sample. The total number of force values analyzed are n=130 in each case.

Figure 3.8a-d shows the F-D spectroscopy data of a silica bead of size 600 nm interacting with freshly prepared (+43.0 mV ZP) and aged (-23.0 mV ZP) CNPs in water (negative charges on CNPs are obtained by natural aging process and not by any basic buffer treatment). It is clear that the adhesion force of silica bead with freshly prepared CNPs is much higher compared to aged CNPs. The force distribution shows that the peak interaction force between the silica bead and freshly prepared CNPs is in the range of

400-500 nN (with a maximum at 600 nN), while for aged CNPs, the peak interaction force is observed mostly between 0-20 nN (with a maximum at 140 nN). F-D spectroscopy data reveals that it is important to use freshly prepared CNPs for CMP slurry to achieve a better adhesion of the ceria abrasive particles with silica surface. The experimental observations from the CNP aging process indicate that the NPs could undergo charge reversal with time and temperature during CMP process especially in basic pH conditions. Hence, it is important to start with freshly prepared slurry of positively charged CNPs for CMP process. It is also essential to monitor the changes in the ZP to determine the shelf life of the slurry depending upon the storage time and especially operational temperatures.

3.3.8 Biomedical Implications in Targeted Drug Delivery: Transferrin-Nanoceria Interactions

Ligand-receptor mediated drug delivery and imaging systems have been a major focus of study in nanomedicine.[55, 56] NPs conjugated with cellular targeting proteins[5, 57, 58] (mostly anionic) and polymer transfection agents[59, 60] (mostly cationic) are a topic of active biomedical research. This conjugation relies predominantly on the high surface area and surface charge of the NPs, leading to the columbic attachment.[5, 11] Under physiological pH conditions, the ligands may exhibit positive or negative charges with respect to their PZC. Hence, depending on the nature of ligand molecules, NPs engineered with appropriate surface charges are often chosen to achieve better NP-ligand binding.[11]

Tf is a protein used in biological systems for the transportation and supply of iron to the growing cells. It has been used as a targeting ligand to deliver a wide range of therapeutic

agents including NPs to cells that overexpress transferrin receptor (TfRs)[5, 57, 61-64] In order to demonstrate the influence of ZP changes with aging time on Tf-CNP interactions, SMFS measurements were conducted on both freshly prepared and 220 days aged CNPs using Tf coated AFM probes.

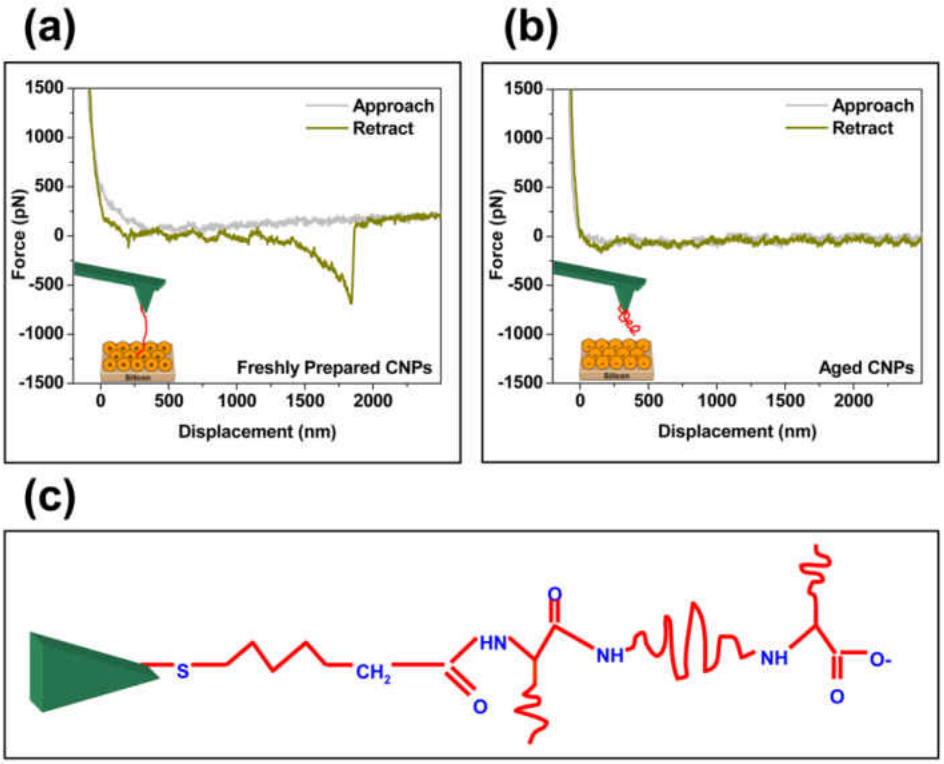

Figure 3.9: Single Molecule Force Spectroscopy of Tf protein interacting with (a) Freshly prepared (+43.0 mV ZP) CNPs and (b) Aged (-23.0 mV ZP) CNPs. Freshly prepared CNPs exhibits higher binding affinity with Tf compared to aged CNPs. (c) Schematic diagram of transferrin conjugated AFM tip.

Figure 3.9a, b shows the force spectroscopy of Tf coated AFM probe (Figure 3.9c) interacting with freshly prepared (+43.0 mV ZP) and aged (-23.0 mV ZP) CNPs. It is clear from the figure that the Tf interacts strongly with freshly prepared CNPs while it experienced much less and mostly negligible interaction with aged CNPs. The unbinding forces obtained here in both the cases are similar to that observed in our earlier studies of

Tf interaction with acidic/basic buffer treated surface charge tuned positive (+36.0 mV) and negative (-35.0 mV) CNPs (discussed in forth chapter).[5] Our experiments shows that Tf experienced a strong unbinding force of 100-400 pN with freshly prepared CNPs while it experienced an unbinding force of much less magnitude (0-75 pN) with aged CNPs. These observations suggests that it is essential to use freshly prepared positively charged CNPs for achieving better Tf-CNP conjugation to ensure a strong electrostatic attraction. CNPs dispersed in water can undergo charge reversal with time and their ability to form bonds with Tf can deteriorate due to the strong columbic repulsion between the negatively charged CNPs and the negatively charged Tf.

3.4 Summary

Surface charges on the NPs have implications not only on the dispersibility but also on many potential applications. The present experimental results along with theoretical calculations presented here demonstrate that CNPs, when dispersed in water, exhibit positive ZP due to a kinetically driven proton adsorption process. However, the initial positive ZP of CNPs is highly unstable and prolonged exposure to water and/or increasing the solution temperature and/or lowering the CNP concentration, the CNPs undergo a ZP switch from positive to negative values by adsorbing OH^- ions on the NP surface, resulting in thermodynamically stable state. Positively charged CNPs exhibit a better adhesion interaction with silica beads (chemical mechanical planarization applications) and a better ligand conjugation with cellular targeting transferrin protein (drug delivery applications), while negatively charged CNPs displayed negligible adhesion to both protein and silica beads. The data presented here demonstrate that the

surface charges of CNPs play a vital role in their efficient use as a targeted drug delivery carrier in biomedical or as an abrasive material in CMP applications. In order to tailor the surface properties of colloidal NPs for intended applications, it is essential to understand the dynamics of the physicochemical surface reactions occurring on the colloidal NP surface.

3.5 References

1. Lewis, L. N., *Chem. Rev.* **2002,** 93 (8), 2693.

2. Maier, S. A.; Brongersma, M. L.; Kik, P. G.; Meltzer, S.; Requicha, A. A. G.; Atwater, H. A., *Adv. Mater.* **2001,** 13 (19), 1501.

3. Kamat, P. V., *J. Phys. Chem. B* **2002,** 106 (32), 7729.

4. Nicewarner-Peña, S. R.; Freeman, R. G.; Reiss, B. D.; He, L.; Peña, D. J.; Walton, I. D.; Cromer, R.; Keating, C. D.; Natan, M. J., *Science* **2001,** 294 (5540), 137.

5. Vincent, A.; Babu, S.; Heckert, E.; Dowding, J.; Hirst, S. M.; Inerbaev, T. M.; Self, W. T.; Reilly, C. M.; Masunov, A. E.; Rahman, T. S.; Seal, S., *ACS Nano* **2009,** 3 (5), 1203.

6. Karimian, H.; Babaluo, A. A., *J. Euro. Ceram. Soc.* **2007,** 27 (1), 19.

7. Artelt, C.; Schmid, H.-J.; Peukert, W., *J. Aerosol Sci.* **2005,** 36 (2), 147.

8. Qi, L.; Sehgal, A.; Castaing, J.-C.; Chapel, J.-P.; Fresnais, J.; Berret, J.-F.; Cousin, F., *ACS Nano* **2008,** 2 (5), 879.

9. Brant, J.; Lecoanet, H.; Hotze, M.; Wiesner, M., *Environ. Sci. Technol.* **2005,** 39 (17), 6343.

10. Tang, E.; Cheng, G.; Ma, X.; Pang, X.; Zhao, Q., *Appl. Surf. Sci.* **2006,** 252 (14), 5227.

11. Patil, S.; Sandberg, A.; Heckert, E.; Self, W.; Seal, S., *Biomaterials* **2007,** 28 (31), 4600.

12. Duncan, L. K., *Glass Ind.* **1960,** 41, 412.

13. Croy, J.; Mostafa, S.; Liu, J.; Sohn, Y.; Heinrich, H.; Cuenya, B., *Cat. Lett.* **2007,** 119 (3), 209.

14. Eguchi, K.; Setoguchi, T.; Inoue, T.; Arai, H., *Solid State Ionics* **1992,** 52 (1-3), 165.

15. Jasinski, P.; Suzuki, T.; Anderson, H. U., *Sens. Actuators B.* **2003,** 95 (1-3), 73.

16. Chen, J.; Patil, S.; Seal, S.; McGinnis, J. F., *Nat. Nano* **2006,** 1 (2), 142.

17. Das, M.; Patil, S.; Bhargava, N.; Kang, J. F.; Riedel, L. M.; Seal, S.; Hickman, J. J., *Biomaterials* **2007,** 28 (10), 1918.

18. Tarnuzzer, R. W.; Colon, J.; Patil, S.; Seal, S., *Nano Lett.* **2005,** 5 (12), 2573.

19. Deshpande, S.; Patil, S.; V. N. T. Kuchibhatla, S.; Seal, S., *App. Phys. Lett.* **2005,** 87 (13), 133113.

20. Suphantharida, P.; Osseo-Asare, K., *J. Electrochem. Soc.* **2004,** 151 (10), G658.

21. Babu, S.; Schulte, A.; Seal, S., *Appl. Phys. Lett.* **2008,** 92 (12), 123112.

22. Pei-Lin, C.; Chen, I.-W., *J. Am. Ceram. Soc.* **1993,** 76 (6), 1577.

23. Mezei, A.; Mészáros, R., *Langmuir* **2006,** 22 (17), 7148.

24. Henry, D. C., *Proc. R. Soc. London* **1931,** A133 (821), 106.

25. Oesterhelt, F.; Oesterhelt, D.; Pfeiffer, M.; Engel, A.; Gaub, H. E.; uuml; ller, D. J., *Science* **2000,** 288 (5463), 143.

26. Florin, E. L.; Moy, V. T.; Gaub, H. E., *Science* **1994,** 264 (5157), 415.

27. Smith, B. L.; Schaffer, T. E.; Viani, M.; Thompson, J. B.; Frederick, N. A.; Kindt, J.; Belcher, A.; Stucky, G. D.; Morse, D. E.; Hansma, P. K., *Nature* **1999,** 399 (6738), 761.

28. Oberhauser, A. F.; Marszalek, P. E.; Erickson, H. P.; Fernandez, J. M., *Nature* **1998,** 393 (6681), 181.

29. Kresse, G.; Hafner, J., *Phys. Rev. B* **1993,** 47 (1), 558.

30. Kresse, G.; Furthmüller, J., *Phys. Rev. B* **1996,** 54 (16), 11169.

31. Blöchl, P. E., *Phys. Rev. B* **1994,** 50 (24), 17953.

32. Loschen, C.; Carrasco, J.; Neyman, K. M.; Illas, F., *Phys. Rev. B* **2007,** 75 (3), 035115.

33. Castleton, C. W. M.; Kullgren, J.; Hermansson, K., *J. Chem. Phys.* **2007,** 127 (24), 244704.

34. Makov, G.; Payne, M. C., *Phys. Rev. B* **1995,** 51 (7), 4014.

35. Necula, B. S.; Apachitei, I.; Fratila-Apachitei, L. E.; Teodosiu, C.; Duszczyk, J., *J. Colloid Interface Sci.* **2007,** 314 (2), 514.

36. Tabakova, T.; Boccuzzi, F.; Manzoli, M.; Sobczak, J. W.; Idakiev, V.; Andreeva, D., *Appl. Catal. A: Gen.* **2006,** 298, 127.

37. Wang, X.; Rodriguez, J. A.; Hanson, J. C.; Gamarra, D.; Martínez-Arias, A.; Fernández-García, M., *J. Phys. Chem. B* **2006,** 110 (1), 428.

38. Tuckerman, M. E.; Marx, D.; Parrinello, M., *Nature* **2002,** 417 (6892), 925.

39. Eigen, M., *Angew. Chem. Int. Ed. Engl.* **1964,** 3 (1), 1.

40. Zundel, G., The Hydrogen Bond, Recent Developments in Theory and Experiments. In Schuster, P.; Zundel, G.; Sandorfy, C., Eds. North-Holland: Amsterdam, 1976; Vol. II, p 683.

41. Loschen, C.; Bromley, S. T.; Neyman, K. M.; Illas, F., *J. Phys. Chem. C* **2007,** 111 (28), 10142.

42. Silvi, B.; Savin, A., *Nature* **1994,** 371 (6499), 683.

43. Zimmermann, R.; Dukhin, S.; Werner, C., *J. Phys. Chem. B* **2001,** 105 (36), 8544.

44. Lai, T.-Y.; Lee, W.-C., *J. Photochem. Photobiol. A: Chem.* **2009,** 204 (2-3), 148.

45. Patil, S.; Seal, S.; Guo, Y.; Schulte, A.; Norwood, J., *Appl. Phys. Lett.* **2006,** 88 (24), 243110.

46. Mamontov, E.; Egami, T.; Brezny, R.; Koranne, M.; Tyagi, S., *J. Phys. Chem. B* **2000,** 104 (47), 11110.

47. Babu, S.; Thanneeru, R.; Inerbaev, T.; Day, R.; Masunov, A. E.; Schulte, A.; Seal, S., *Nanotechnology* **2009,** 20 (8), 085713.

48. Sabia, R.; Stevens, H. J., *Mach. Sci. Technol.* **2000,** 4 (2), 235.

49. Janoš, P.; Petrák, M., *J. Mater. Sci.* **1991,** 26 (15), 4062.

50. Dana, L. Z., Polishing Parameters and Their Effect on Glass Polish Performance., *Ceram. Eng. Sci. Proc.*, John, B. W., Jr., Ed. 2008; Vol. 16, p 302.

51. Homma, Y.; Furusawa, T.; Morishima, H.; Sato, H., *Solid State Electron.* **1997,** 41 (7), 1005.

52. Cook, L. M., *J. Non-Cryst. Solids* **1990,** 120 (1-3), 152.

53. Rajan, K.; Singh, R.; Adler, J.; Mahajan, U.; Rabinovich, Y.; Moudgil, B. M., *Thin Solid Films* **1997,** 308-309, 529.

54. Parks, G. A., *Chem. Rev.* **1965,** 65 (2), 177.

55. Vyas, S. P.; Singh, A.; Sihorkar, V., *Crit. Rev. Ther. Drug Carr. Sys.* **2001,** 18 (1), 1.

56. Gao, X.; Cui, Y.; Levenson, R. M.; Chung, L. W. K.; Nie, S., *Nat. Biotech.* **2004,** 22 (8), 969.

57. Qian, Z. M.; Li, H.; Sun, H.; Ho, K., *Pharmacol. Rev.* **2002,** 54 (4), 561.

58. Low, P. S.; Antony, A. C., *Adv. Drug Del. Rev.* **2004,** 56 (8), 1055.

59. Boussif, O.; Lezoualc'h, F.; Zanta, M. A.; Mergny, M. D.; Scherman, D.; Demeneix, B.; Behr, J. P., *Proc. Natl. Acad. Sci. U.S.A.* **1995,** 92 (16), 7297.

60. Rosenholm, J. M.; Meinander, A.; Peuhu, E.; Niemi, R.; Eriksson, J. E.; Sahlgren, C.; Lindén, M., *ACS Nano* **2009,** 3 (1), 197.

61. Iinuma, H.; Maruyama, K.; Okinaga, K.; Sasaki, K.; Sekine, T.; Ishida, O.; Ogiwara, N.; Johkura, K.; Yonemura, Y., *Int. J. Cancer* **2002,** 99 (1), 130.

62. Ishida, O.; Maruyama, K.; Tanahashi, H.; Iwatsuru, M.; Sasaki, K.; Eriguchi, M.; Yanagie, H., *Pharm. Res.* **2001,** 18 (7), 1042.

63. Yang, P.-H.; Sun, X.; Chiu, J.-F.; Sun, H.; He, Q.-Y., *Bioconjugate Chem.* **2005,** 16 (3), 494.

64. Chithrani, B. D.; Chan, W. C. W., *Nano Lett.* **2007,** 7 (6), 1542.

3.6 Supporting Information

3.6.1 HRTEM Images of CNPs

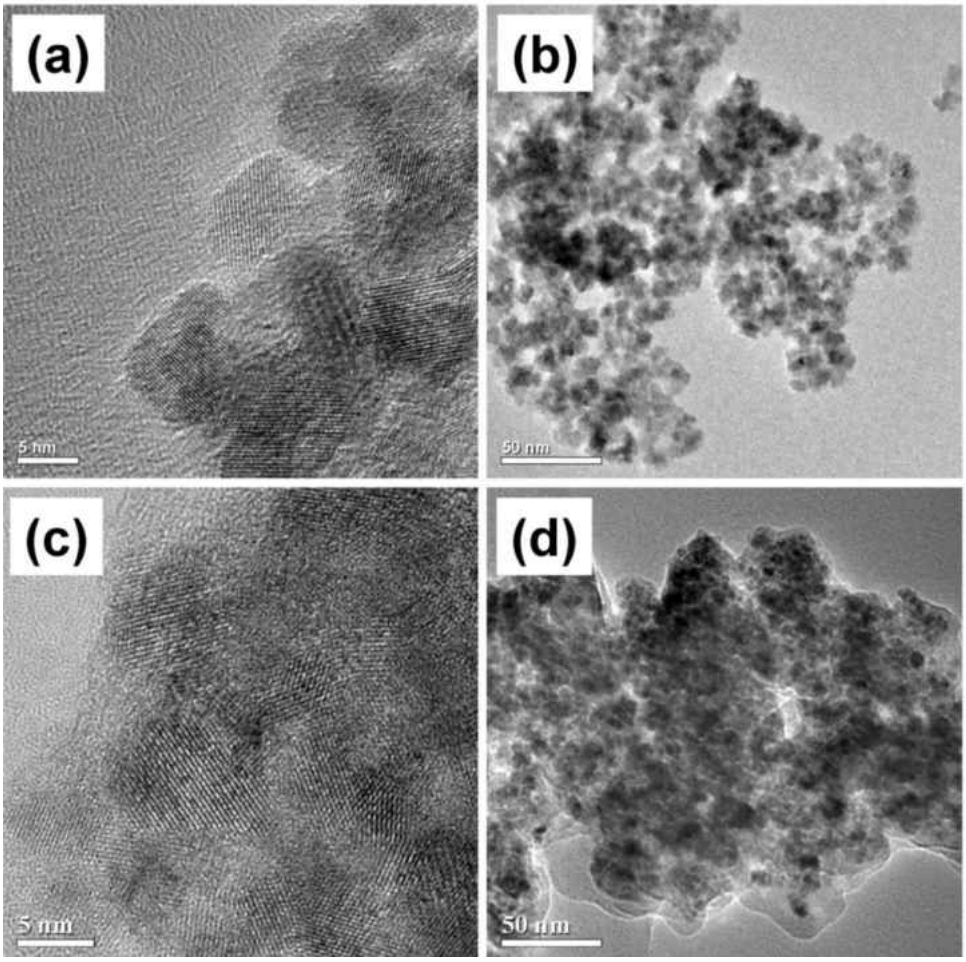

Figure 3.10: (a,b) HRTEM images of freshly prepared positively charged CNPs. (c,d) HRTEM images of aged negatively charged CNPs. It is clear that the CNP size remains the same in both the cases.

CHAPTER 4: SINGLE MOLECULE PROTEIN INTERACTIONS WITH PROTONATED NANOPARTICLES

4.1 Introduction

With more than ten million new cases every year, cancer has become one of the most dreadful diseases worldwide. Current cancer treatments include surgical intervention, radiation therapy, and chemotherapeutic drugs, which often kill healthy cells and cause severe side effects.[1] Site specific delivery of drugs and therapeutics can significantly reduce drug toxicity and increase the therapeutic effects.[2] Recent advances in nanomedicine research have shown the capability of using nanoparticles (NPs) to treat intractable diseases (viral, genetic, cancerous) as they are the only microscopic objects that can gain access to the cells and function as therapeutic agents.[3] NPs could be used as effective therapeutic agents for intracellular imaging, targeting, and in the delivery of drugs, genes and vaccines.[1, 4-6] Cellular targeting is often achieved by bioconjugation of polymeric (drug carriers), metallic, or oxide NPs with ligand proteins that can bind to the overexpressed receptors on the target cells.[1, 7] NP-protein conjugation is often influenced by the surface potential differences, and understanding their specific interactions leading to their cellular uptake is crucial for targeted drug delivery.[8]

CNPs have been shown to be biocompatible, nontoxic and have excellent antioxidant properties in the prevention of reactive oxygen species (ROS) mediated cell damage in animals.[9] CNPs have been found to prevent healthy cell damage during radiation therapy[10] and provide neuroprotection to spinal cord neurons[11] by acting as an antioxidant. Due to their smaller particle size, non-toxic nature and excellent biocompatibility, CNPs have the potential to be used as drug carrier and delivery agents.

Ligand-receptor mediated drug delivery and imaging systems have attracted primary focus in nanomedicine.[12, 13] Transferrin (Tf) is a cellular targeting ligand protein (Supporting Information Figure 4.6) used for transportation and supply of iron to growing cells in the body. The iron uptake process involves binding of iron carrying Tf to the Tf receptors (TfRs) expressed on the cells followed by their internalization via receptor mediated endocytosis.[14] With a motivation to develop a potential targeted drug delivery system, we have chosen CNPs as our model NP system and holo-Tf (Tf carrying two iron ions) as the cellular targeting agent.[15] Many studies have been carried out using Tf as a targeting ligand to deliver a wide range of therapeutic agents including nanoparticles into malignant sites that overexpress TfRs.[15-19] Since surface potential differences play a major role in NP-protein adhesion,[8] Tf could be attached to CNPs through electrostatic adsorption. During the transportation as well as cellular internalization process, changes in the local environmental pH could influence the surface charges and affect the NP-protein binding. Hence, a molecular level understanding of NP-protein binding is essential to develop effective cellular targets. No detailed studies have been reported so far on the molecular level interaction forces and adhesion behavior of Tf over nanoparticle surface.

Atomic force microscopy (AFM) based single molecule force spectroscopy (SMFS)[20-23] have proven to be the most versatile technique that induce molecular level interactions on surfaces using functionalized probes and monitor them in real time at sub-nanometer resolution. Here we have used SMFS technique to probe the interaction forces between Tf and CNPs with varying zeta potentials (ZPs), and an extensive study on the

importance of Tf adhesion on nanoparticle surface for preferential cellular uptake is presented. Density functional theory (DFT) along with DFT+U technique is used to calculate the binding energy between the protein and the NP responsible for preferential cellular uptake. Both high resolution transmission electron microscopy (HRTEM) and inductively coupled plasma mass spectrometry (ICP-MS) measurements were performed on human lung adenocarcinoma epithelial cells and human embryo lung fibroblast cells to analyze and quantify the cellular internalization of transferrin conjugated CNPs (Tf:CNPs) and bare CNPs.

4.2 Results and Discussion

4.2.1 Cerium Oxide Nanoparticles

HRTEM image of base precipitated CNPs (mean size of 8.2 ± 1 nm) and AFM image of the same CNPs coated on a silicon substrate are shown in Figure 4.1a, and b, respectively. X-ray diffraction (XRD) pattern of CNPs shows a fluorite structure with dominant (111) planes (Figure 2.1c). CNPs in water showed a positive ZP of +39.6±0.631 mV in the synthesized condition, while Tf dissolved in deionized water exhibited a negative ZP of -19.9 ± 0.9 mV. In order to study the electrostatic interaction of CNPs with negatively charged Tf, CNPs with different surface charges were prepared by treating them with acidic and basic pH buffers.[8] CNPs treated with pH buffers 5, 8 and 14 showing a ZP values of +36.4±0.7, +5.9±1.2, and -35.1±0.9 mV, respectively, were used for SMFS studies (Figure 2.1d).

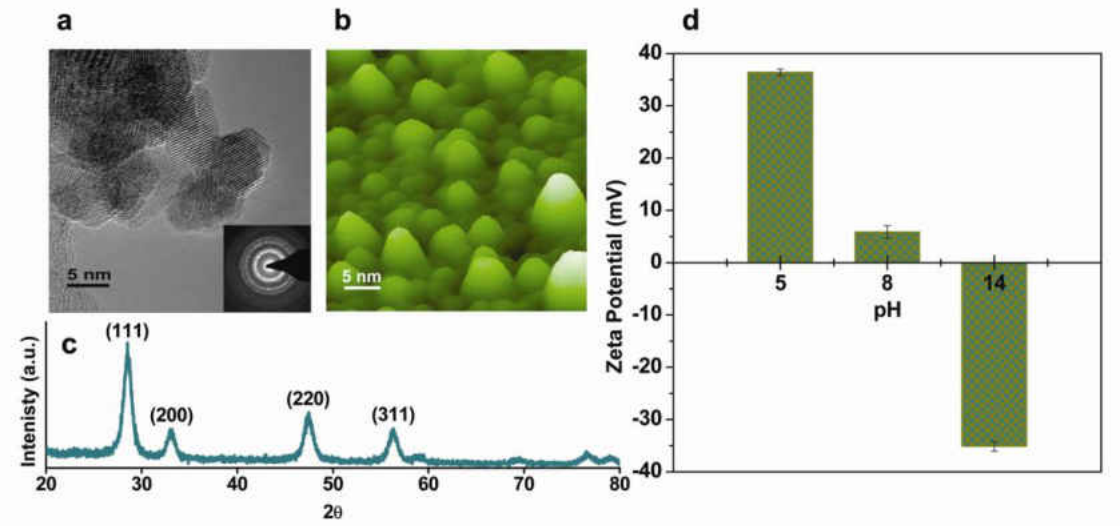

Figure 4.1: Particle size, crystal structure and surface potentials of CNPs. (a) HRTEM (b) AFM image and (c) XRD spectrum of fluorite structured CNPs; (d) ZP plot of CNPs treated with different pH buffers. AFM and HRTEM images show that the CNP particle size is between 7-10 nm. XRD pattern and HRTEM images shows the presence of dominant (1 1 1) planes of cerium oxide fluorite structure. Positively charged CNPs were obtained by acidic buffer treatment (more H^+ ions on surface) while basic buffer treatment (more OH^- ions on surface) resulted in negatively charged CNPs. The isoelectric point (pl) is observed at 8.5. Each sample was analyzed 30 times (n=30) and the average values of ZP with standard deviation (mean±sd) are plotted here.

4.2.2 Single Molecule Interaction of Transferrin with Cerium Oxide Nanoparticles

SMFS measurements were carried out using a Tf conjugated AFM tip (Figure 4.2a-c) on CNPs (with zeta potentials of +36.4±0.7, +5.9±1.2, and -35.1±0.9 mV) coated on silicon substrate. To understand the interaction mode and conformational changes of Tf, SMFS measurements were also conducted on an atomically smooth silicon substrate in aqueous medium (Supporting Information Figure 4.7). Figure 4.2d-f shows the force-extension profile of Tf coated AFM tip interaction with CNPs of varying surface potentials. The corresponding unbinding force and unbinding length histograms of rupture events are also shown in Figure 4.2g-l. These results indicate that the adhesion between Tf and

CNPs decreases on tuning CNP surface charges from positive to negative ZP values, with a maximum for +36.4±0.7 mV ZP. The force spectrum corresponding to CNPs of +36.4±0.7 mV ZP (Figure 4.2d), shows multiple interaction events due to the unbinding of proteins from the CNP sample at three different sites (strong interaction between Tf and CNPs could result in the adhesion of multiple proteins from the AFM tip at different sites on the sample). The highest unbinding force is observed at the first dip where the magnitude of pull-off force is ~2.835 nN. As the ZP is directly related to the particle surface potential, a strong attraction is observed between the Tf and positive CNPs due to their high surface charge difference. To confirm that the observed changes in the force signals were indeed originated from the single molecule rupture events, the force extension profiles were fitted using entropic elasticity models, which predict the relationship between the applied force and the stretching of a polymer molecule.[24] The elastic properties of these stretching events can be described by the worm-like chain (WLC) model.[23, 25] According to this model, the force needed to stretch a linear polymer molecule in a medium to a length x is given by

$$F(x) = \left(\frac{k_b T}{b}\right)\left[\frac{1}{4}\left(1-\frac{x}{L}\right)^{-2} - \frac{1}{4} - \frac{x}{L}\right] \tag{4.1}$$

where K_b is the Boltzmann constant, T is the absolute temperature of the medium, b is the persistence length (length of a stiff segment of the protein chain), L is the contour length (length of the completely stretched chain) and x is the distance between the attachment points of the protein (extension or end-to-end distance between the tip and sample). The stiffest element in a peptide chain is the single amino acid unit and it has a length of

~0.38 nm which corresponds to the persistence length *b* in the WLC model.[26] WLC fit yielded values of *b* = (0.024±0.003) nm and *L* = (423.2±5.7) nm for the first interaction event (Figure 4.2d). Such a low persistence length (~0.024nm) is unphysical (one order less than the values typically quoted for pulling of single proteins[25]) and the contour length is also higher than the maximum possible length (~257 nm) of a fully extended single Tf. This could be due to the simultaneous unfolding of multiple interacting proteins attached to the tip[27] (since the Tf backbone is folded into multiple helical groups, pulling Tf itself involves stretching of many interacting protein chains). The second and third unbinding force dips correspond to a magnitude of ~748 pN and ~499 pN, respectively. These additional dips in the force-extension spectrum reveal multiple protein interactions with the NP surface. For these interactions, we used a persistence length value of 0.5 nm and the WLC model yielded a counter length value of 203.1±3.1 nm and 83.5±6.7 nm for the second and third dip, respectively. These contour lengths were smaller than an estimated fully extended length of Tf (polypeptide chain of 678 amino acids corresponds to ~257 nm in length). Hence the second dip could be as a result of single molecule stretching of peptide chain involving unfolding of both the domains (N-lobe and C-lobe) and the third dip could be likely due to the unfolding of part of another peptide chain (most likely just one of the two domains of the protein is involved in stretching). This kind of multiple protein-stretching event happens due to the strong interaction of Tf with high positive CNPs and most of the SMFS measurements carried out on these samples showed similar multiple stretching events. According to the unbinding force histogram analysis shown in Figure 4.2g, the majority of rupture force

events observed are between 150 to 225 pN with a maximum force at ~9.0 nN. Even though they had a wide spectrum of force range, events with a force of magnitude higher than 1.5 nN were mostly non-repeating single events. Similarly majority of protein unbinding lengths fall between 25 to 50 nm (Figure 4.2h). Figure 4.2e shows the Tf interaction spectrum with CNPs having moderate ZP (+5.9±1.2 mV). The force-extension spectrum shows two successive single molecule interaction events and the corresponding unbinding forces are ~318 pN and ~596 pN, respectively. WLC fit with a persistence length of 0.5 nm yielded contour lengths of 215.4±2.5 nm and 130.9±2.0 nm. The lower unbinding force observed is due to the weak interaction between Tf and CNPs with lower positive surface potentials. Unbinding force histogram analysis shows that the maximum number of rupture force events is observed between 75 to 150 pN with a maximum force at ~1.1 nN (Figure 4.2i), and the maximum number of protein unbinding lengths falls between 0 to 25 nm (Figure 4.2j). Similarly, Figure 4.2f shows the force spectrum of Tf interacting with high negative ZP (-35.1±0.9 mV) CNPs, and the unbinding force observed is ~349 pN. WLC fit with persistence length of 0.5 nm yielded a contour length of 251.2±3.7 nm. Repeated SMFS measurements on these samples yielded a force of interaction much lower than 349 pN and within the range of 0 to 125 pN (mostly a flat force spectrum at 0 nN was obtained due to the absence of interaction events). Unbinding force histogram analysis showed almost negligible interaction force events with a maximum unbinding force at ~900 pN (Figure 4.2k). Here above 50 pN, most of the events were non-repeating single events and the unbinding length histogram exhibited a peak close to zero nm due to higher number of negligible interaction events (Figure 4.2l).

The lower unbinding force and length observed is due to the strong repulsion between Tf and negatively charged CNPs. Characteristic domain unfolding of Tf was observed in some of the force extension profiles (Supporting Information Figure 4.8) and were very similar to the domain unfolding usually seen in SMFS of other proteins.[25] SMFS studies conducted on NP samples revealed a strong binding affinity of Tf to protonated CNP surface. To understand the nature and type of Tf bonding over CNP surface, theoretical simulation studies have been carried out.

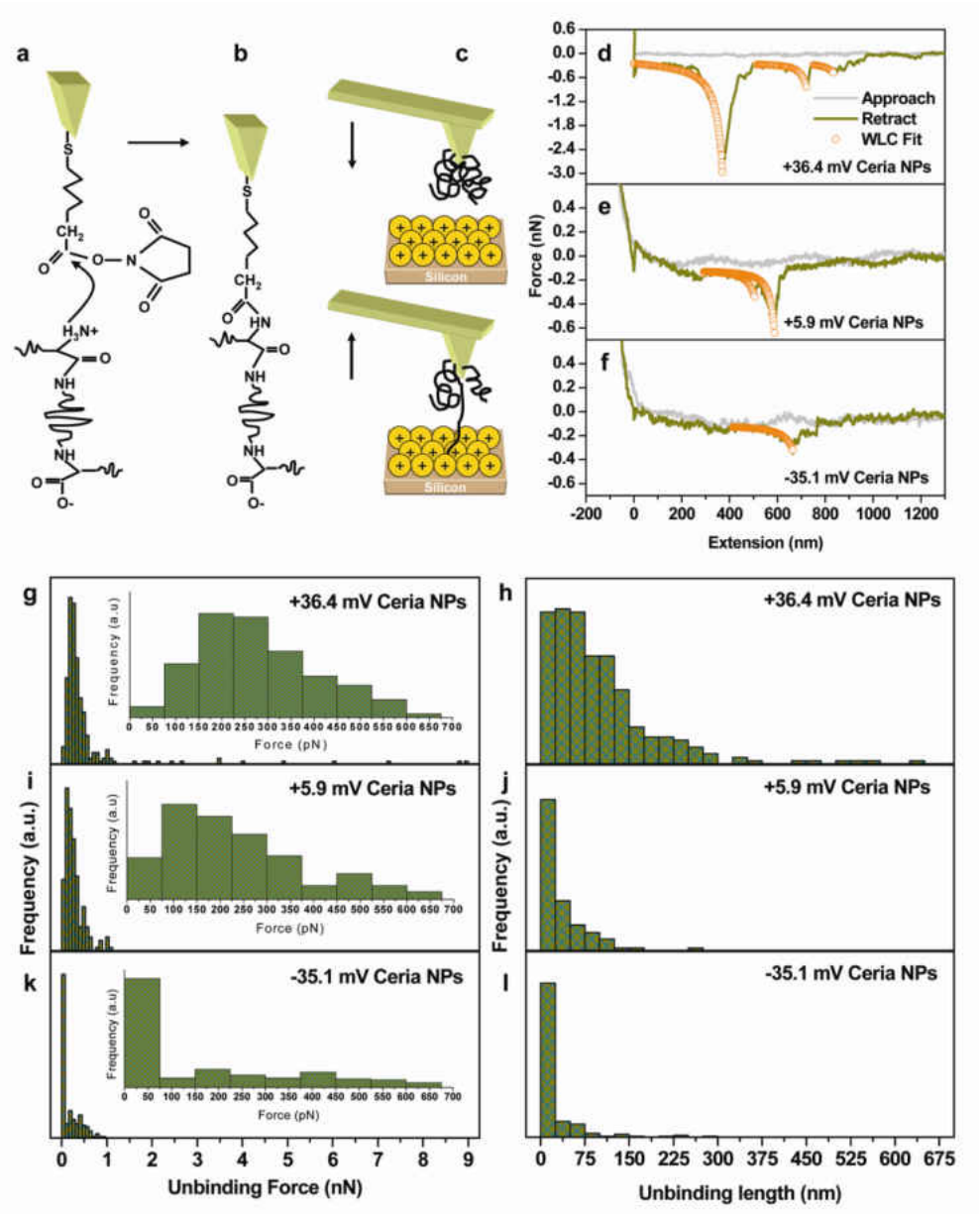

Figure 4.2: Schematic diagram of AFM probe functionalized with Tf interacting with positively charged CNPs, the force-extension spectrum and the force, length histograms obtained on CNPs with different ZPs. For protein-CNP interaction studies, (a) succinimide functionalized AFM tip was bioconjugated with Tf to form (b) Tf terminated AFM probe. (c) Interaction of Tf terminated AFM tip with protonated CNPs. Force-extension plots of Tf interacting with CNPs of ZP (d) +36.4±0.7 mV; (e) +5.9±1.2 mV; and (f) -35.1±0.9 mV. The corresponding force (g, i, and k) and length histograms (h, j, and l) are also shown. Force and length histograms were obtained by conducting multiple SMFS measurements on each sample. The total number of force and length values analyzed were n=273 (g and h), 206 (i and j) and 210 (k and l).

4.2.3 DFT Simulation of Protein Interaction with Protonated Cerium Oxide Nanoparticles

Under physiological pH conditions, Tf exhibits higher number of negatively charged sites on its surface. These sites contain carboxylate ions in the form of aspartate (Asp) and glutamate (Glu) amino acid residues [28] that can interact with protonated CNPs to form hydrogen bonds with the NP surface. Both these residues are terminated with carboxyl ions at each end. DFT simulation studies were conducted to understand the nature of bonding between the carboxyl ion of the protein and the protonated CNPs. For simplicity, we modeled the NP-protein interaction by considering one glycinate ion (the simplest amino acid structure with one carboxyl ion) interacting with one CNP. Figure 4.3a shows the atomic structural model of protonated CNP interacting with the carboxyl ion of the glycinate. This octahedral CNP was derived from a bulk fluorite lattice that exposes the most stable (111) facets. To simulate the surface properties of CNPs with respect to their surface charge conditions, different levels of protonation varying from one to three H^+ ions on the surface of CNP were considered. This is achieved by terminating up to three neighboring oxygen atoms on the same NP facet with one H^+ ion each. Relaxed configuration of triple protonated CNP interacting with the carboxyl ion of the glycinate is shown in Figure 4.3a. All of the H^+ ions interacted strongly with the NP and formed strong hydrogen bonds (more covalent in nature) with its surface oxygen atoms. The length of the O-H bond obtained here is 0.991 Å. The projection of electron localization function (ELF)[29] on different planes (Figure 4.3b,c) passing through oxygen atoms of the protonated CNP and the glycinate ion reveals the formation of weak hydrogen bonds

(more ionic in nature) between one of the carboxyl oxygen atoms and multiple protons on the CNP surface (Figure 4.3b). Here, the equilibrium O-H distance obtained is 1.87 Å. Meanwhile, the second oxygen atom of the carboxyl ion, which is in an equilibrium position with respect to one of the NP surface protons, formed a strong hydrogen bond with that proton (Figure 4.3c). This hydrogen bonding forms the basis for strong interaction of proteins with CNPs. Here, the equilibrium O-H distance obtained is 1.36 Å. Figure 4.3d shows the energy profiles of protonated CNP interacting with the carboxyl ion of the glycinate as a function of the number of protons on the NP surface. The blue curve represents the total ground state energies of CNPs interacting with the carboxyl ion of the glycinate, while the red curve represents the sum of their individual energies when they are separated by infinite distance (no interaction with each other). Both the curves show a decrease in the ground state energies with the addition of protons on CNP surfaces. However, the ground state energies of the carboxyl ion of the glycinate interacting with doubly and triply protonated CNP are not much different. This is due to the bending of bonds as a result of relaxation of weak hydrogen bond forming oxygen atoms to their equilibrium positions (total energy increases as the bond angles are bent from their normal configuration). The decrease in ground state energies with increase in numbers of protons on NP surfaces showed that the triply protonated CNP's surface is at a more favorable energy state for carboxyl ion interaction than the singly protonated CNP's surface. The total energies of CNP glycinate complex at binding configuration and at a large separation are represented by the red and the blue curves in Figure 4.3d. The difference of these total energies amounts to the binding energy between the protonated

CNP and the carboxyl ion of the glycinate and is represented by cyan curve as shown in Figure 4.3d. The binding energy values displayed a tendency to increase with an increase in the number of protons on the NP surface. The binding energies between the carboxyl ion of a glycinate and a CNP covered by 1 to 3 protons are 2.81 eV, 4.03 eV and 4.19 eV, respectively. Hence, it is clear that adding more protons to the CNP surface could enhance the NP-protein binding. Both SMFS and DFT simulation studies conducted on CNPs revealed that Tf forms strong hydrogen bonds with a protonated CNP surface. The ligand-receptor mediated internalization of CNPs depends on the stability of Tf adhesion on CNP surface in a physiological environment. To test the stability of Tf coating over protonated CNP surface and its cellular uptake efficiency, Tf:CNPs were incubated with human lung adenocarcinoma epithelial cells (A549) and human embryo lung fibroblast cells (WI-38).

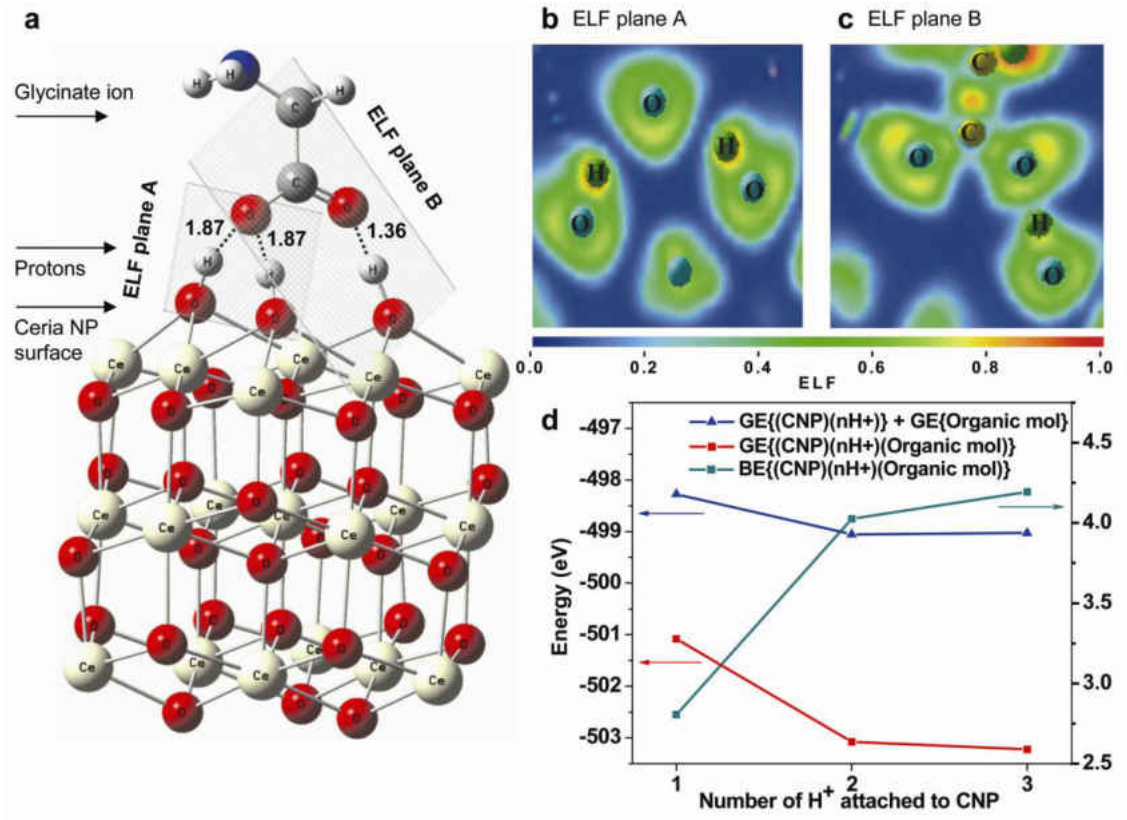

Figure 4.3: Atomic structural model and energy profile of carboxyl ion of a glycinate interacting with a CNP. (a) Side view of the relaxed configuration of a negatively charged glycinate ion on a triply protonated facet of CNP. (b, c) Representation of the projection of electron localization function (ELF) on different planes passing through oxygen atoms of a protonated CNP and a glycinate ion, revealing the formation of weak and strong hydrogen bonds between them. (d) Representation of ground state energy profile. Blue curve represents the ground state energy levels of a protonated CNP interacting with the carboxyl ion of a glycinate and the red curve represents the sum of the ground state energies of a protonated CNP and a glycinate ion located at infinite distance. The binding energy (cyan curve) between the protonated CNP and carboxyl ion of the glycinate was evaluated as the difference between the red and blue energy curves. ELF plots also reveal that all the protons formed strong hydrogen bonds with oxygen atoms of cerium oxide. Color code blue (ELF=0) and red (ELF=1.0) represents full absence and full presence of electron pair in actual point of space.

4.2.4 Transferrin Adsorption and Cellular Uptake of Cerium Oxide Nanoparticles

CNPs with a high positive ZP of +39.6±0.631 mV were used for protein adsorption and cellular uptake studies. Due to a strong electrostatic attraction, Tf was strongly bonded to

CNPs (the higher the surface charges of NPs, the higher the protein adsorption). The ZP obtained on CNPs after Tf coating was +24.0±2.1 mV (ZP differences between CNPs and Tf:CNPs indicate the presence of Tf on CNPs). The protein adsorption on CNPs was confirmed by conducting FT-IR (Supporting Information Figure 4.9) and XPS (Supporting Information Figure 4.10) analyses on Tf:CNPs. The amount of Tf adsorption on CNPs was quantified by conducting UV absorbance spectroscopy measurements at 280 nm wavelength (Supporting Information Figure 4.11) on Tf:CNP solutions. Tf:CNPs showed a protein adsorption of approximately 500 mg/g of CNPs.

Cellular uptake of NPs involves a two-step process. The first step is the binding of NPs to the cell membrane and the second is cellular internalization.[30] After the adsorption of the NPs on the cell membrane, the uptake occurs via several possible mechanisms: pinocytosis, receptor-mediated endocytosis, or phagocytosis.[31] Since cancer cells have a higher growth rate, they over-express TfRs on their surface and will absorb iron at a higher rate. Hence, NPs linked with Tf would be taken up efficiently. To understand the mechanism of CNP uptake in cancer and healthy cells, we have chosen A549 and WI-38 cells, respectively, as model cell systems. The cells were incubated with varying concentrations (from 100 nM to 100 μM) of Tf:CNPs and bare CNPs. Figures 4a, b show the percent of CNP cellular uptake by A549 and WI-38 cells obtained from ICP-MS measurements (ICP-MS measurements were made after diluting the NPs incubated cell samples to ppb level concentrations and the % uptake are reported with respect to the molar concentrations at which the cells were incubated). A549 cells incubated with 100 nM concentration of CNPs, exhibited an enhanced uptake (~9.7 ng/mL) of Tf:CNPs

compared to bare CNPs (~5.2 ng/mL). However, at 1 μM concentration, A549 cells exhibited a reduced uptake (~51.8 ng/mL) of Tf:CNPs than that of bare CNPs (~61.1 ng/mL). Both 10 μM and 100 μM CNP incubated cells showed a higher uptake (~0.9 μg/mL and ~11.3 μg/mL, respectively) of Tf:CNPs and a lower uptake (~0.7 μg/mL and ~6.8 μg/mL, respectively) of bare CNPs similar to cells incubated with 100 nM concentrations of CNPs. Among all the concentrations, A549 cells incubated with concentrations of 100 nM, 10 μM, and 100 μM exhibited preferential uptake of Tf:CNPs compared to bare CNPs (Figure 4.4a). An enhanced uptake of Tf:CNPs by A549 cells indicates that the uptake in cancer cells is most likely by receptor-mediated endocytosis.[32] Figure 4.4c shows the proposed model of TfR mediated endocytosis of CNPs by A549 cancer cells. The first step is the binding of holo-Tf carrying CNPs to the TfRs on the cell membrane (SMFS studies reported earlier have shown an unbinding force of ~56 pN and an unbinding length of ~44 nm between holo-Tf coated tip and and TfR functionalized mica substrate at pH 7.4[33]). The complex is then taken up inside the cell and transferred to the endosomal compartment where it is acidified (pH changes from ~7.4 to ~5.5). At a pH close to 5.4 (pl of Tf), Tf becomes neutrally charged and triggers the release of CNPs and iron as there is no more interaction with Tf. Recent studies have shown that Tf conjugated quantum dots (Tf:Qdots), after internalization through receptor mediated endocytosis remained in the endocytic structures and were not efficiently exocytosed.[32] This could be due to the strong interaction of Tf with the quantum dots. Similar to Tf:Qdots, Tf:CNPs can also get trapped inside the endocytic structures. To understand the exocytosis mechanism of Tf:CNPs, a detailed investigation has to be carried out. Due to

their high growth rate, cancer cells need more iron and thus will eventually internalize more iron carrying Tf:CNPs. The highest percent uptake (~66%, corresponds to ~11.3 μg/mL) of Tf:CNPs was seen in cells incubated with 100 μM concentration of CNPs (Figure 4.4a). A549 cells incubated with a concentration of 100nM exhibited the highest difference in uptake (~87%, from ~5.2 ng/mL to ~9.7 ng/mL) upon coating with Tf. Figure 4.4d shows the TEM images of A549 cells incubated with a concentration of 100 nM of Tf:CNPs. The core-shell like particles seen in TEM images, indicate the presence of a thin layer of Tf coating on CNPs. Large core size (~500nm) indicates the formation of NP agglomerates during the uptake process. Although the percentage of uptake was lower compared to Tf:CNPs, A549 cells showed considerable uptake of bare CNPs (Figure 4.4a). In the case of bare CNPs, the initial binding process can be visualized as a strong attraction between the positively charged CNPs and the negatively charged cell, facilitating their adsorption on the cell membrane and subsequent internalization via a nonspecific phagocytosis or pinocytosis processes.[8] The relatively lower uptake of bare CNPs by A549 cells is also evident from the lack of particles seen in the TEM images of cells incubated with a concentration of 100nM of bare CNPs (Supporting Information Figure 4.12a).

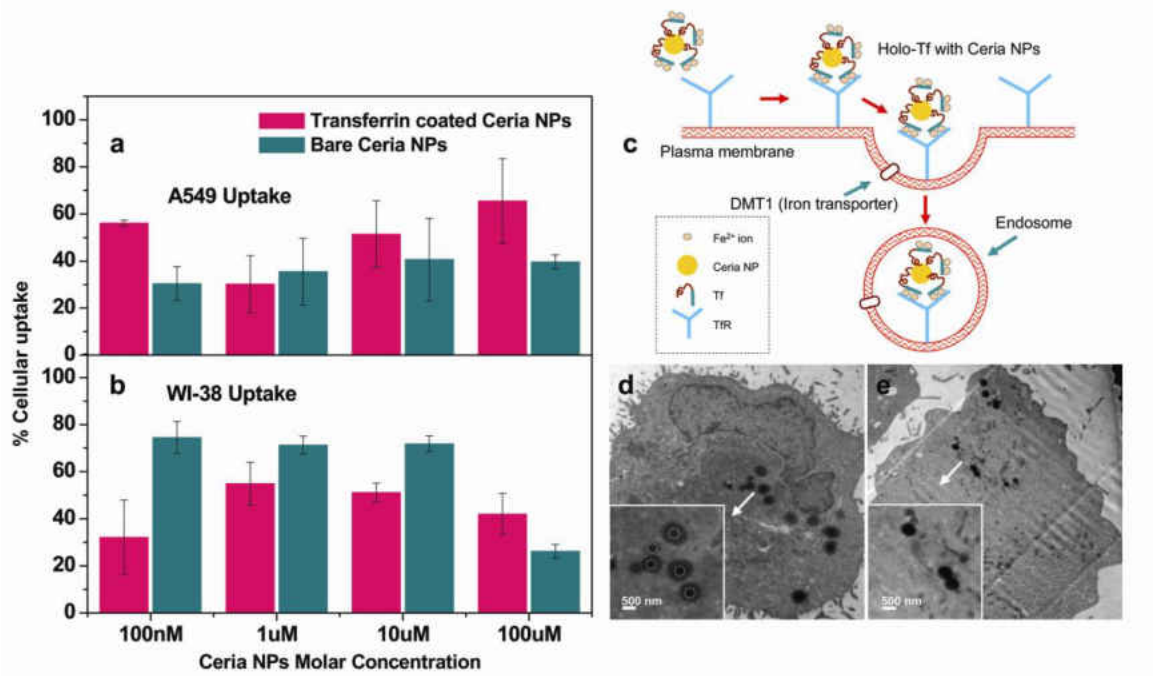

Figure 4.4: Cellular uptake of CNPs. (a, b) Cellular uptake of the CNPs by A549 cancer cells and WI-38 healthy cells at different concentrations of CNPs. (c) The cycle of TfR mediated cellular uptake of Tf:CNPs. (d, e) TEM images of A549 cancer cells incubated with Tf:CNPs and WI-38 healthy cells incubated with bare CNPs. (a) A549 Cells treated with 100 nM, 10 µM and 100 µM concentrations showed preferential cellular uptake of Tf:CNPs while (b) WI-38 cells treated with 100 nM, 1 µM, and 10 µM concentrations exhibit an increased uptake of bare CNPs. The bar chart is obtained by conducting ICP-MS analysis on 24 sets of A549 and WI-38 cells. The data is expressed as mean±sd. (c) Holo-Tf carrying CNP binds to TfR molecules expressed on the cell surface. After endocytosis via clathrin coated pits formed on the plasma membrane, the complex is taken up inside the plasma membrane by forming an endocytic vesicle. (d) The core shell like particles seen in A549 cells indicates the presence of Tf:CNPs (e) Solid spherical particles seen in WI-38 indicate the presence of bare CNPs. Agglomerated CNPs of size ~500 nm is observed in both the cases. Inset shows the magnified view of particles. White doted circles show the position of the CNPs inside the core shell structure.

WI-38 cells incubated with three different concentrations of bare CNPs under similar conditions exhibited enhanced uptake compared to Tf:CNPs (Figure 4.4b). Here the mechanism of uptake is similar to that seen in the case of bare CNPs in A549 cells. Figure 4.4e shows TEM images of WI-38 cells incubated with a concentration of 100 nM of bare CNPs. The solid spherical particles seen in TEM images indicate the presence of

CNP agglomerates. It is clear from the ICP-MS data (Figure 4.4b) that the Tf:CNPs had a reduced uptake in these cells. At 100 nM, 1 μM and 10 μM concentrations, WI-38 cells exhibited a lower uptake (~5.5 ng/mL, ~94.4 ng/mL and ~0.9μg/mL, respectively) of Tf:CNPs compared to bare CNPs (~12.8 ng/mL, ~122.7 ng/mL and ~1.2 μg/mL, respectively). However, 100 μM CNP treated cells showed a higher uptake (~7.2 μg/mL) of Tf:CNPs that that of bare CNPs (~4.5 μg/mL). The TEM images of WI-38 cells incubated with 100 nM of Tf:CNPs also displayed less numbers of particles inside the cells and most of them were trapped near the cell wall (Supporting Information Figure 4.12b). This indicates that Tf:CNPs interact with the WI-38 cell membrane to a lesser extent as compared to bare CNPs. Besides reducing the CNPs effective surface potentials (from +39.6±0.631 mV to +24±2.1 mV), Tf coating can also induce steric hindrance between Tf and the negatively charged domains present on the cell membrane.[30, 34] This could be the reason for the reduced cellular uptake of Tf:CNPs. WI-38 cells incubated with 100 nM of bare CNPs (Figure 4.4b) showed the highest percent of uptake (~75%, corresponds to ~12.8 ng/mL) and the uptake was reduced by ~57% (from ~12.8 ng/mL to ~5.5 ng/mL) upon coating with Tf. 100 μM treated WI-38 cells exhibited reduced uptake of bare CNPs as compared Tf:CNPs. At higher concentrations CNPs have a tendency to agglomerate,[35] which could be the reason for the reduced uptake of bare CNPs seen at 100μM concentration (in the case of Tf:CNPs, larger agglomeration may not take place due to the steric hindrance between the Tf coated particles). The cellular uptake studies conducted on both A549 and WI-38 cells of Tf:CNPs and bare CNPs have shown that the

interaction mechanism of nanoparticles with cells can be tuned by changing the NP surface conditions.

Tuning the surface charges of NPs (for enhanced ligand coverage) is a key requirement to achieve efficient cellular targeting and preferential drug delivery to malignant sites in the body. The interaction forces acting between NPs and biological systems (proteins and cells) at different stages starting from ligand conjugation to cellular uptake plays a major role in the transportation and delivery of drugs. Figure 4.5 shows a schematic diagram of interaction forces acting at various stages of the Tf:CNP cellular uptake process. The specific interaction between a Tf (on NP surface) and a TfR (at cell surface) is fixed (unbinding force of ~56 pN and unbinding length of ~44 nm) and cannot be tuned. However, through protonation, the interaction between Tf and CNPs can be enhanced (unbinding force of ~150 to 225 pN and unbinding length of ~25 to 50 nm for +36.4±0.7 mV ZP CNPs) to a greater extent. Since Tf loading on a NP surface depends mainly on the surface charge difference (electrostatic adhesion), it is possible to add more numbers of Tf to a highly positive CNP surface. A higher positive charge and more numbers of Tf on the CNP surface will lead to better cell adhesion through a large number of ligand receptor mediated interactions (tunable multi-point interaction events, Figure 4.5). Hence, tuning the NP surface with more protons can not only improve the adhesion of ligands with the NP surface, but it can also enhance the adhesion of a ligand conjugated NP with the cell surface thereby enhancing the receptor mediated cellular uptake. Similarly, the non-specific interaction can also be tuned by tuning the CNPs surface potentials.

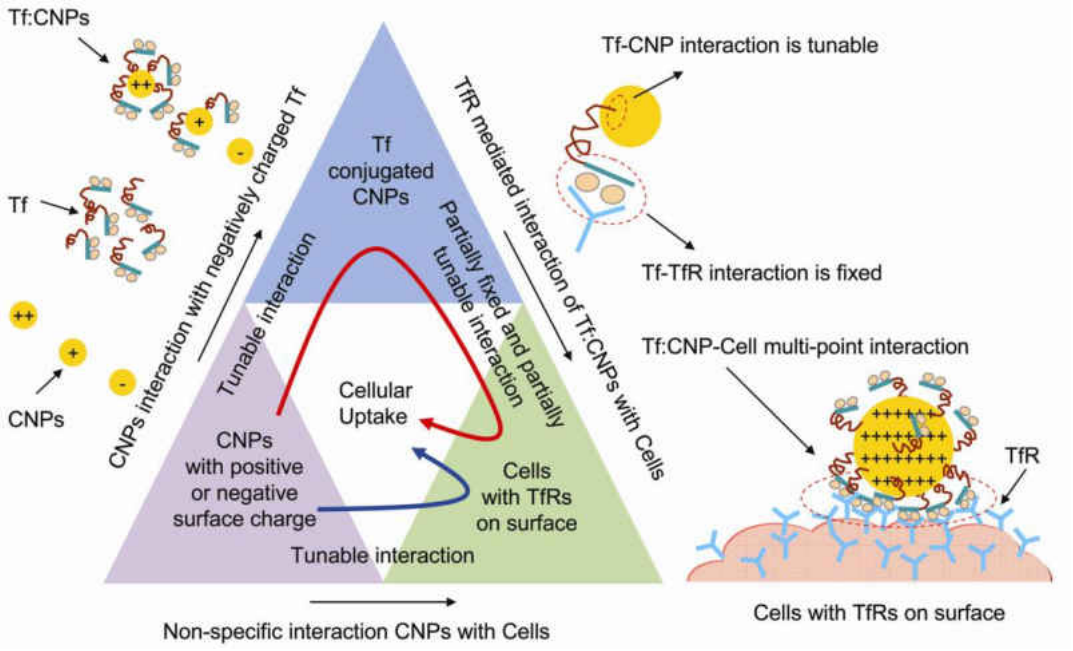

Figure 4.5: Schematic diagram of interaction forces acting at different stages of cellular uptake. The triangle blocks show the interaction pathways of cellular uptake of CNPs. CNPs with strong positive charge show better adsorption of Tf. The interaction between Tf and CNPs can be tuned by protonation; however, the interaction of Tf with TfR is fixed. CNPs with a strong positive charge lead to enhanced Tf adsorption and multiple interactions with the TfRs on the cell surface. Red curved arrow inside the triangle blocks indicates the receptor mediated cellular internalization pathway of positively charged CNPs and blue curved arrow indicates the non-specific cellular internalization pathway of both positively and negatively charged CNPs. The red dashed circle represents the domain of multi-point interaction between Tf:CNP and TfRs on cell surface.

4.3 Conclusion

The experiments presented here not only show that the Tf can be effectively attached to the NP surface but also can be used as a targeting ligand in receptor mediated internalization of metal oxide NPs. Acidic buffer treatment of CNPs results in highly protonated surface and forms stable coating of Tf over CNPs. According to DFT simulation studies, the bonding between Tf and CNPs is mostly determined by the nature of hydrogen bonds forming between the NP surface protons and the carboxylate ions of the protein, and the binding energy between Tf and CNP increases with the number of

surface protons present on the NPs. ICP-MS and TEM analysis conducted on both healthy and cancer cells incubated with CNPs shows that Tf:CNPs can be preferentially internalized by cancer cells. These results revealed the efficiency and physiological stability of Tf:CNP in receptor mediated cellular internalization process. They also demonstrate that the preferential cellular uptake of NPs can be achieved by binding with targeting ligands and it is essential to tune the surface charges of nanoparticles to achieve a better NP-ligand binding. Physiochemical modifications of nanoscale surfaces play a vital role in designing nanosize drug carriers, which can preferentially target and deliver therapeutic drugs to malignant cells.

4.4 Materials and Methods

CNPs were synthesized by precipitation technique from cerium nitrate precursors.[36] The particles were treated with acidic or basic pH buffers to induce different surface charges (see Supporting Information for more details).

Succinimide functionalized gold coated silicon nitride cantilevers (purchased from Novascan technologies) were treated with Tf solution to obtain Tf conjugated AFM probes. SMFM experiments were conducted on CNPs coated silicon surface placed in a liquid cell filled with deionized water. The forces of interaction between Tf and CNPs were measured by lowering the tip close to the NP surface and retracting it until the NP-protein bond broke (see Supporting Information for more details).

4.5 References

1. Peer, D.; Karp, J. M.; Hong, S.; Farokhzad, O. C.; Margalit, R.; Langer, R., *Nat. Nano* **2007,** 2, (12), 751-760.

2. Anabousi, S.; Laue, M.; Lehr, C.-M.; Bakowsky, U.; Ehrhardt, C., *Eur. J. Pharm. Biopharm.* **2005,** 60, (2), 295-303.

3. Lynch, I.; Cedervall, T.; Lundqvist, M.; Cabaleiro-Lago, C.; Linse, S.; Dawson, K. A., *Adv. Colloid. Interface Sci.* **2007,** 134-135, 167-174.

4. Sun, C.; Lee, J. S. H.; Zhang, M., *Adv. Drug. Del. Rev.* **2008,** 60, (11), 1252-1265.

5. Cui, Z.; Mumper, R. J., *Crit. Rev. Ther. Drug Carr. Sys.* **2003,** 20, (2-3), 103-137.

6. Panyam, J.; Labhasetwar, V., *Adv. Drug Del. Rev.* **2003,** 55, (3), 329-347.

7. Roy, I.; Ohulchanskyy, T. Y.; Pudavar, H. E.; Bergey, E. J.; Oseroff, A. R.; Morgan, J.; Dougherty, T. J.; Prasad, P. N., *J. Am. Chem. Soc.* **2003,** 125, (26), 7860-7865.

8. Patil, S.; Sandberg, A.; Heckert, E.; Self, W.; Seal, S., *Biomaterials* **2007,** 28, (31), 4600-4607.

9. Chen, J.; Patil, S.; Seal, S.; McGinnis, J. F., *Nat. Nano* **2006,** 1, (2), 142-150.

10. Tarnuzzer, R. W.; Colon, J.; Patil, S.; Seal, S., *Nano Lett.* **2005,** 5, (12), 2573-2577.

11. Das, M.; Patil, S.; Bhargava, N.; Kang, J. F.; Riedel, L. M.; Seal, S.; Hickman, J. J., *Biomaterials* **2007,** 28, (10), 1918-1925.

12. Vyas, S. P.; Singh, A.; Sihorkar, V., *Crit. Rev. Ther. Drug Carr. Sys.* **2001,** 18, (1), 1-76.

13. Gao, X.; Cui, Y.; Levenson, R. M.; Chung, L. W. K.; Nie, S., *Nat. Biotech.* **2004,** 22, (8), 969-976.

14. Gomme, P. T.; McCann, K. B.; Bertolini, J., *Drug Discov. Today* **2005,** 10, (4), 267-273.

15. Qian, Z. M.; Li, H.; Sun, H.; Ho, K., *Pharmacol. Rev.* **2002,** 54, (4), 561-587.

16. Iinuma, H.; Maruyama, K.; Okinaga, K.; Sasaki, K.; Sekine, T.; Ishida, O.; Ogiwara, N.; Johkura, K.; Yonemura, Y., *Int. J. Cancer* **2002,** 99, (1), 130-137.

17. Ishida, O.; Maruyama, K.; Tanahashi, H.; Iwatsuru, M.; Sasaki, K.; Eriguchi, M.; Yanagie, H., *Pharm. Res.* **2001,** 18, (7), 1042-1048.

18. Yang, P. H.; Sun, X.; Chiu, J. F.; Sun, H.; He, Q. Y., *Bioconjugate Chem.* **2005,** 16, (3), 494-496.

19. Chithrani, B. D.; Chan, W. C. W., *Nano Lett.* **2007,** 7, (6), 1542-1550.

20. Oesterhelt, F.; Oesterhelt, D.; Pfeiffer, M.; Engel, A.; Gaub, H. E.; uuml; ller, D. J., *Science* **2000,** 288, (5463), 143-146.

21. Florin, E. L.; Moy, V. T.; Gaub, H. E., *Science* **1994,** 264, (5157), 415-417.

22. Smith, B. L.*, et al.*, *Nature* **1999,** 399, (6738), 761-763.

23. Oberhauser, A. F.; Marszalek, P. E.; Erickson, H. P.; Fernandez, J. M., *Nature* **1998,** 393, (6681), 181-185.

24. Bustamante, C.; Marko, J. F.; Siggia, E. D.; Smith, S., *Science* **1994,** 265, (5178), 1599-1600.

25. Rief, M.; Gautel, M.; Oesterhelt, F.; Fernandez, J. M.; Gaub, H. E., *Science* **1997,** 276, (5315), 1109-1112.

26. Mueller, H.; Butt, H.-J.; Bamberg, E., *Biophys. J.* **1999,** 76, (2), 1072-1079.

27. Thompson, J. B.; Kindt, J. H.; Drake, B.; Hansma, H. G.; Morse, D. E.; Hansma, P. K., *Nature* **2001,** 414, (6865), 773-776.

28. Xu, G.; Liu, R.; Zak, O.; Aisen, P.; Chance, M. R., *Mol. Cell Proteomics* **2005,** 4, (12), 1959-1967.

29. Silvi, B.; Savin, A., *Nature* **1994,** 371, (6499), 683-686.

30. Wilhelm, C.; Billotey, C.; Roger, J.; Pons, J. N.; Bacri, J. C.; Gazeau, F., *Biomaterials* **2003,** 24, (6), 1001-1011.

31. Conner, S. D.; Schmid, S. L., *Nature* **2003,** 422, (6927), 37-44.

32. Tekle, C.; Deurs, B. v.; Sandvig, K.; Iversen, T.-G., *Nano Lett.* **2008,** 8, (7), 1858-1865.

33. Yersin, A.; Osada, T.; Ikai, A., *Biophys. J.* **2008,** 94, (1), 230-240.

34. Thakkar, H.; Lowe, P. A.; Price, C. P.; Newman, D. J., *Kidney Int.* **1998,** 54, (4), 1197-1205.

35. Babu, S.; Velez, A.; Wozniak, K.; Szydlowska, J.; Seal, S., *Chem. Phys. Lett.* **2007,** 442, (4-6), 405-408.

36. Babu, S.; Schulte, A.; Seal, S., *Appl. Phys. Lett.* **2008,** 92, (12), 123112-3.

4.6 Supporting Information

4.6.1 Transferrin

Transferrin (Tf) is a glycoprotein with a molecular mass of 76-81 kDa and consists of a single polypeptide chain of 679 amino acid residues.[1] This amino acid chain (Figure 4.6) is folded into two homologous globular domains with high affinity binding site for ferric ion.[2] The first domain (contains 1 to 336 amino acid residues) is designated as the N-lobe and the second domain (contains 337 to 679 amino acid residues) is designated as the C lobe. Both the lobes consist of a mixture of β-sheets connected by α-helix and non-helical loops.[3] Human holo-Transferrin obtained from Sigma-Aldrich Chemical Inc., was used for the cellular uptake experiments.

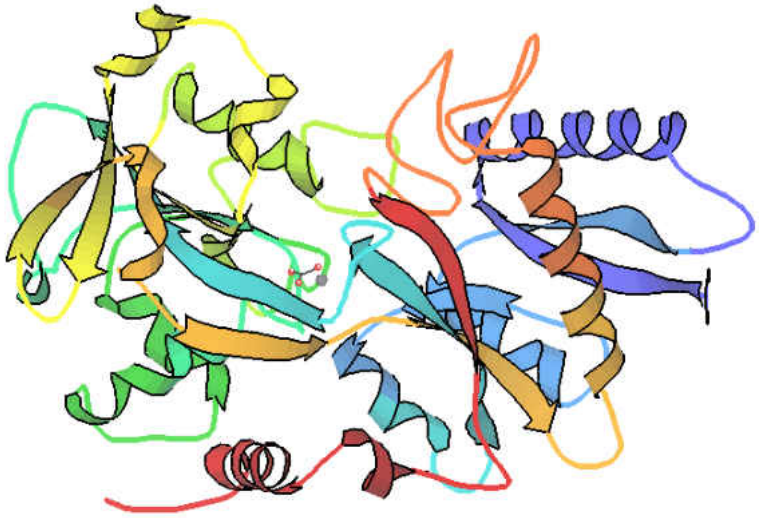

Figure 4.6: The structure and sequence of a human Tf. X-ray crystal structure of the N-lobe of human Tf.4 The helical groups indicate the α-helix, arrows indicate the β-sheets and the thin lines indicate the non-helical groups.

4.6.2 Cerium Oxide Nanoparticle Synthesis

Cerium nitrate hexahydrate (Sigma-Aldrich Chemical Inc.) was used as a precursor for synthesizing CNPs.[5] 0.5N ammonium hydroxide solution was added to 0.1M aqueous cerium nitrate solution and stirred at 300 rpm for 4 hours. The precipitated nanoparticles were centrifuged and washed with water multiple times to remove any impurities attached to the surface. Resultant nanoparticle powder was dried at 100°C and was analyzed by both X-ray diffraction (Rigaku Model) and high resolution transmission electron microscopy (Philips Tecnai series). HRTEM and AFM images shown in Figure 4.1a,b demonstrate the structural morphology and size distribution of CNPs. Figure 4.1c shows the XRD pattern collected from CNPs.

4.6.3 Tuning the Surface Charges of Cerium Oxide Nanoparticles

To tune the surface charges of CNPs, we treated them with acidic and basic pH buffers. All buffers were specially prepared to ensure that each one had the same type of ions in the solution. Buffers were synthesized using 25 mL of 0.2 M KCl solution and 75 mL deionized water. HCl or KOH solutions were added as necessary to adjust the pH. The surface charges of CNPs were varied by treating 5 mg of the CNPs with 5 mL pH buffer at a 1 mg/mL concentration. The solution was then ultrasonicated for an hour and stirred using a magnetic stirrer for another 24 hours followed by centrifuging and re-dispersing in 5 mL deionized water. The ultrasonication and stirring cycles were repeated and the solutions were centrifuged at 65000 rpm for 10 minutes to precipitate the larger agglomerates. The supernatant solutions were then collected for ZP measurements by the

Zetasizer (Nano-ZS) from Malvern Instruments. Figure 4.1d shows the ZP graph obtained on pH buffer treated CNPs.

4.6.4 Transferrin Coating on Cerium Oxide Nanoparticles

To coat CNPs with Tf, we mixed 1 mg/mL of CNPs solution with 1 mg/mL concentration of Tf solution and stirred for one hour using a magnetic stirrer. Both the solutions were prepared using deionized water and the CNPs solution was ultrasonicated for an hour before adding the protein solution.

4.6.5 Primary Culture of Human Lung Adenocarcinoma Epithelial Cells and Human Embryo Lung Fibroblast Cells

Human lung adenocarcinoma epithelial (A549) and human embryo lung fibroblast cell lines (WI-38) were obtained from the American Type Culture Collection (Manassas, VA). WI-38 cells were cultured in Eagle's Minimum Essential Medium (EMEM) with Earle's balanced salt solution, non-essential amino acids, sodium pyruvate, 10% FBS, 50 µg/mL streptomycin, and 50 IU/mL penicillin. A549 cells were cultured in Dulbecco's modification of Eagle's medium (DMEM) supplemented with L-glutamine, sodium pyruvate, 4.5 g/L glucose, 100 µg/mL streptomycin, 100 IU/mL penicillin (Mediatech, Herndon, VA), and 10 % fetal bovine serum (FBS, Equi-tech Bio, Kerrville, TX). Culture monolayers were maintained at 37^{o}C in a humidified atmosphere containing 5% CO_2. Cells were incubated for 24 hours with nanoparticles and then collected and washed with PBS to remove excess media and particles that were adsorbed on the surface of the cells. Cells incubated with CNPs were analyzed for their cerium content using a Thermo

Electron X-Series inductively coupled plasma mass spectrometer (ICP-MS), following APHA method 3125B to determine the amount of CNPs taken up by the cells.

4.6.6 TEM Biological Cell Sample Preparations

Human lung adenocarcinoma epithelial (A549) and human embryo lung fibroblast cell lines (WI-38) were cultured as previously described and incubated with a concentration of 100 nM of Tf:CNPs or bare CNPs overnight. Cells were washed two times with PBS, harvested using trypsin and spun down at 3000 RPM for 3min. Supernatant was removed and pellets were re-suspended by pipetting quickly up and down in 1mL fixative (5% glutaraldehyde, 4.4% formaldehyde, 2.75% picric acid 0.05M NaCaCo) solution. Samples were then cooled to 4^{o}C. TEM samples were prepared by fixing them using a Poly/Bed 812 embedding media from Polysciences, Inc. Cells were then examined using a Zeiss 10 CA TEM at 60 keV beam energy.

4.6.7 Single Molecule Force Spectroscopy (SMFS)

Force measurements were carried out using Solver pro Scanning Probe Microscopy (SPM) with a SMENA controller from NT-MDT, Moscow, Russia. We used succinimide functionalized gold coated silicon nitride cantilevers (purchased from Novascan technologies) with an average spring constant of 0.05 N/m and a tip curvature radius of ~10 nm for force measurements. Cantilevers were washed with deionized water and air dried. Tf solution was prepared by adding 10 mg of Tf powder into 10 mL deionized water, and the resulting solution was used for conjugating a succinimide terminated AFM probe with Tf. AFM probes were placed in the protein solution for half an hour and then

washed three times with phosphate buffer solution (PBS) followed by three more washes with deionized water. Multiple washing eliminates loosely bound protein molecules hanging from the AFM tip. SMFS samples were prepared by drop coating CNPs onto an atomically smooth silicon surface. The forces of interaction between Tf and CNPs were measured by lowering the probe tip close to the NP surface and retracting it until the protein-NP bond breaks. Force-distance spectroscopy measurements were carried out multiple times at different locations on CNPs coated silicon samples and the corresponding force values were plotted in the form of histograms. Experiments were repeated multiple times until a minimum of 100 force interaction curves were obtained for each sample. The force-distance spectrum yields 1000 points for each of the approach and retraction portions of the cycle.

4.6.8 Transferrin Interaction with Silicon

To understand the interaction mode and conformational changes of Tf, SMFS measurements were conducted on an atomically smooth silicon (Si) substrate in aqueous medium using Tf coated AFM probes. The obtained force deflection data was converted to force against displacement of the tip from the sample surface using the following equation.

$$D(t) = z(t) - \partial(z)/s \tag{4.2}$$

where $D(t)$ is the distance between the AFM probe and the surface in nm, $z(t)$ is the piezostage displacement, $\delta(z)$ is the cantilever deflection in nanoampere (nA) and s is the sensitivity of the cantilever determined by calculating the slope of the part of the force-

distance curve reflecting the bending of the cantilever obtained on silicon sample. The force *F(z)* is calculated by using the Hooke's law for a linear elastic spring (cantilever) as

$$F(z) = k_c \partial(z) / s \tag{4.3}$$

where k_c is the spring constant of the cantilever. Figure 4.7a shows the deflection-extension profile of Tf-Si interaction. The corresponding force-extension profile is also shown in Figure 4.7b. During the retraction process, Tf molecules were stretched until the applied force exceeded the adhesion between the protein molecule and the silicon substrate. This leads to the detachment of the protein molecule from the substrate followed by a sudden decrease in the force exerted by the cantilever. The AFM probe and the Tf molecule experienced a pull of force of 2.658 nN and 542 pN respectively on the silicon substrate. At a neutral pH, silicon with a thin native oxide layer exhibits negative charges on the surface and Tf is therefore expected to have less interaction with silicon. However, due to surface charge differences, silicon nitride AFM tip showed a strong interaction with the silicon surface. WLC fitting calculations yielded a persistence length value of 0.5 nm. The contour length obtained for the interaction of Tf with the silicon substrate is 104.8±0.9 nm (Figure 4.7b). Assuming that each amino acid contributes ~0.38 nm to the contour length of a fully extended chain, a polypeptide chain of ~276 amino acids of Tf was stretched during this pull-off experiment. The contour length (104.8±0.9) of the stretched portion of Tf was smaller than an estimated fully extended length of Tf (~257 nm). This could be due to the unfolding of part of the peptide chain (most likely just one of the two domains of the protein) because of the lower interacting forces acting between the Tf and silicon surface. According to the WLC model, prior to

the stretching the protein experienced a force of ~305 nN, and during stretching the protein experienced an additional force of ~237 nN. SMFS measurements conducted on the silicon substrate helped us better understand the interaction behavior of Tf with surfaces by correlating the stretching pattern of Tf with its structural conformations.

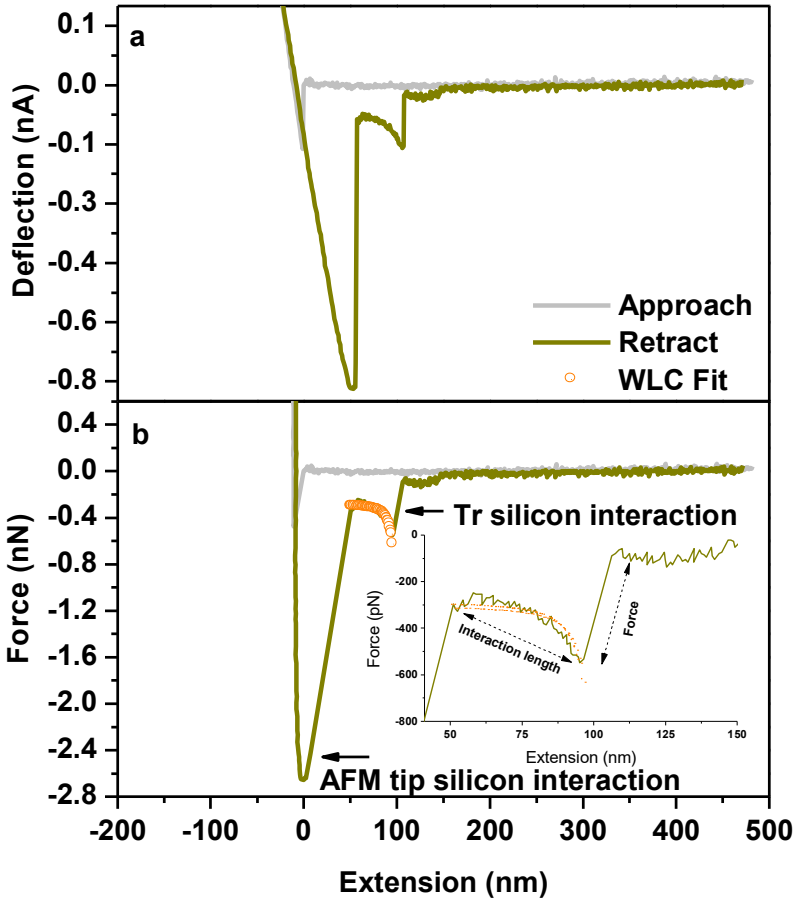

Figure 4.7: (a) The deflection-extension spectrum of a Tf coated AFM probe interacting with silicon substrate; (b) the corresponding force-extension spectrum of a Tf coated AFM probe interacting with silicon. The AFM probe and the Tf molecule experienced a pull of force of 2.658 nN and 542 pN respectively.

4.6.9 Characteristic Domain Unfolding of Transferrin

SMFS experiments performed on all the three types of NPs samples (NPs with ZPs +36.4±0.7 mV, +5.9±1.2 mV, and -35.1±0.9 mV) displayed saw tooth like unfolding force curves with multiple force jumps. The force-extension spectrum shown in Figure 4.8 (corresponding to the interaction of Tf with +5.9±1.2 mV charged CNPs) was fitted with a persistence length of 0.4 nm and the WLC fit yielded a contour length of 145.75±2.1, 111±6.5, and 87.02±3.4 for the three force jumps. These contour lengths correspond to the stretching of polypeptide chains of ~384, ~294 and ~229 amino acid residues. Since each domains of Tf consists of ~330 amino acid groups, the above contour lengths indicate the characteristic domain unfolding of more than one interacting protein.

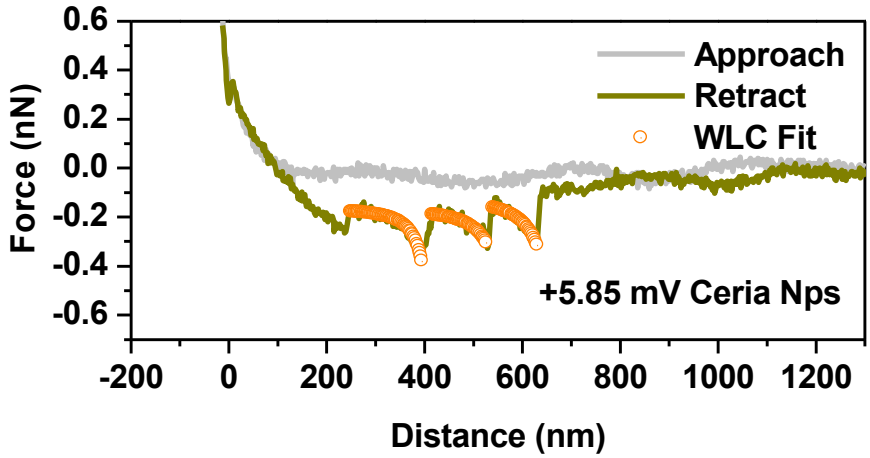

Figure 4.8: Characteristic domain unfolding of Tf interacting with CNPs. These force jumps appeared to represent the characteristic domain unfolding usually seen in SMFS of giant protein molecules.

4.6.10 Attenuated Total Reflectance Fourier Transform Infrared Spectroscopy (ATR FT-IR) Analysis of Transferrin Coated Ceria Nanoparticles

In order to confirm the surface functionalization of CNPs with Tf, ATR FT-IR characterization was carried out. Tf:CNPs were obtained by mixing the protein solution with positively charged CNPs that were then centrifuged and washed with water to remove any loosely adhered Tf. Dried Tf:CNPs powder was analyzed by ATR FT-IR measurements. The spectrum was recorded using a Perkin-Elmer (Spectrum one) FT-IR spectrometer in the range of 4000 to 600 cm^{-1} with a resolution of 2 cm^{-1}. Figure 4.9 shows the ATR FT-IR measurements conducted on pure Tf, pure CNPs, and Tf:CNPs. No characteristic features were observed for pure CNPs. A broad peak was observed for both Tf and Tf:CNP around 3400 cm^{-1} due to the presence of hydroxyl groups. Tf:CNPs show peaks at 1640 and 1516 cm^{-1} which can be assigned to the presence of amide C=O groups (from amide I band) and vibrations of tyrosine side chains, respectively.[6] The presence of different functional groups such as C=C (1520 cm^{-1}), OH (1330 cm^{-1}), C-O (1155 cm^{-1}) and CH (846 cm^{-1}) in the ATR FT-IR spectrum of Tf:CNPs confirms the presence of Tf coating on the surface of CNPs.

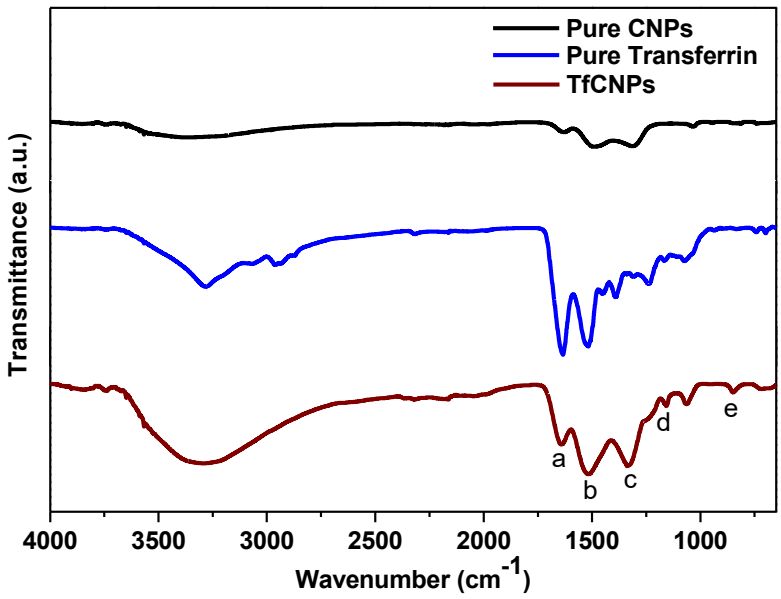

Figure 4.9: ATR-IR spectra of pure CNPs, pure Tf and Tf:CNPs. Vibration peaks corresponding to (a) C=O (1640 cm^{-1} from amide I band), (b) C=C (1520 cm^{-1}), (c) OH (1330 cm^{-1}), (d) C-O (1155 cm^{-1}) and (e) CH (846 cm^{-1}) confirm the presence of Tf coating on the surface of CNPs.

4.6.11 X-Ray Photoelectron Spectral (XPS) Studies of Transferrin Coated Ceria Nanoparticles

The Tf coating on CNPs was examined using a 5400 PHI ESCA X-ray photo electron spectrometer (XPS). The base pressure during the XPS analysis was approximately 10^{-9} Torr, and Mg Kα X-radiation (1253.6 eV) at a power of 300 W was used for sample irradiation. The instrument was calibrated using a standard gold sample at a binding energy of 84.0 ± 0.1 eV for the Au($4f_{7/2}$) peak. All the samples were prepared by pressing them onto an In foil. Figure 4.10 shows the XPS spectra recorded for Tf:CNPs corresponding to cerium Ce(3*d*) and iron Fe(2*p*) in Tf:CNPs. Cerium has a complex spectrum due to multiple 3d splitting as well as mixed oxidation states (+3 and +4).[7] The

iron XPS peaks, Fe($2p_{1/2}$) and Fe($2p_{3/2}$) resulting from holo-Tf confirms the presence of Tf on Tf:CNPs.

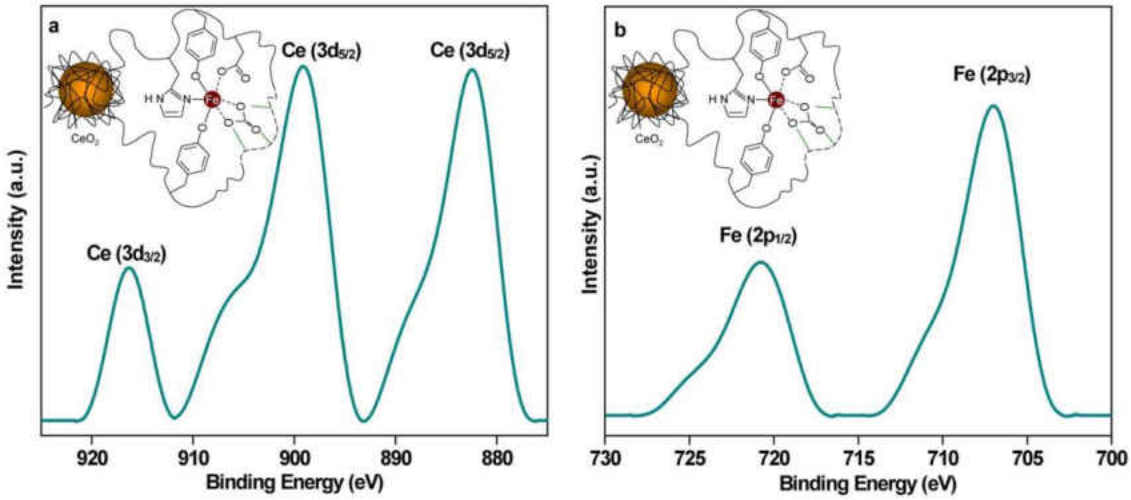

Figure 4.10: High resolution X-ray photoelectron spectra for (a) Ce(3*d*) and (b) Fe(2*p*) indicating the presence of Ce and Fe in Tf:CNPs. The cartoon diagram of Tf:CNP shows the magnified view six-coordinate iron binding site in Tf. The coordination geometry is a distorted octahedral. The carbonate ion is held in place by hydrogen bonds (green lines) to the amino acid side-chains.

4.6.12 UV-Vis Analysis of Transferrin Coated Ceria Nanoparticles

The amount of proteins adsorbed on CNPs was calculated using the equation:

$$q = (C_i - C_f)V/m \tag{4.5}$$

where C_i and C_f correspond to the initial Tf concentrations and the final Tf concentration in the supernatant after centrifugation; V is the total volume of the solution; and m is the mass of the CNPs added into the solution. The Tf concentration values are calculated by measuring the UV absorbance maximum at 280 nm wavelengths on Tf:CNPs and using a standard absorption calibration curve obtained on known concentrations of Tf (Figure 4.11). Tf:CNPs showed a protein adsorption of approximately 500 mg/g of CNPs.

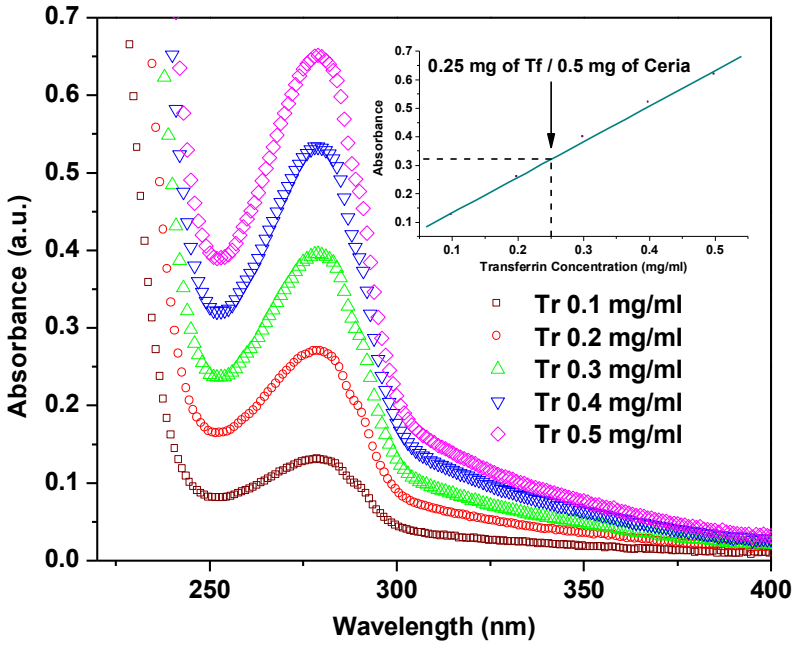

Figure 4.11: UV-Visible spectroscopy measurements were carried out for known concentrations of Tf at the absorbance maximum of 280 nm. Inset shows the calibration curve prepared using known concentrations (0.1 to 0.5 mg/mL) of Tf.

4.6.13 TEM Images of Cells Incubated With Ceria Nanoparticles

Figure 4.12 shows the TEM images of A549 and WI-38 cells incubated with CNPs. A549 cells incubated with bare CNPs did not show much cellular uptake. Similarly, in the case of WI-38 cells, Tf:CNPs showed fewer uptakes and appeared as if they were trapped near the cell membrane and did not show much diffusion into the cell.

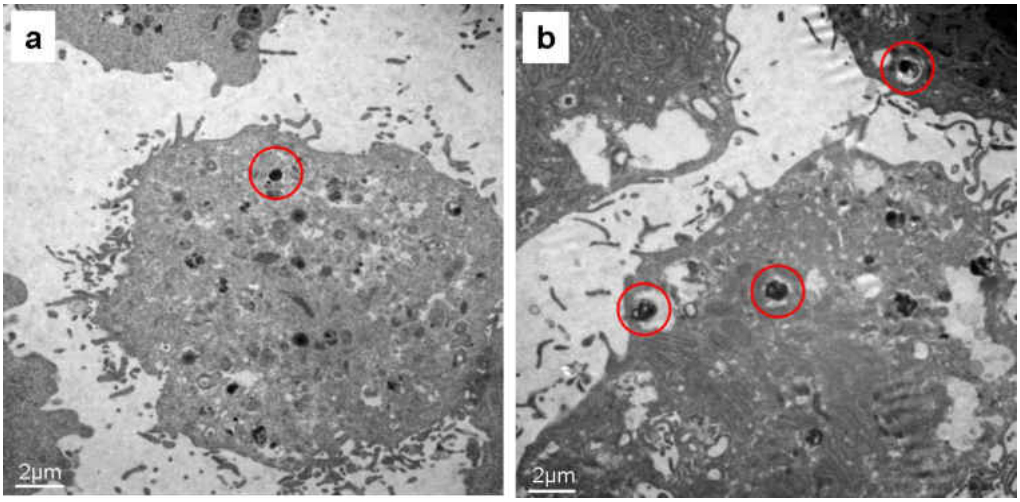

Figure 4.12: (a) TEM image of A549 cancer cells incubated with bare CNPs; (b) TEM image of WI-38 healthy cells incubated with Tf:CNPs. Red circles represent the positions of the nanoparticles in the cells.

4.6.14 Computational Details

All calculations presented were carried out with the plane-wave based Vienna *ab initio* simulation package (VASP).[8, 9] The electronic ground state was determined by using local density (LDA) approximation. We used the LDA+*U* version with local parts described by Ceperley-Adler functional. On site Coulomb and exchange interactions are treated by a single effective parameter *U*-*J*. Plane waves were included up to an energetic cutoff of 415 eV and electronic wave functions were described using the projected augmented wave (PAW) method and *U*-*J*=5 eV.[10] These calculation parameters were recently employed for investigation of cerium oxide and it was shown that the LDA+*U* approximation demonstrates better agreement with experiments than GGA+*U* approach.[11] Super cells were chosen with at least 10 Å between replicas to remove spurious periodic interactions while Coulomb interactions between periodic charged images were compensated according to procedure described earlier.[12]

4.6.15 References for Supporting Information

1. Briggs, D. A.; Sharp, D. J.; Miller, D.; Gosden, R. G., *Mol. Hum. Reprod.* **1999,** 5, (12), 1107-1114.

2. Wally, J.; Halbrooks, P. J.; Vonrhein, C.; Rould, M. A.; Everse, S. J.; Mason, A. B.; Buchanan, S. K., *J. Biol. Chem.* **2006,** 281, (34), 24934-24944.

3. Welch, S., *Transferrin: The Iron Carrier*. CRC: Boca Raton, FL, 1992; p 291.

4. Macgillivray, R.T.A.; Moore, S.A.; Chen, J.; Anderson, B.F.; Baker, H.; Luo, Y.; Bewley, M.; Smith, C.A.; Murphy, M.E.P.; Wang, Y.; Mason, A.B.; Woodworth, R.C.; Brayer, G.D.; Baker, E.N., *Protein Data Bank (www.rcsb.org)* **1998**, PDB ID 1a8e, DOI 10.2210/pdb1a8e/pdb.

5. Babu, S.; Schulte, A.; Seal, S., *Appl. Phys. Lett.* **2008,** 92, (12), 123112-3.

6. Hadden, J. M.; Bloemendal, M.; Haris, P. I.; Srai, S. K. S.; Chapman, D., *Biochim. Biophys. Acta* **1994,** 1205, (1), 59-67.

7. Tsunekawa, S.; Fukuda, T.; Kasuya, A., *Surf. Sci.* **2000,** 457, (3), L437-L440.

8. Kresse, G.; Hafner, J., *Phys. Rev. B* **1993,** 47, (1), 558-561.

9. Kresse, G.; Furthmüller, J., *Phys. Rev. B* **1996,** 54, (16), 11169-11186.

10. Blöchl, P. E., *Phys. Rev. B* **1994,** 50, (24), 17953-17979.

11. Loschen, C.; Carrasco, J.; Neyman, K. M.; Illas, F., *Phys. Rev. B* **2007,** 75, (3), 035115-8.

12. Makov, G.; Payne, M. C., *Phys. Rev. B* **1995,** 51, (7), 4014-4022.

CHAPTER 5: SUMMARY, CHALLENGES AND FUTURE SCOPE

Atomic force microscopy (AFM) based force-distance (F-D) spectroscopy have been shown to be a unique characterization technique for understanding the basic materials properties such as the intra-atomic interaction forces determining the surface adhesion and inter-atomic interaction forces determining the mechanical strength of the materials. Cancer cells targeted drug delivery of therapeutics is always a challenging task for the biomedical researchers. A significant contribution of this dissertation is an insight into the possible way of functionalizing cerium oxide nanoparticles (CNPs) for preferential cellular uptake. This dissertation discuss in detail about the use of AFM based single molecule force spectroscopy (SMFS) in probing picoNewton level interaction forces acting between the CNPs and transferrin protein (Tf) molecules. It is shown that, by suitably tuning the surface charges of the nanoparticles (NPs), a strong binding interaction between the ligand protein molecules and nanoparticles can be achieved in physiological pH conditions. This dissertation also discusses the density functional theory (DFT) simulations employed to understand the protein-nanoparticle interactions. The information on the nature of chemical bonding between the protein molecules and nanoparticles is a significant contribution of this dissertation. The cellular uptake studies proved the potentials of using transferrin protein coated nanoparticles for targeted drug delivery. The dissertation also discuss about the dynamic ion exchange reactions occurring on the surface of colloidal CNPs, leading to their natural time dependent surface charge reversal and its influence in determining the CNP's adhesion properties with organic (protein) and inorganic (silica) surfaces. Using DFT calculations, it is

demonstrated that the initial positive surface charges exhibited by CNPs are resulting from the adsorption of kinetically favourable H^+ ions onto their surface and the time dependent surface charge reversal towards the negative charges are due the adsoption of more thermodynamically favorable OH^- ions.

Similarly, this dissertation shows that by varying the nature of catalyst, it is possible to prepare silica nanoparticle thin film surfaces with roughness ranging from ~0.3 nm to ~16.2 nm and particle size varying from ~5.9 nm to ~99.5 nm. By applying F-D spectroscopy technique in the high force regime (<1 nN), the elastic properties of thin silica nanoparticle films of thickness varying from ~105 nm to ~635 nm is obtained. A correlation between the mechanical properties and the porosity of the thin films is another major contribution of this dissertation.

5.1 Challenges and Future Scope

It has been a challenging experience for the author and the collaborators involved in this work to understand the force-distance spectroscopy technique to explore the unique biological properties of CNPs. While the significance of this work has been emphasized in the previous section, there are still few observations remains indefinable. In addition to finding, unique observations related to the biological (cell, protein and DNA) interactions of CNPs, the experience from this dissertation research provided some specific directives based on which future studies on the biological interactions of CNPs and other nanoparticles should be undertaken.

Following are some questions that remained unanswered at the time of this dissertation submission:

- Can the protein undergo confirmation changes, while it is adsorbed on to the NP surface?
- Is it possible to retain a strong binding adhesion between the NPs and protein molecules during in vivo experiments?
- Is there a chance that blood proteins can get adsorbed on to the NPs during targeted drug delivery transportation process?
- Will the phagocytes remove protein coated NPs from the blood stream during their transportation inside the body?

Most of the above-mentioned observations are significant in drug delivery and imaging related therapeutics applications. Physiochemical and biological modifications of the nanoparticle surfaces can play a vital role in designing nanosize drug carriers, which may preferentially target and deliver therapeutic drugs to malignant cells in human body. Hence, it is essential to understand all possible surface physical and surface chemical properties of biocompatable nonmaterials that can have possible impact on their behavior in significant applications.

APPENDIX A: PUBLICATIONS FROM THE THESIS

From chapter 2: Vincent, A; Babu S.; Seal, S., "Surface elastic properties of porous nano-silica coatings by scanning force microscopy", *Applied Physics Letters* **2007**, 91, 161901-1-161901-3.

From chapter 2: Vincent, A.; Babu, S.; Brinley, E.; Karakoti, A. S.; Deshpande, S.; Seal, S., "Role of catalyst on refractive index tunability of porous silica antireflective coatings by sol-gel technique", *Journal of Physical Chemistry C* **2007**, 111 (23), 8291-8298.

From chapter 3: Vincent, A.; Inerbaev, T. M.; Babu, S.; Karakoti, A. S.; Masunov, A.; Seal, S., "Tuning Hydrated Nanoceria Surfaces: Experimental/Theoretical Investigations of Ion Exchange and Implications in Organic and Inorganic Interactions", *Langmuir* **Article ASAP**.

From chapter 4: Vincent, A.; Babu, S.; Heckert, E.; Dowding, J.; Self, W. T.; Hirst, S. M.; Reilly, C. M.; Inerbaev, T. M.; Masunov, A.; Rahman, T. S.; Seal, S., **"**Protonated nanoparticle surface governing ligand tethering and tumor targeting", *ACS Nano* **2009**, 3 (5), 1203-1211.

APPENDIX B: LETTERS OF PERMISSION

AMERICAN CHEMICAL SOCIETY LICENSE
TERMS AND CONDITIONS
Mar 10, 2010

This is a License Agreement between Abhilash Vincent ("You") and American Chemical Society ("American Chemical Society") provided by Copyright Clearance Center ("CCC"). The license consists of your order details, the terms and conditions provided by American Chemical Society, and the payment terms and conditions.

All payments must be made in full to CCC. For payment instructions, please see information listed at the bottom of this form.

License Number	2385081208816
License Date	Mar 09, 2010
Licensed content publisher	American Chemical Society
Licensed content publication	The Journal of Physical Chemistry C
Licensed content title	Role of Catalyst on Refractive Index Tunability of Porous Silica Antireflective Coatings by Sol-Gel Technique
Licensed content author	Abhilash Vincent et al.
Licensed content date	Jun 1, 2007
Volume number	111
Issue number	23
Type of Use	Thesis/Dissertation
Requestor type	Not specified
Format	Print
Portion	Full article
Author of this ACS article	Yes
Order reference number	
Expected completion date	Mar 2010
Estimated size(pages)	142
Billing Type	Invoice
Billing Address	12002 Pasteur Dr.

	APT-316 Orlando, FL 32826 United States
Customer reference info	
Total	0.00 USD
Terms and Conditions	

Thesis/Dissertation

ACS / RIGHTSLINK TERMS & CONDITIONS
THESIS/DISSERTATION

INTRODUCTION
The publisher for this copyrighted material is the American Chemical Society. By clicking "accept" in connection with completing this licensing transaction, you agree that the following terms and conditions apply to this transaction (along with the Billing and Payment terms and conditions established by Copyright Clearance Center, Inc. ("CCC"), at the time that you opened your Rightslink account and that are available at any time at <http://myaccount.copyright.com>).

LIMITED LICENSE
Publisher hereby grants to you a non-exclusive license to use this material. Licenses are for one-time use only with a maximum distribution equal to the number that you identified in the licensing process; any form of republication must be completed within 60 days from the date hereof (although copies prepared before then may be distributed thereafter).

GEOGRAPHIC RIGHTS: SCOPE
Licenses may be exercised anywhere in the world.

RESERVATION OF RIGHTS
Publisher reserves all rights not specifically granted in the combination of (i) the license details provided by you and accepted in the course of this licensing transaction, (ii) these terms and conditions and (iii) CCC's Billing and Payment terms and conditions.

PORTION RIGHTS STATEMENT: DISCLAIMER
If you seek to reuse a portion from an ACS publication, it is your responsibility to examine each portion as published to determine whether a credit to, or copyright notice of, a third party owner was published adjacent to the item. You may only obtain permission via Rightslink to use material owned by ACS. Permission to use any material published in an ACS publication, journal, or article which is reprinted with permission of a third party must be obtained from the third party owner. ACS disclaims any responsibility for any use you

make of items owned by third parties without their permission.

REVOCATION
The American Chemical Society reserves the right to revoke a license for any reason, including but not limited to advertising and promotional uses of ACS content, third party usage, and incorrect figure source attribution.

LICENSE CONTINGENT ON PAYMENT
While you may exercise the rights licensed immediately upon issuance of the license at the end of the licensing process for the transaction, provided that you have disclosed complete and accurate details of your proposed use, no license is finally effective unless and until full payment is received from you (by CCC) as provided in CCC's Billing and Payment terms and conditions. If full payment is not received on a timely basis, then any license preliminarily granted shall be deemed automatically revoked and shall be void as if never granted. Further, in the event that you breach any of these terms and conditions or any of CCC's Billing and Payment terms and conditions, the license is automatically revoked and shall be void as if never granted. Use of materials as described in a revoked license, as well as any use of the materials beyond the scope of an unrevoked license, may constitute copyright infringement and publisher reserves the right to take any and all action to protect its copyright in the materials.

COPYRIGHT NOTICE: DISCLAIMER
You must include the following copyright and permission notice in connection with any reproduction of the licensed material: "Reprinted (“Adapted” or “in part”) with permission from REFERENCE CITATION. Copyright YEAR American Chemical Society."

WARRANTIES: NONE
Publisher makes no representations or warranties with respect to the licensed material.

INDEMNITY
You hereby indemnify and agree to hold harmless publisher and CCC, and their respective officers, directors, employees and agents, from and against any and all claims arising out of your use of the licensed material other than as specifically authorized pursuant to this license.

NO TRANSFER OF LICENSE
This license is personal to you or your publisher and may not be sublicensed, assigned, or transferred by you to any other person without publisher's written permission.

NO AMENDMENT EXCEPT IN WRITING
This license may not be amended except in a writing signed by both parties (or, in the case of publisher, by CCC on publisher's behalf).

OBJECTION TO CONTRARY TERMS

Publisher hereby objects to any terms contained in any purchase order, acknowledgment, check endorsement or other writing prepared by you, which terms are inconsistent with these terms and conditions or CCC's Billing and Payment terms and conditions. These terms and conditions, together with CCC's Billing and Payment terms and conditions (which are incorporated herein), comprise the entire agreement between you and publisher (and CCC) concerning this licensing transaction. In the event of any conflict between your obligations established by these terms and conditions and those established by CCC's Billing and Payment terms and conditions, these terms and conditions shall control.

JURISDICTION
This license transaction shall be governed by and construed in accordance with the laws of the District of Columbia. You hereby agree to submit to the jurisdiction of the courts located in the District of Columbia for purposes of resolving any disputes that may arise in connection with this licensing transaction.

THESES/DISSERTATION TERMS
Publishing implications of electronic publication of theses and dissertation material
Students and their mentors should be aware that posting of theses and dissertation material on the Web prior to submission of material from that thesis or dissertation to an ACS journal may affect publication in that journal. Whether Web posting is considered prior publication may be evaluated on a case-by-case basis by the journal's editor. If an ACS journal editor considers Web posting to be "prior publication", the paper will not be accepted for publication in that journal. If you intend to submit your unpublished paper to ACS for publication, check with the appropriate editor prior to posting your manuscript electronically.

If your paper has already been published by ACS and you want to include the text or portions of the text in your thesis/dissertation in **print or microfilm formats**, please print the ACS copyright credit line on the first page of your article: "Reproduced (or 'Reproduced in part') with permission from [FULL REFERENCE CITATION.] Copyright [YEAR] American Chemical Society." Include appropriate information.

Submission to a Dissertation Distributor: If you plan to submit your thesis to UMI or to another dissertation distributor, you should not include the unpublished ACS paper in your thesis if the thesis will be disseminated electronically, until ACS has published your paper. After publication of the paper by ACS, you may release the entire thesis (**not the individual ACS article by itself**) for electronic dissemination through the distributor; ACS's copyright credit line should be printed on the first page of the ACS paper.

Use on an Intranet: The inclusion of your ACS unpublished or published manuscript is permitted in your thesis in print and microfilm formats. If ACS has published your paper you may include the manuscript in your thesis on an intranet that is not publicly available. Your ACS article cannot be posted electronically on a publicly available medium (i.e. one that is not password protected), such as but not limited to, electronic archives, Internet,

library server, etc. The only material from your paper that can be posted on a public electronic medium is the article abstract, figures, and tables, and you may link to the article's DOI or post the article's author-directed URL link provided by ACS. This paragraph does not pertain to the dissertation distributor paragraph above.

Other conditions:

v1.1

Gratis licenses (referencing $0 in the Total field) are free. Please retain this printable license for your reference. No payment is required.

If you would like to pay for this license now, please remit this license along with your payment made payable to "COPYRIGHT CLEARANCE CENTER" otherwise you will be invoiced within 48 hours of the license date. Payment should be in the form of a check or money order referencing your account number and this invoice number RLNK10747983.
Once you receive your invoice for this order, you may pay your invoice by credit card. Please follow instructions provided at that time.

Make Payment To:
Copyright Clearance Center
Dept 001
P.O. Box 843006
Boston, MA 02284-3006

If you find copyrighted material related to this license will not be used and wish to cancel, please contact us referencing this license number 2385081208816 and noting the reason for cancellation.

Questions? customercare@copyright.com or +1-877-622-5543 (toll free in the US) or +1-978-646-2777.

AMERICAN INSTITUTE OF PHYSICS LICENSE
TERMS AND CONDITIONS
Mar 10, 2010

This is a License Agreement between Abhilash Vincent ("You") and American Institute of Physics ("American Institute of Physics") provided by Copyright Clearance Center ("CCC"). The license consists of your order details, the terms and conditions provided by American Institute of Physics, and the payment terms and conditions.

All payments must be made in full to CCC. For payment instructions, please see information listed at the bottom of this form.

License Number	2385660893212
License date	Mar 10, 2010
Licensed content publisher	American Institute of Physics
Licensed content publication	Applied Physics Letters
Licensed content title	Surface elastic properties of porous nanosilica coatings by scanning force microscopy
Licensed content author	A. Vincent, S. Babu, S. Seal
Licensed content date	Oct 15, 2007
Volume number	91
Issue number	16
Type of Use	Thesis/Dissertation
Requestor type	Author (original article)
Format	Print and electronic
Portion	Excerpt (> 800 words)
Will you be translating?	No
Title of your thesis / dissertation	PROBING THE NANOSCALE INTERACTION FORCES AND ELASTIC PROPERTIES OF ORGANIC AND INORGANIC MATERIALS USING FORCE DISTANCE (F-D) SPECTROSCOPY
Expected completion date	Mar 2010
Estimated size (number of pages)	142
Total	0.00 USD

Terms and Conditions

American Institute of Physics -- Terms and Conditions: Permissions Uses

American Institute of Physics ("AIP") hereby grants to you the non-exclusive right and license to use and/or distribute the Material according to the use specified in your order, on a one-time basis, for the specified term, with a maximum distribution equal to the number that you have ordered. Any links or other content accompanying the Material are not the subject of this license.

1. You agree to include the following copyright and permission notice with the reproduction of the Material: "Reprinted with permission from [FULL CITATION]. Copyright [PUBLICATION YEAR], American Institute of Physics." For an article, the copyright and permission notice must be printed on the first page of the article or book chapter. For photographs, covers, or tables, the copyright and permission notice may appear with the Material, in a footnote, or in the reference list.
2. If you have licensed reuse of a figure, photograph, cover, or table, it is your responsibility to ensure that the material is original to AIP and does not contain the copyright of another entity, and that the copyright notice of the figure, photograph, cover, or table does not indicate that it was reprinted by AIP, with permission, from another source. Under no circumstances does AIP, purport or intend to grant permission to reuse material to which it does not hold copyright.
3. You may not alter or modify the Material in any manner. You may translate the Material into another language only if you have licensed translation rights. You may not use the Material for promotional purposes. AIP reserves all rights not specifically granted herein.
4. The foregoing license shall not take effect unless and until AIP or its agent, Copyright Clearance Center, receives the Payment in accordance with Copyright Clearance Center Billing and Payment Terms and Conditions, which are incorporated herein by reference.
5. AIP or the Copyright Clearance Center may, within two business days of granting this license, revoke the license for any reason whatsoever, with a full refund payable to you. Should you violate the terms of this license at any time, AIP, American Institute of Physics, or Copyright Clearance Center may revoke the license with no refund to you. Notice of such revocation will be made using the contact information provided by you. Failure to receive such notice will not nullify the revocation.
6. AIP makes no representations or warranties with respect to the Material. You agree to indemnify and hold harmless AIP, American Institute of Physics, and their officers, directors, employees or agents from and against any and all claims arising out of your use of the Material other than as specifically authorized herein.
7. The permission granted herein is personal to you and is not transferable or assignable without the prior written permission of AIP. This license may not be amended except in a writing signed by the party to be charged.
8. If purchase orders, acknowledgments or check endorsements are issued on any forms containing terms and conditions which are inconsistent with these provisions, such inconsistent terms and conditions shall be of no force and effect. This document, including the CCC Billing and Payment Terms and Conditions, shall be

the entire agreement between the parties relating to the subject matter hereof.

This Agreement shall be governed by and construed in accordance with the laws of the State of New York. Both parties hereby submit to the jurisdiction of the courts of New York County for purposes of resolving any disputes that may arise hereunder.

Gratis licenses (referencing $0 in the Total field) are free. Please retain this printable license for your reference. No payment is required.

If you would like to pay for this license now, please remit this license along with your payment made payable to "COPYRIGHT CLEARANCE CENTER" otherwise you will be invoiced within 48 hours of the license date. Payment should be in the form of a check or money order referencing your account number and this invoice number RLNK10748703.
Once you receive your invoice for this order, you may pay your invoice by credit card. Please follow instructions provided at that time.

Make Payment To:
Copyright Clearance Center
Dept 001
P.O. Box 843006
Boston, MA 02284-3006

If you find copyrighted material related to this license will not be used and wish to cancel, please contact us referencing this license number 2385660893212 and noting the reason for cancellation.

Questions? customercare@copyright.com or +1-877-622-5543 (toll free in the US) or +1-978-646-2777.

AMERICAN INSTITUTE OF PHYSICS LICENSE
TERMS AND CONDITIONS
Mar 10, 2010

This is a License Agreement between Abhilash Vincent ("You") and American Institute of Physics ("American Institute of Physics") provided by Copyright Clearance Center ("CCC"). The license consists of your order details, the terms and conditions provided by American Institute of Physics, and the payment terms and conditions.

All payments must be made in full to CCC. For payment instructions, please see information listed at the bottom of this form.

License Number	2385651156752
License date	Mar 10, 2010
Licensed content publisher	American Institute of Physics
Licensed content publication	Applied Physics Letters
Licensed content title	Surface elastic properties of porous nanosilica coatings by scanning force microscopy
Licensed content author	A. Vincent, S. Babu, S. Seal
Licensed content date	Oct 15, 2007
Volume number	91
Issue number	16
Type of Use	Thesis/Dissertation
Requestor type	Author (original article)
Format	Print and electronic
Portion	Figure/Table
Number of figures/tables	4
Title of your thesis / dissertation	PROBING THE NANOSCALE INTERACTION FORCES AND ELASTIC PROPERTIES OF ORGANIC AND INORGANIC MATERIALS USING FORCE DISTANCE (F-D) SPECTROSCOPY
Expected completion date	Mar 2010
Estimated size (number of pages)	142
Total	0.00 USD

Terms and Conditions

American Institute of Physics -- Terms and Conditions: Permissions Uses

American Institute of Physics ("AIP") hereby grants to you the non-exclusive right and

license to use and/or distribute the Material according to the use specified in your order, on a one-time basis, for the specified term, with a maximum distribution equal to the number that you have ordered. Any links or other content accompanying the Material are not the subject of this license.

1. You agree to include the following copyright and permission notice with the reproduction of the Material: "Reprinted with permission from [FULL CITATION]. Copyright [PUBLICATION YEAR], American Institute of Physics." For an article, the copyright and permission notice must be printed on the first page of the article or book chapter. For photographs, covers, or tables, the copyright and permission notice may appear with the Material, in a footnote, or in the reference list.
2. If you have licensed reuse of a figure, photograph, cover, or table, it is your responsibility to ensure that the material is original to AIP and does not contain the copyright of another entity, and that the copyright notice of the figure, photograph, cover, or table does not indicate that it was reprinted by AIP, with permission, from another source. Under no circumstances does AIP, purport or intend to grant permission to reuse material to which it does not hold copyright.
3. You may not alter or modify the Material in any manner. You may translate the Material into another language only if you have licensed translation rights. You may not use the Material for promotional purposes. AIP reserves all rights not specifically granted herein.
4. The foregoing license shall not take effect unless and until AIP or its agent, Copyright Clearance Center, receives the Payment in accordance with Copyright Clearance Center Billing and Payment Terms and Conditions, which are incorporated herein by reference.
5. AIP or the Copyright Clearance Center may, within two business days of granting this license, revoke the license for any reason whatsoever, with a full refund payable to you. Should you violate the terms of this license at any time, AIP, American Institute of Physics, or Copyright Clearance Center may revoke the license with no refund to you. Notice of such revocation will be made using the contact information provided by you. Failure to receive such notice will not nullify the revocation.
6. AIP makes no representations or warranties with respect to the Material. You agree to indemnify and hold harmless AIP, American Institute of Physics, and their officers, directors, employees or agents from and against any and all claims arising out of your use of the Material other than as specifically authorized herein.
7. The permission granted herein is personal to you and is not transferable or assignable without the prior written permission of AIP. This license may not be amended except in a writing signed by the party to be charged.
8. If purchase orders, acknowledgments or check endorsements are issued on any forms containing terms and conditions which are inconsistent with these provisions, such inconsistent terms and conditions shall be of no force and effect. This document, including the CCC Billing and Payment Terms and Conditions, shall be the entire agreement between the parties relating to the subject matter hereof.

This Agreement shall be governed by and construed in accordance with the laws of the State of New York. Both parties hereby submit to the jurisdiction of the courts of New York County for purposes of resolving any disputes that may arise hereunder.

Gratis licenses (referencing $0 in the Total field) are free. Please retain this printable license for your reference. No payment is required.

If you would like to pay for this license now, please remit this license along with your payment made payable to "COPYRIGHT CLEARANCE CENTER" otherwise you will be invoiced within 48 hours of the license date. Payment should be in the form of a check or money order referencing your account number and this invoice number RLNK10748693.
Once you receive your invoice for this order, you may pay your invoice by credit card. Please follow instructions provided at that time.

Make Payment To:
Copyright Clearance Center
Dept 001
P.O. Box 843006
Boston, MA 02284-3006

If you find copyrighted material related to this license will not be used and wish to cancel, please contact us referencing this license number 2385651156752 and noting the reason for cancellation.

Questions? customercare@copyright.com or +1-877-622-5543 (toll free in the US) or +1-978-646-2777.

AMERICAN CHEMICAL SOCIETY LICENSE
TERMS AND CONDITIONS
Mar 10, 2010

This is a License Agreement between Abhilash Vincent ("You") and American Chemical Society ("American Chemical Society") provided by Copyright Clearance Center ("CCC"). The license consists of your order details, the terms and conditions provided by American Chemical Society, and the payment terms and conditions.

All payments must be made in full to CCC. For payment instructions, please see information listed at the bottom of this form.

License Number	2385090209884
License Date	Mar 09, 2010
Licensed content publisher	American Chemical Society
Licensed content publication	Langmuir
Licensed content title	Tuning Hydrated Nanoceria Surfaces: Experimental/Theoretical Investigations of Ion Exchange and Implications in Organic and Inorganic Interactions
Licensed content author	Abhilash Vincent et al.
Licensed content date	Feb 1, 2010
Volume number	0
Issue number	0
Type of Use	Thesis/Dissertation
Requestor type	Not specified
Format	Print
Portion	Full article
Author of this ACS article	Yes
Order reference number	
Expected completion date	Mar 2010
Estimated size(pages)	142

Billing Type	Invoice
Billing Address	12002 Pasteur Dr. APT-316 Orlando, FL 32826 United States
Customer reference info	
Total	0.00 USD

Terms and Conditions

Thesis/Dissertation

ACS / RIGHTSLINK TERMS & CONDITIONS
THESIS/DISSERTATION

INTRODUCTION
The publisher for this copyrighted material is the American Chemical Society. By clicking "accept" in connection with completing this licensing transaction, you agree that the following terms and conditions apply to this transaction (along with the Billing and Payment terms and conditions established by Copyright Clearance Center, Inc. ("CCC"), at the time that you opened your Rightslink account and that are available at any time at <http://myaccount.copyright.com>).

LIMITED LICENSE
Publisher hereby grants to you a non-exclusive license to use this material. Licenses are for one-time use only with a maximum distribution equal to the number that you identified in the licensing process; any form of republication must be completed within 60 days from the date hereof (although copies prepared before then may be distributed thereafter).

GEOGRAPHIC RIGHTS: SCOPE
Licenses may be exercised anywhere in the world.

RESERVATION OF RIGHTS
Publisher reserves all rights not specifically granted in the combination of (i) the license details provided by you and accepted in the course of this licensing transaction, (ii) these terms and conditions and (iii) CCC's Billing and Payment terms and conditions.

PORTION RIGHTS STATEMENT: DISCLAIMER
If you seek to reuse a portion from an ACS publication, it is your responsibility to examine each portion as published to determine whether a credit to, or copyright notice of, a third party owner was published adjacent to the item. You may only obtain permission via Rightslink to use material owned by ACS. Permission to use any material published in an

ACS publication, journal, or article which is reprinted with permission of a third party must be obtained from the third party owner. ACS disclaims any responsibility for any use you make of items owned by third parties without their permission.

REVOCATION
The American Chemical Society reserves the right to revoke a license for any reason, including but not limited to advertising and promotional uses of ACS content, third party usage, and incorrect figure source attribution.

LICENSE CONTINGENT ON PAYMENT
While you may exercise the rights licensed immediately upon issuance of the license at the end of the licensing process for the transaction, provided that you have disclosed complete and accurate details of your proposed use, no license is finally effective unless and until full payment is received from you (by CCC) as provided in CCC's Billing and Payment terms and conditions. If full payment is not received on a timely basis, then any license preliminarily granted shall be deemed automatically revoked and shall be void as if never granted. Further, in the event that you breach any of these terms and conditions or any of CCC's Billing and Payment terms and conditions, the license is automatically revoked and shall be void as if never granted. Use of materials as described in a revoked license, as well as any use of the materials beyond the scope of an unrevoked license, may constitute copyright infringement and publisher reserves the right to take any and all action to protect its copyright in the materials.

COPYRIGHT NOTICE: DISCLAIMER
You must include the following copyright and permission notice in connection with any reproduction of the licensed material: "Reprinted (“Adapted” or “in part”) with permission from REFERENCE CITATION. Copyright YEAR American Chemical Society."

WARRANTIES: NONE
Publisher makes no representations or warranties with respect to the licensed material.

INDEMNITY
You hereby indemnify and agree to hold harmless publisher and CCC, and their respective officers, directors, employees and agents, from and against any and all claims arising out of your use of the licensed material other than as specifically authorized pursuant to this license.

NO TRANSFER OF LICENSE
This license is personal to you or your publisher and may not be sublicensed, assigned, or transferred by you to any other person without publisher's written permission.

NO AMENDMENT EXCEPT IN WRITING
This license may not be amended except in a writing signed by both parties (or, in the case

of publisher, by CCC on publisher's behalf).

OBJECTION TO CONTRARY TERMS
Publisher hereby objects to any terms contained in any purchase order, acknowledgment, check endorsement or other writing prepared by you, which terms are inconsistent with these terms and conditions or CCC's Billing and Payment terms and conditions. These terms and conditions, together with CCC's Billing and Payment terms and conditions (which are incorporated herein), comprise the entire agreement between you and publisher (and CCC) concerning this licensing transaction. In the event of any conflict between your obligations established by these terms and conditions and those established by CCC's Billing and Payment terms and conditions, these terms and conditions shall control.

JURISDICTION
This license transaction shall be governed by and construed in accordance with the laws of the District of Columbia. You hereby agree to submit to the jurisdiction of the courts located in the District of Columbia for purposes of resolving any disputes that may arise in connection with this licensing transaction.

THESES/DISSERTATION TERMS
Publishing implications of electronic publication of theses and dissertation material
Students and their mentors should be aware that posting of theses and dissertation material on the Web prior to submission of material from that thesis or dissertation to an ACS journal may affect publication in that journal. Whether Web posting is considered prior publication may be evaluated on a case-by-case basis by the journal's editor. If an ACS journal editor considers Web posting to be "prior publication", the paper will not be accepted for publication in that journal. If you intend to submit your unpublished paper to ACS for publication, check with the appropriate editor prior to posting your manuscript electronically.

If your paper has already been published by ACS and you want to include the text or portions of the text in your thesis/dissertation in **print or microfilm formats**, please print the ACS copyright credit line on the first page of your article: "Reproduced (or 'Reproduced in part') with permission from [FULL REFERENCE CITATION.] Copyright [YEAR] American Chemical Society." Include appropriate information.

Submission to a Dissertation Distributor: If you plan to submit your thesis to UMI or to another dissertation distributor, you should not include the unpublished ACS paper in your thesis if the thesis will be disseminated electronically, until ACS has published your paper. After publication of the paper by ACS, you may release the entire thesis (**not the individual ACS article by itself**) for electronic dissemination through the distributor; ACS's copyright credit line should be printed on the first page of the ACS paper.

Use on an Intranet: The inclusion of your ACS unpublished or published manuscript is permitted in your thesis in print and microfilm formats. If ACS has published your paper

you may include the manuscript in your thesis on an intranet that is not publicly available. Your ACS article cannot be posted electronically on a publicly available medium (i.e. one that is not password protected), such as but not limited to, electronic archives, Internet, library server, etc. The only material from your paper that can be posted on a public electronic medium is the article abstract, figures, and tables, and you may link to the article's DOI or post the article's author-directed URL link provided by ACS. This paragraph does not pertain to the dissertation distributor paragraph above.

Other conditions:

v1.1

Gratis licenses (referencing $0 in the Total field) are free. Please retain this printable license for your reference. No payment is required.

If you would like to pay for this license now, please remit this license along with your payment made payable to "COPYRIGHT CLEARANCE CENTER" otherwise you will be invoiced within 48 hours of the license date. Payment should be in the form of a check or money order referencing your account number and this invoice number RLNK10747987.
Once you receive your invoice for this order, you may pay your invoice by credit card. Please follow instructions provided at that time.

Make Payment To:
Copyright Clearance Center
Dept 001
P.O. Box 843006
Boston, MA 02284-3006

If you find copyrighted material related to this license will not be used and wish to cancel, please contact us referencing this license number 2385090209884 and noting the reason for cancellation.

Questions? customercare@copyright.com or +1-877-622-5543 (toll free in the US) or +1-978-646-2777.

AMERICAN CHEMICAL SOCIETY LICENSE
TERMS AND CONDITIONS
Mar 10, 2010

This is a License Agreement between Abhilash Vincent ("You") and American Chemical Society ("American Chemical Society") provided by Copyright Clearance Center ("CCC"). The license consists of your order details, the terms and conditions provided by American Chemical Society, and the payment terms and conditions.

All payments must be made in full to CCC. For payment instructions, please see information listed at the bottom of this form.

License Number	2385080154321
License Date	Mar 09, 2010
Licensed content publisher	American Chemical Society
Licensed content publication	ACS Nano
Licensed content title	Protonated Nanoparticle Surface Governing Ligand Tethering and Cellular Targeting
Licensed content author	Abhilash Vincent et al.
Licensed content date	May 1, 2009
Volume number	3
Issue number	5
Type of Use	Thesis/Dissertation
Requestor type	Not specified
Format	Print
Portion	Full article
Author of this ACS article	Yes
Order reference number	
Title of the thesis / dissertation	PROBING THE NANOSCALE INTERACTION FORCES AND ELASTIC PROPERTIES OF ORGANIC AND INORGANIC MATERIALS USING FORCE DISTANCE (F-D) SPECTROSCOPY
Expected completion date	Mar 2010
Estimated size(pages)	142

Billing Type	Invoice
Billing Address	12002 Pasteur Dr. APT-316 Orlando, FL 32826 United States
Customer reference info	
Total	0.00 USD

Terms and Conditions

Thesis/Dissertation

ACS / RIGHTSLINK TERMS & CONDITIONS
THESIS/DISSERTATION

INTRODUCTION
The publisher for this copyrighted material is the American Chemical Society. By clicking "accept" in connection with completing this licensing transaction, you agree that the following terms and conditions apply to this transaction (along with the Billing and Payment terms and conditions established by Copyright Clearance Center, Inc. ("CCC"), at the time that you opened your Rightslink account and that are available at any time at <http://myaccount.copyright.com>).

LIMITED LICENSE
Publisher hereby grants to you a non-exclusive license to use this material. Licenses are for one-time use only with a maximum distribution equal to the number that you identified in the licensing process; any form of republication must be completed within 60 days from the date hereof (although copies prepared before then may be distributed thereafter).

GEOGRAPHIC RIGHTS: SCOPE
Licenses may be exercised anywhere in the world.

RESERVATION OF RIGHTS
Publisher reserves all rights not specifically granted in the combination of (i) the license details provided by you and accepted in the course of this licensing transaction, (ii) these terms and conditions and (iii) CCC's Billing and Payment terms and conditions.

PORTION RIGHTS STATEMENT: DISCLAIMER
If you seek to reuse a portion from an ACS publication, it is your responsibility to examine each portion as published to determine whether a credit to, or copyright notice of, a third party owner was published adjacent to the item. You may only obtain permission via Rightslink to use material owned by ACS. Permission to use any material published in an ACS publication, journal, or article which is reprinted with permission of a third party must

be obtained from the third party owner. ACS disclaims any responsibility for any use you make of items owned by third parties without their permission.

REVOCATION
The American Chemical Society reserves the right to revoke a license for any reason, including but not limited to advertising and promotional uses of ACS content, third party usage, and incorrect figure source attribution.

LICENSE CONTINGENT ON PAYMENT
While you may exercise the rights licensed immediately upon issuance of the license at the end of the licensing process for the transaction, provided that you have disclosed complete and accurate details of your proposed use, no license is finally effective unless and until full payment is received from you (by CCC) as provided in CCC's Billing and Payment terms and conditions. If full payment is not received on a timely basis, then any license preliminarily granted shall be deemed automatically revoked and shall be void as if never granted. Further, in the event that you breach any of these terms and conditions or any of CCC's Billing and Payment terms and conditions, the license is automatically revoked and shall be void as if never granted. Use of materials as described in a revoked license, as well as any use of the materials beyond the scope of an unrevoked license, may constitute copyright infringement and publisher reserves the right to take any and all action to protect its copyright in the materials.

COPYRIGHT NOTICE: DISCLAIMER
You must include the following copyright and permission notice in connection with any reproduction of the licensed material: "Reprinted (“Adapted” or “in part”) with permission from REFERENCE CITATION. Copyright YEAR American Chemical Society."

WARRANTIES: NONE
Publisher makes no representations or warranties with respect to the licensed material.

INDEMNITY
You hereby indemnify and agree to hold harmless publisher and CCC, and their respective officers, directors, employees and agents, from and against any and all claims arising out of your use of the licensed material other than as specifically authorized pursuant to this license.

NO TRANSFER OF LICENSE
This license is personal to you or your publisher and may not be sublicensed, assigned, or transferred by you to any other person without publisher's written permission.

NO AMENDMENT EXCEPT IN WRITING
This license may not be amended except in a writing signed by both parties (or, in the case of publisher, by CCC on publisher's behalf).

OBJECTION TO CONTRARY TERMS
Publisher hereby objects to any terms contained in any purchase order, acknowledgment, check endorsement or other writing prepared by you, which terms are inconsistent with these terms and conditions or CCC's Billing and Payment terms and conditions. These terms and conditions, together with CCC's Billing and Payment terms and conditions (which are incorporated herein), comprise the entire agreement between you and publisher (and CCC) concerning this licensing transaction. In the event of any conflict between your obligations established by these terms and conditions and those established by CCC's Billing and Payment terms and conditions, these terms and conditions shall control.

JURISDICTION
This license transaction shall be governed by and construed in accordance with the laws of the District of Columbia. You hereby agree to submit to the jurisdiction of the courts located in the District of Columbia for purposes of resolving any disputes that may arise in connection with this licensing transaction.

THESES/DISSERTATION TERMS
Publishing implications of electronic publication of theses and dissertation material
Students and their mentors should be aware that posting of theses and dissertation material on the Web prior to submission of material from that thesis or dissertation to an ACS journal may affect publication in that journal. Whether Web posting is considered prior publication may be evaluated on a case-by-case basis by the journal's editor. If an ACS journal editor considers Web posting to be "prior publication", the paper will not be accepted for publication in that journal. If you intend to submit your unpublished paper to ACS for publication, check with the appropriate editor prior to posting your manuscript electronically.

If your paper has already been published by ACS and you want to include the text or portions of the text in your thesis/dissertation in **print or microfilm formats**, please print the ACS copyright credit line on the first page of your article: "Reproduced (or 'Reproduced in part') with permission from [FULL REFERENCE CITATION.] Copyright [YEAR] American Chemical Society." Include appropriate information.

Submission to a Dissertation Distributor: If you plan to submit your thesis to UMI or to another dissertation distributor, you should not include the unpublished ACS paper in your thesis if the thesis will be disseminated electronically, until ACS has published your paper. After publication of the paper by ACS, you may release the entire thesis (**not the individual ACS article by itself**) for electronic dissemination through the distributor; ACS's copyright credit line should be printed on the first page of the ACS paper.

Use on an Intranet: The inclusion of your ACS unpublished or published manuscript is permitted in your thesis in print and microfilm formats. If ACS has published your paper you may include the manuscript in your thesis on an intranet that is not publicly available. Your ACS article cannot be posted electronically on a publicly available medium (i.e. one

that is not password protected), such as but not limited to, electronic archives, Internet, library server, etc. The only material from your paper that can be posted on a public electronic medium is the article abstract, figures, and tables, and you may link to the article's DOI or post the article's author-directed URL link provided by ACS. This paragraph does not pertain to the dissertation distributor paragraph above.

Other conditions:

v1.1

Gratis licenses (referencing $0 in the Total field) are free. Please retain this printable license for your reference. No payment is required.

If you would like to pay for this license now, please remit this license along with your payment made payable to "COPYRIGHT CLEARANCE CENTER" otherwise you will be invoiced within 48 hours of the license date. Payment should be in the form of a check or money order referencing your account number and this invoice number RLNK10747977.
Once you receive your invoice for this order, you may pay your invoice by credit card. Please follow instructions provided at that time.

Make Payment To:
Copyright Clearance Center
Dept 001
P.O. Box 843006
Boston, MA 02284-3006

If you find copyrighted material related to this license will not be used and wish to cancel, please contact us referencing this license number 2385080154321 and noting the reason for cancellation.

Questions? customercare@copyright.com or +1-877-622-5543 (toll free in the US) or +1-978-646-2777.
